2015

Acousto-Electric Impedance Of Ferroelectric Phononic Superlattice

Ola Hassan Nusierat
University of Mississippi

ACOUSTO-ELECTRIC IMPEDANCE OF FERROELECTRIC PHONONIC SUPERLATTICE

A Dissertation

presented in partial fulfillment of requirements

for the degree of Doctor of Philosophy

in the Department of Physics and Astronomy

The University of Mississippi

By

Ola Hassan Nusierat

April 2015

ABSTRACT

The acousto-electric impedance $Z(f)$ of a ferroelectric phononic superlattice (FPS) is investigated. The analytical derivation of $Z(f)$ and its phase $\theta(f)$ reveal that both are functions of physical parameters such as the electromechanical coupling coefficient, the mechanical quality factor, the domain length and the phase velocity of the plate acoustic waves (PAW). Mathematica code is produced that allows for modeling $Z(f)$ and $\theta(f)$ in a two dimensional FPS. It is observed that $Z(f)$ depends on the number of domains in the FPS structure. Fewer domains in the structure might minimize $Z(f)$ or make it approach zero at certain conditions.

A series of experiments is performed to investigate the impedance and its phase shift for a ZX-cut periodically poled lithium niobate in the frequency range 3-4 MHz. The experimental results of studying $Z(f)$ and (θ) are in a good agreement with the developed theory. Experiments reveal the stopband, when an acoustic wavelength is close to a double-length of ferroelectric domain within the inversely poled structure, in which $Z(f)$ has minima close to it. Furthermore, these experiments show that the displacement components of the acoustic mode are decoupled in the transition zone, a small frequency range that extends a few kilohertz from the boundary of the stopband, and the amplitude of those decoupled components goes to zero in that zone. The equations obtained, the computation codes developed, and the experimental investigations can be applied to the ultrasonic transducers and the field of energy harvesting

DEDICATIONS

All gratitude and thanks to God for protection and ability to work.

I am dedicating this dissertation to my loving, supportive, encouraging and patient husband Dr. ***ALI ALSHARADQAH*** whose faithful support during all stages of this Ph.D. is appreciated. And I dedicate it to the love of my life, ***Kareem*** and ***Jana***, who are collectively extending my horizon every day.

ACKNOWLEDGEMENTS

I would never been able to finish my dissertation without the guidance of my committee members, the help from my friends, and the support from my family and husband. My special thanks to my supervisor, Professor Igor Ostrovskii, who encouraged and directed me through my PH.D journey. His challenges brought this work towards a completion. It is with his guidance that this work came into existence. I would like to extend my appreciation to all of the members of my dissertation committee, Prof. Cremaldi the chair of the Physics department, Dr. Gladden the director of the National Center for Physical Acoustics, Dr. Beach from the Physics department, and Dr. Alkhateb from the Civil Engineering department, for agreeing to serve on my dissertation committee and their useful comments regarding this research work. For all their generous advice, assistance and companionship, I also thank Dr. Bombelli and Dr. Labuda from the Physics department.

I would like to thank my family in Jordan for all their love and encouragement, especially, my parents who raised me with a love of science and supported me in all my pursuits. Their major concerns are always my health and happiness.

God bless you all.

TABLE OF CONTENTS

LIST OF FIGURES

LIST OF TABLES

LIST OF SYMBOLS

c	Effective elastic constant
ρ	Density of crystal
t	Time
ω	Angular frequency
k	Wave number
h	Thickness of a plate
A	Acoustic displacement
T	Mechanical stress tensor
E	Electric field
D	Electric displacement
c_{ijkl}^{E}	Elastic modulus tensor components at constant electric field
$e_{ijkl}^{\pm}$	Piezoelectric tensor components changing its sign in neighboring domains
ε_{ij}^{S}	Components of dielectric permittivity tensor at constant strain
d	Single ferroelectric domain length along the x-axis
S_{kl}	Acoustic strain tensor and its components

$V(\omega)$ Applied voltage

$K^2 = e^2/\varepsilon c$ Squared electromechanical coupling coefficient

ε The effective dielectric constant of 3m-crystal along the x-axis.

J Current density

N Number of domains

FG Function generator

VVM Vector voltmeter

V Phase velocity

A_0 Zero Antisymmetric lamb wave mode

CHAPTER I INTRODUCTION

Historically, the motivation for research into acousto-electric phenomena was radar applications for military purposes. At that time, the most important requirement on the design of acoustic delay line devices was the highest performance with less focus on price and mass manufacturability. With the transition from military applications to the commercial and customer sector, the requirements imposed on the design of acousto-electric solid state devices shifted towards mass production at low cost while keeping an acceptable performance. Today's commercially available acousto-electric devices, such as transducers and oscillators, are based on two challenging technologies, namely The Surface and Bulk Acoustic Wave resonators, SAW and BAW, respectively. Both use piezoelectric materials and metal electrodes as transducers to convert electrical energy into mechanical and vice versa, while employing different types of acoustic waves in solids. The SAW resonators take advantage of surface acoustic waves propagating on the surface of the material while BAW resonators employ bulk acoustic waves propagating in the bulk of a crystal. The research in the field of acousto-electric phenomena is in continuous progress. New applications challenged new requirements on device performance leading to new solutions. Moreover, new devices can introduce higher versatility and lead to novel applications. As a result of recent research, a new type of acoustic resonator has emerged: the thin film plate acoustic resonator, employing another type of acoustic waves, Lamb waves, which are known as a class of guided waves in plates with free boundaries.

Lamb waves, sometimes called plate acoustic waves (PAW), are elastic waves that propagate in plates of finite thickness. A given plate can support a number of these waves depending on the value of the ratio h/λ, where h is the plate thickness and λ is the acoustic wavelength [1]. In recent years there has been a growing interest in using PAW for a variety of physical, chemical, and biological sensors [2, 3]. The operating principle of lamb wave sensors is similar to the more extensively studied surface acoustic wave (SAW) sensors [4]. However, important advantages of PAW over SAW sensors are obtained by utilizing the lowest-order antisymmetric Lamb wave mode, the A_0 mode, propagating in thin plates with thickness less than one-millimeter. These advantages include higher sensitivity, possible lower operating frequency, faster response, and ability to operate in liquid media.

Multidomain ferroelectrics have been the subject of fundamental physical investigations and possible applications since the early publications on fabrication of the periodic inversely poled structures over the past three decades [5-8]. The acoustic superlattice is proposed as a ferroelectric single crystal with 180^o domains arranged periodically with a periodicity in the range of ultrasonic waves [9-11]. Lithium niobate is a well-known ferroelectric crystal that possesses superior piezoelectric properties such as: a high electromechanical coupling coefficient, a low transmission loss, and a high chemical stability, suitable for microwave acoustic applications. The domain walls in Periodically Poled Lithium Niobate (PPLN) have been reported to be responsible for nonlinear ultrasonic attenuation [12]. Acoustic waves in thin piezoelectric plates have been attracting much attention recently [2, 13-25]. The existence of an acoustic stop band in superlattices has been shown for different composite structures [26, 27] and in $LiNbO_3$ crystals [28]. A specific acoustic plate mode could not propagate within the frequencies of the acoustic stopband, due to the total destructive interference by the interdomain walls [29].

When the acoustic wave length is close to the length of two inversely poled domains (2d), so-called “domain resonance” may take place, and consequently the highest vibration amplitude is observed in a specific frequency range. It is demonstrated that at least two resonances in acousto-electric transduction instead of one do exist in the optimal frequency range [30]. No information about the boundary regions of the stopband seems to have been reported in literature.

The field of acoustic metamaterials, in which materials are artificially engineered exhibits unusual and useful acoustic material properties. Most current designs of acoustic metamaterials are based on the stopband effect [31].

The investigation of the acousto-electric impedance $Z(f)$ of a ferroelectric phononic superlattice is a direction of research in the fields of solids and physical acoustics. The acousto-electric transducers are intended for transformation of electrical energy into acoustic signal and back. The impedance of a single crystal of lithium niobate (LN) and quartz is investigated. Up to our knowledge, the acousto-electric impedance, which is a fundamental physical property of FPS under consideration, has not been considered yet in literature. The frequency characteristics of $Z(f)$ and its phase shift are essential for developing new applications, for instance, new ultrasonic transducers and sensors. The impedance is also an important step in understanding the physics of FPS, including practical usage in the applications. Therefore, the main objectives are as follows.

1) Developing problem formulation to find the impedance of FPS by analytical solution of the corresponding equations.
2) Deriving analytical relations describing the impedance as a function of physical parameters of FPS.

3) Computer modeling the impedance depending on the physical parameters of FPS based on $LiNbO_3$.
4) Verifying experimentally the analytical equations and the computer modeling, describing the impedance of FPS, by using PPLN, which is a typical FPS.
5) Analytical derivations to obtain the equations for the phase shift of the impedance.
6) Developing computational model to consider the impedance phase shift as a function of FPS parameters.
7) Performing experiments for estimating the impedance phase shift of FPS in $LiNbO_3$.

Physical acoustics considers wave propagation in a media. And its propagation is a phenomenon involving stress and strain. Two different modes of elastic waves, including longitudinal and shear in an isotropic medium, will be considered in this chapter. Isotropic material is considered so that its properties are independent of the material orientation. The simplest form of acoustic waves is the plane wave, in which all wave characteristics are constants over a plane called wave front. In the longitudinal wave, the displacement is parallel to a propagation direction. In the transverse wave, displacement is in any direction parallel to the wave front, and normal to the propagation direction.

This chapter also presents the basic properties of ferroelectrics with a special emphasis on lithium niobate (LN), which is the main material for research discussed later in this dissertation. This is followed by an introduction of ferroelectric domains. Acoustic superlattice and the acoustics stopband, in phononic crystal, will be introduced and explained. Plate acoustic waves propagating in lithium niobate wafer will be described. This chapter builds a solid basic knowledge needed in this research.

1.1 Strain

Force applied to a solid body will deform it. This deformation can be represented by the displacement vector $\vec{A}$ and the strain S defined with respect to a reference point. In general, the displacement vector has components that vary continuously from one point to another in the solid. A plane wave generates displacements that vary harmonically in the direction of the wave propagation. If that is in the X-direction, the wave amplitude A may be represented by $\vec{A}(x,y,z) = (A_1\hat{x} + A_2\hat{y} + A_3\hat{z})e^{i(\omega t - kx)}$,

in which A_1, A_2, A_3 represent particle displacements along the X, Y and Z directions, respectively; ω is the angular frequency, and k is the wave number. Because simple translation of the entire solid is not of our interest, this class of motion is eliminated to give a parameter related only to local deformations of the solid. The gradient of the displacement vector $\vec{\nabla}A$ represents the changes in a particular distance as well as local rotations. Once the effect of simple translation is eliminated, by taking the gradient of the displacement vector, the contribution due to rotations can be eliminated as well, resulting in a parameter that describes only the local stretching of the solid[32, 33]. This is accomplished by adding the displacement gradient to its transpose. The resulting strain matrix S describes this deformation with respect to a reference point. Tensor notations will be used here to report the elastic parameters in acoustics. The strain tensor is given by

$$S_{ik} = \frac{1}{2}\left(\frac{\partial A_i}{\partial x_k} + \frac{\partial A_k}{\partial x_i}\right) \quad . \tag{1.1}$$

The diagonal strain terms S_{ii} represent the axial strain components, while the off-diagonal terms (S_{ik}), where $i \neq j$ are the shear strains.

1.2 Stress

In this work, a static equilibrium condition is assumed in a body under external forces, so there is no net translation or rotation. Two types of forces might act on an object, which are the body forces, such as gravity, that acts throughout the body and the surface forces that are proportional to the area of the surface. The force F acting in the X-direction on a body of volume V is given by $\int F_X dV$, where F_x is a scalar quantity that can be written in terms of the divergence of a vector $F_X = \nabla \cdot T$, where T is the stress vector of three components. Using Gauss's theorem, one can write

$$\int_V F_X dV = \int_V \nabla \cdot T dV = \int_s T \cdot ds \ , \tag{1.2}$$

where the surface integral is taken over the enclosed volume, so the average force on an element dV is

$$\frac{1}{dV}\int \nabla \cdot T dV = \frac{1}{dV}\int \frac{\partial T_{ij}}{\partial x_j} dV = \frac{1}{dV}\int T_{ij} d S_j \ . \tag{1.3}$$

Consider a cube of length b as shown in Figure 1-1-(a). Being interested in surface forces acting on it, leads to a deformation reported by a strain tensor. If a force acts on XY-plane, then two vectors are involved. These vectors are normal and tangential to the surface. Total stress will be broken into two types of stresses: a normal component of the applied force would

give rise to a tensile stress, and the tangential component would give rise to shear stresses, as appears in Figure 1-1-(b).

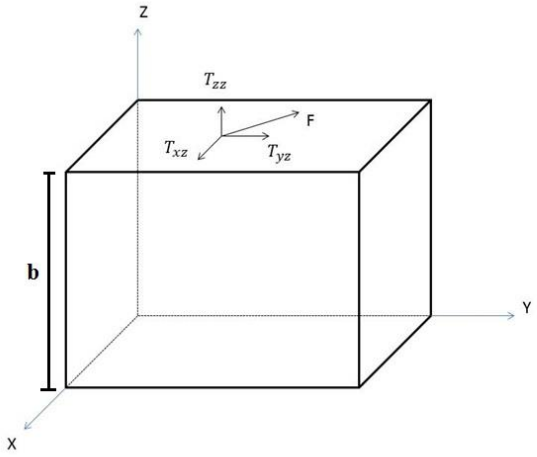

Figure 1-1-(a). Force F acting on the XY-plane of a cube.

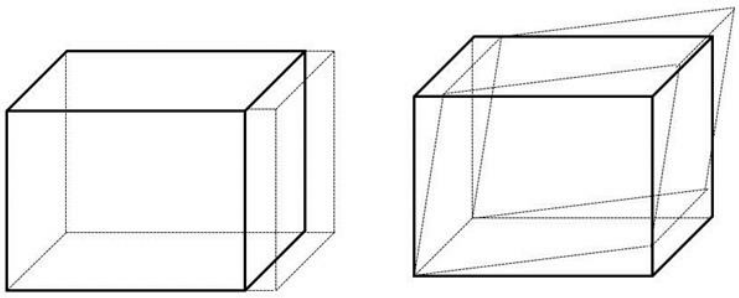

Figure 1-1-(b). Tensile and Shear stain.

A static equilibrium must be taken into consideration to give the symmetry to the stress tensor. In the case of tensile stress, the tensor is diagonal with three independent components. However, the shear stress would have three off-diagonal components to avoid rotation.

1.3 Hooke's law

Under Hooke's law, a stress is proportional to strain for a small elongation of an elastic system. Waves are distinguished by different types of deformation. A shear wave is consistent with a change of the cube shape at constant volume, so $S_{ii} = 0$. Pure hydrostatic compression produces a change of volume at constant shape. Tensor notations are introduced to explain the elastic parameters in physical acoustics. Tensors are a generalization of vectors. They represent real physical quantities, and their importance comes from relating two vectors. In linear elasticity

$$T_{ij} = c_{ijkl} S_{kl} \quad , \tag{1.4}$$

where c_{ijkl} is a symmetric 4th rank elastic constant tensor connecting two second-rank tensors. The symmetry of the elastic constant, considering the lack of rotation given by $c_{ijkl} = c_{jikl} = c_{ijlk} = c_{jilk}$ and the reciprocity $c_{ijkl} = c_{klij}$, would reduce the number of the independent elastic components from 81 to 36, represented by a 6×6 matrix. Additional simplification of the stress-strain relationship can be realized through simplifying the matrix notation for stresses and strains. The indices can be replaced as follow; $c_{ijkl} = c_{mn}$, where $ijkl = 1,2,3$ and $mn = 1,2....,6$, which is explained in the following table [43].

Tensor notations	Matrix notations	Corresponding strain
11	1	Longitudinal in X-direction
22	2	Longitudinal in Y-axis
33	3	Longitudinal in Z-direction
12=21	4	Shear Y-Z
13=31	5	Shear Z-X
23=32	6	Shear X-Y

Table 1. Conversion table from regular indices to reduced indices.

Of the 36 constants, there are six constants where $m = n$, and 30 constants where $m \neq n$. Only one half of these constants are independent since $c_{mn} = c_{nm}$. Therefore, for the general anisotropic linear elastic solid, there are $\frac{30}{2} + 6 = 21$ independent elastic constants. The 21 independent elastic constants can be reduced still further by considering the symmetry conditions found in different crystal structures.

Lame` constants: The number of independent elastic constants in an isotropic medium will be reduced to two because of symmetry. These two constants are called Lame constants (μ and λ). These parameters can be used to determine the total stored energy in a system. In an isotropic medium, the three coordinate axes and the three coordinate planes are equivalent. Let us consider a cubic crystal in which the elastic constants are as follow

$$c_{11} = c_{22} = c_{33} = \lambda + 2\mu, \tag{1.5}$$

$$c_{44} = c_{55} = c_{66} = \mu = \frac{c_{11} - c_{12}}{2} \quad , \tag{1.6}$$

$$c_{12} = c_{13} = c_{23} = c_{21} = c_{31} = c_{32} = \lambda, \tag{1.7}$$

where λ and μ are Lame constants. For example, c_{12} corresponds to the ratio of the longitudinal stress in the X-direction to the longitudinal strain in the Y-direction. This term occurs when a material is compressed in one direction, so it will expand in the perpendicular direction. When dealing with isotropic materials, additional conditions are applied. If shear wave propagates along Z-axis, with motion in the X-axis, then the strain is $S_5 = \frac{\partial A_x}{\partial z}$. From Equation (1.8), the stress can be written in this form $T_5 = \mu S_5$. Therefore, the cubic crystal stress can be expressed as $T_5 = c_{44} S_5$, where the parameter μ is known as shear modulus. All other terms are zero because of mirror symmetry. The elasticity matrix of an isotropic material is given by Equation (1.8)

$$\begin{bmatrix} T_1 \\ T_2 \\ T_3 \\ T_4 \\ T_5 \\ T_6 \end{bmatrix} = \begin{bmatrix} \lambda+2\mu & \lambda & \lambda & 0 & 0 & 0 \\ \lambda & \lambda+2\mu & \lambda & 0 & 0 & 0 \\ \lambda & \lambda & \lambda+2\mu & 0 & 0 & 0 \\ 0 & 0 & 0 & \mu & 0 & 0 \\ 0 & 0 & 0 & 0 & \mu & 0 \\ 0 & 0 & 0 & 0 & 0 & \mu \end{bmatrix} \begin{bmatrix} S_1 \\ S_2 \\ S_3 \\ S_4 \\ S_5 \\ S_6 \end{bmatrix} . \quad (1.8)$$

The longitudinal stress $T_1 = \lambda(S_1 + S_2 + S_3) + 2\mu S_1 = \lambda\Delta + 2\mu S_1$ can be written in a general form

$$T_I = \lambda\Delta + 2\mu S_I, \quad I = (1,2,3), \quad (1.9)$$

$$\Delta = S_{ii} = (S_1 + S_2 + S_3) = \nabla \cdot A \quad , \quad (1.10)$$

where Δ is the dilation. Similarly, shear stress can be expressed as:

$$T_4 = \mu S_4, \quad (1.11)$$

$$T_5 = \mu S_5, \tag{1.12}$$

And $T_6 = \mu S_6$. (1.13)

It follows that in the isotropic cube, there are only two independent elastic constants: c_{12} and c_{44}.

1.4 Equation of motion for solids

Consider an element of length l that is affected by an external force F acting in the positive X-axis. This results in elongation ∂A. Then the total stress on the element is $T = l\left(\frac{\partial T}{\partial x}\right)$, which gives a total force per unit volume of $\left(\frac{\partial T}{\partial x}\right)$. Combining Hooke's law with Newton's law will lead us to the wave equation

$$\rho \frac{\partial^2 A}{\partial t^2} = \vec{\nabla} \cdot \vec{T}. \tag{1.14}$$

The propagation of a wave in the X-direction with velocity v and a displacement vector *A* is given by

$$\vec{A} = A_\circ e^{i(\omega t - kx)} + B_\circ e^{i(\omega t + kx)}. \tag{1.15}$$

The first term shows the propagation in the forward direction and the second term shows the propagation in the backward direction with wave number $k = \frac{\omega}{v}$. These results can be

generalized to three dimensions, so three acoustic polarizations do exist: a longitudinal wave and two transverse waves with orthogonal polarization [34, 35]. Hooke's law and Newton's law will be used to get the wave equation in three dimensions. Tensor notations will be used, and the displacement vector can be written using the gradient of a scalar (ϕ) and the curl of a vector $(\vec{\psi})$ potential. Thus,

$$\vec{A} = \vec{\nabla}\phi + \vec{\nabla} \times \vec{\psi} \quad . \tag{1.16}$$

Using these identities from vector analysis $\begin{Bmatrix} \nabla \cdot (\nabla \times \psi) = 0 \\ \nabla \times (\nabla \phi) = 0 \end{Bmatrix}$ will allow us to separate the equations of propagation into longitudinal and transverse waves $\vec{A} = \vec{A}_l + \vec{A}_S$, such that the scalar term $\vec{A}_l = \nabla\phi$ associated with the longitudinal wave is

$$\rho \frac{\partial^2 \phi}{\partial t^2} - (\lambda + 2\mu)\vec{\nabla}^2 \phi = 0 \, . \tag{1.17}$$

The curl of $(\vec{A}_l)$ equals zero, so there is no rotation or change of angle associated with it. $\vec{A}_L(\phi)$ is a characteristic of the longitudinal wave. For a wave propagating as in Equation (1.15), the longitudinal wave number and its velocity will be given by Equations (1.18) and (1.19), respectively.

$$k_l^2 = \frac{\omega^2 \rho}{\lambda + 2\mu} = \frac{\omega^2}{v_l} \tag{1.18}$$

$$v_l = \sqrt{\frac{\lambda + 2\mu}{\rho}} \ , \tag{1.19}$$

The vector term associated with the transverse wave is

$$\rho \frac{\partial^2 \vec{\psi}}{\partial t^2} - \mu \vec{\nabla}^2 \vec{\psi} = 0 \ . \tag{1.20}$$

One property of the displacement $\left(\vec{A}_S\right)$ is that its divergence equals zero, so there is no change in the volume associated with it. On the other hand, there must be a change in volume associated with the transverse wave. Hence, for a wave propagating as in Equation (1.15), the shear wave number and its velocity will be given by Equations (1.21) and (1.22), respectively.

$$k_s^2 = \frac{\omega^2 \rho}{\mu} = \frac{\omega^2}{v_s}, \tag{1.21}$$

$$v_s = \sqrt{\frac{\mu}{\rho}} \ . \tag{1.22}$$

The deformations of these two waves are shown in Figure 1-2 below.

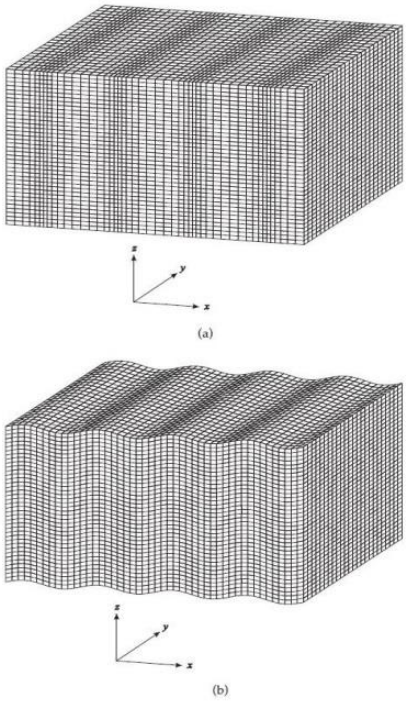

Figure 1-2. Deformation by bulk plane waves propagating along x-axis. (a) Longitudinal waves. (b) Transverse waves polarized in the z-axis [35].

1.5 Lamb waves

Depending on the direction of particle displacement, there are two different types of guided waves possible in plates, namely shear horizontal acoustic plate modes and Lamb waves, or plate acoustic waves (PAW). The former corresponds to the horizontal polarization in the plane of the plate (shear or quasi-shear) while the latter has elliptical polarization in the sagittal plane. Generally, depending on the thickness-to-wavelength ratio, the plate can support a number of these waves. Further, each type of plate mode can be classified as symmetric or antisymmetric, indicating the symmetry of particle displacement relative to the median plane of the plate.

1.6 Ferroelectric and crystallographic classes

A ferroelectric material is both pyroelectric and piezoelectric. It is characterized by a spontaneous, reversible polarization in the absence of an electric field [36]. When mechanical stress is applied in the direction of the spontaneous polarization, an induced polarization and a surface charge is produced through the direct piezoelectric effect [36]. Below the critical temperature, the Curie temperature (Tc), ferroelectric materials possess ferroelectric behavior. While above the Curie temperature, ferroelectric materials get into the paraelectric phase in which they no longer exhibit a spontaneous polarization.

Crystal classes: There are 32 crystal classes, and 21 of them lack a center of symmetry. A crystal which shows a centrosymmetric structure does not possess polar properties, and thus cannot be piezoelectric. Of the 21 noncentrosymmetric classes, 20 are piezoelectric. Ten of the piezoelectric classes are also pyroelectric, which means that they have a spontaneous polarization that does exist in the absence of an applied electric field or stress. This polarization is an outcome of a displacement between the centers of positive and negative charge in the crystal unit cell, and their values change with temperature. Ferroelectric materials are a subgroup of pyroelectric materials with an exchangeable spontaneous polarization. The pyroelectric materials that are not ferroelectrics occur because their spontaneous polarizations are not exchangeable by an applied electric field [37].

1.7 Ferroelectric domains and surfaces

Regions in ferroelectric materials that consist of a large number of dipoles aligned in the same direction with the same amplitude are called domains. Partitions between domains with different dipole polarization direction are called domain walls (or boundaries) [36]. Domain walls are usually divided into two classifications: 180° and non-180° walls. Materials such as lithium niobate supports only two possible polarization orientations along their *c*-axis. The polarization orientations in the neighboring domains are antiparallel to each other. Thus the domain walls are 180°-domain walls. Materials having tetragonal structures, such as PZT and BaTiO3, can have both 90° domains and 180° domains. Materials having rhombohedral structures, such as BiFeO3, can have 71° and 109° domains. The normal component is approximately continuous across the wall. Technology has developed a characterization of ferroelectric domains, including polarization microscopy[38]; second harmonic generation microscopy [39], and scanning electron microscopy[40].

Ferroelectric surfaces: Different orientations of polarization induce positive or negative charges at the ferroelectric material surface. The value of surface charge is given by the normal component of polarization:

$$\sigma = \vec{P} \cdot \hat{n} \tag{1.23}$$

where $\vec{P}$ is the polarization vector and $\hat{n}$ is the unit vector normal to the surface. The surface with unscreened bound charges is energetically unfavorable and thus has to be screened [41] to minimize surface potential. To achieve this, the surface charges undergo external and/or internal screening. External screening is described by the absorption of charged molecules, or surface states due to the surface layer, while internal screening is from free carriers and defects in the

bulk and is distinguished by the formation of a space-charge layer near the surface. Ferroelectric materials such as PZT and BaTiO3 have larger defect density compared to materials such as LiNbO3 and LiTaO3. Hence, for PZT and BaTiO3, the dominant screening is internal screening, while for LiNbO3 and LiTaO3, the dominant screening is external screening. For thin ferroelectric films, the external screening molecules and ionic charges could even control the polarization orientations in the film. In an applied electric field, polarization switching is considered to occur through the nucleation and growth of new domains. In the chemical switching process, the nucleation is suppressed, and switching occurs by uniform decrease and incursion of the polarization without domain creation.

1.8 Ferroelectric superlattice

Novel material systems can be engineered by alternating thin layers of two or more materials in one stacked system. To prepare multilayer samples consisting of alternating layers of thickness d_1 of constituent 1 and thickness d_2 of constituent 2, samples can be prepared so that d_1 and d_2 have any values from two or three atomic spacing up to the order of 100nm or more. We introduce them as periodically layered structures or superlattices. Many of the physical properties are greatly adjusted by the existence of the long (compared with the lattice parameter) spatial period $L = d_1 + d_2$. The most important general consequence is that as a result of Bloch's theorem, a new Brillouin Zone edge appears at wave vector component π/L perpendicular to the interfaces. This can be much smaller than the Zone-edge wave vector π/a related to the lattice constant a. Dispersion curves, such as those for acoustic phonons for example, develop band gaps at these new zone edges. Interesting advantages arise in a

superlattice system for many reasons, including size and strain effects in the individual layers, competition between the properties of the constituent materials, and interactions at the interfaces. Superlattice properties are usually discussed as being dependent on the volume fraction of one of the constituent materials [42]. The sample under consideration in this dissertation is a periodically poled LN. The sample was fabricated in the laboratory [30]. Figure 1.3 shows the inverse domains of PPLN sample [43]. The darker strips are domains with inverted polarization, and the light gray strips are domains with original polarization.

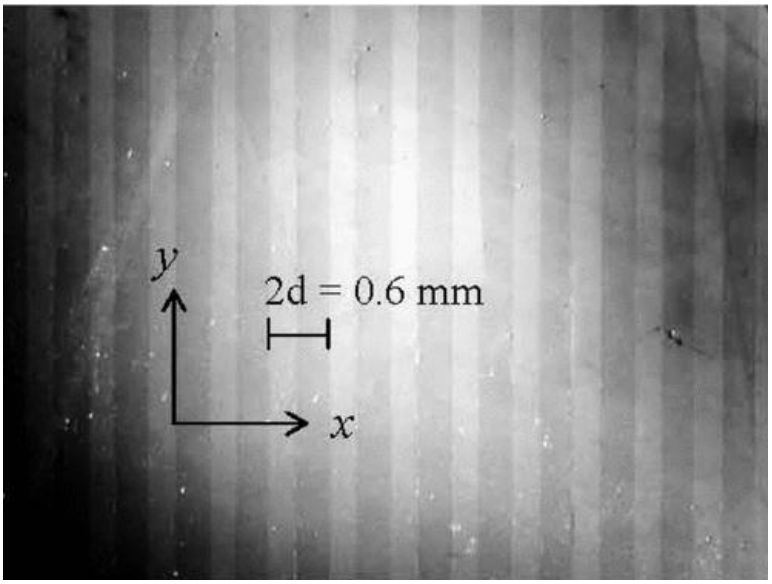

Figure 1-3. Micropicture of PPLN sample LN-MD-1 taken through a polarizing microscope. The width of two adjacent domains is 0.6mm along the crystallographic x-axis.

1.9 Bandgap in phononic crystals

The first phononic band gap was determined by Sigalas and Economou (1993) [44], followed by Kushwaha in 1995 [45]. The existence of full band gaps has led to a range of applications such as filters [46], acoustic waveguides [47, 48], and strong resonators [49]. The concept of band gaps can be explained by considering the interference of multiple waves scattered within a phononic crystal. When a set of scattering elements is positioned periodically, waves are dispersed from one element to the other and end up filling all available space and propagating in every direction. The waves interfere constructively or destructively depending upon the frequency and on the phononic crystal geometry. A band gap appears when the scattered waves interfere destructively in a given direction. For surface acoustic waves, a complete band gap is found experimentally in a two dimensional square-lattice piezoelectric phononic crystal etched in lithium niobate [29]. Similar experiments have been carried out in a silicon plate and showed the complete bandgap for Lamb waves [50]. Different lattices have been investigated. The most common is the square-lattice, although a full bandgap is difficult to achieve, especially in solid material. The triangular and hexagonal lattices allow the creation of larger bandgaps [51, 52]. However, in order to induce a wide frequency band gap, the hexagonal lattice requires the film thickness to be approximately the same of the lattice constant. By using two solid materials with strong contrast in the elastic modulus, it is possible to obtain larger bandgaps [53]. The ability to create band gaps also creates the possibility to confine the energy and create waveguides. Waveguides are important in the communication field to avoid the loss of energy due to the diffraction of the waves.

The stopband properties are made known from the dispersion of phase and group velocities of PAW modes propagating in a two-dimensional periodically poled ferroelectric

wave-guide. Figure 1-4 shows the dispersion of phase velocities for the six lowest PAW modes in a LN wafer near the boundary of the first Brillouin zone in PPLN [43]. From the dispersion curves shown in Figure 1-4, it is seen that Lamb waves are quite dispersive, but for a certain thickness-to-wavelength ratio the lowest symmetrical mode S_0 is low dispersive. Furthermore, the A_0 mode seems to be suitable for low frequency applications. For semi-infinite plates, the lowest A_0 and S_0 Lamb modes converge to a Rayleigh wave propagating along the free surface.

A frequency range of 3-4 MHz is considered in this dissertation, in which the A_0 mode does exists within the wave number range corresponding to a plate thickness of 0.5mm.The A_0 mode is indicated by number one in Figure 1-4, in which the existence of the stopband is clear and is indicated by SB1. The physical origin of stopbands is a Bragg-type reflection of acoustic modes from the multidomain superlattice at the boundary of acoustic first Brillouin zone. Stopbands occur when a particular PAW mode has a wave vector $k = \pi/d$, where d is the domain length. In other words, the stopband takes place because a PAW mode is "trapped" within the multidomain phononic superlattice. Those waves are then reflected by this superlattice when an acoustic wavelength is approximately equal to doubled superlattice period $\lambda = 2d$.

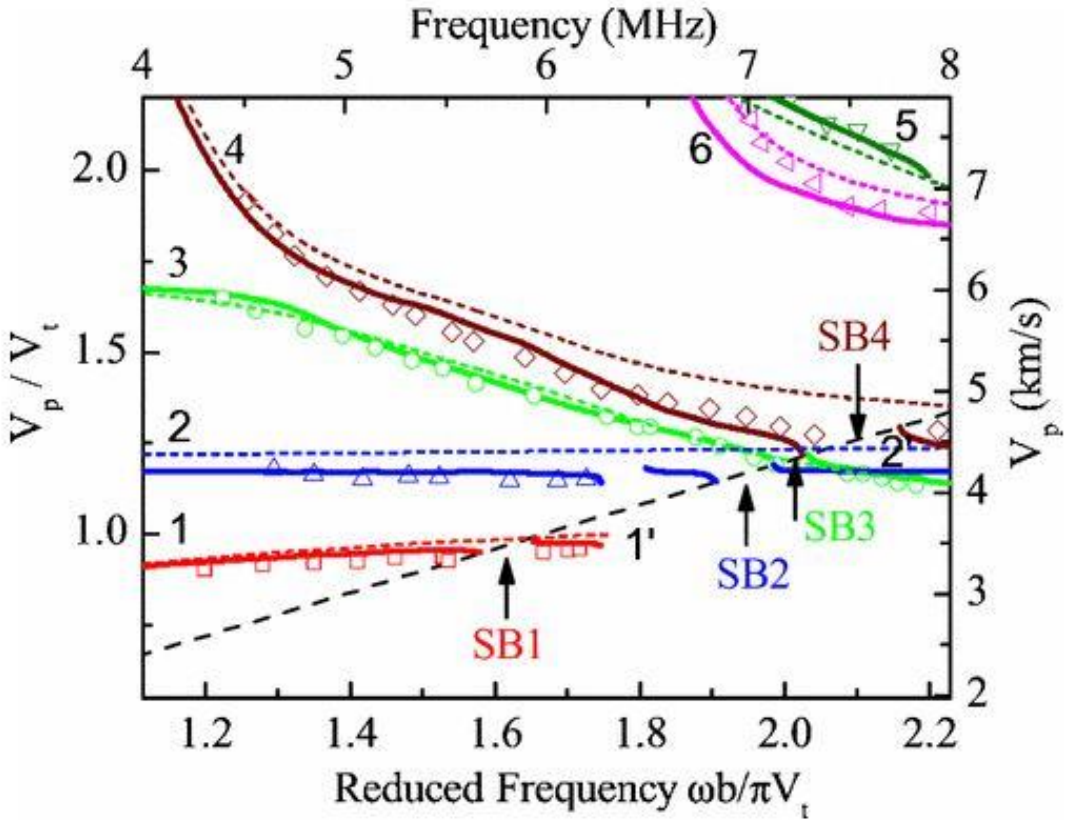

Figure 1-4. Dispersion of phase velocity for six lowest PAW modes in LiNbO3 wafer near boundary of the first acoustic Brillouin zone (ABZ) in PPLN. The inclined dashed line corresponds to $k = \pi/d$. The solid and dotted lines are FEM computations for PPLN and single crystal LN 0.5-mm-thick wafer, respectively. The points are experimental data taken from the multidomain sample LN-MD-1 with domain period d=0.3mm. Different colors indicate different PAW modes. The modes are: 1-A_0, 2-SS_0, 3-S_0, 4-SA_1, 5-A_1, and 6-S_1 [43].

The plate acoustic wave can propagate at frequencies below F_L (lower frequency) and at frequencies above F_U (upper frequency); between F_L and F_U there is no transmission of acoustic displacements through the FPS. The destructive interference is due to diffraction by the inter-domain walls, which causes a single acoustic wave to split into two modes; $m1$ and $m2$ at $k = k_D = \pi/d$, is shown in Figure 1-5 taken from reference [54] under others permission [54]. Finite element modeling (FEM) is represented in Figure 1-6 for the ZX-cut PPLN sample of thickness 0.5mm and domain length of 0.45mm [54]. The acoustic wave cannot propagate within the stopband between 3.27 and 3.67MHz, where the dispersion curve is interrupted. The output of the dispersion curve cannot be obtained, because of the destructive diffraction from the domain walls. The stopband range corresponds exactly to an acoustic wavelength of $\lambda = 2d = 0.9mm$ or $(1/\lambda) = 1.11mm^{-1}$. The horizontal line $(1/\lambda) = 1.11mm^{-1}$ is the boundary between the first and second acoustic Brillouin zone (ABZ).

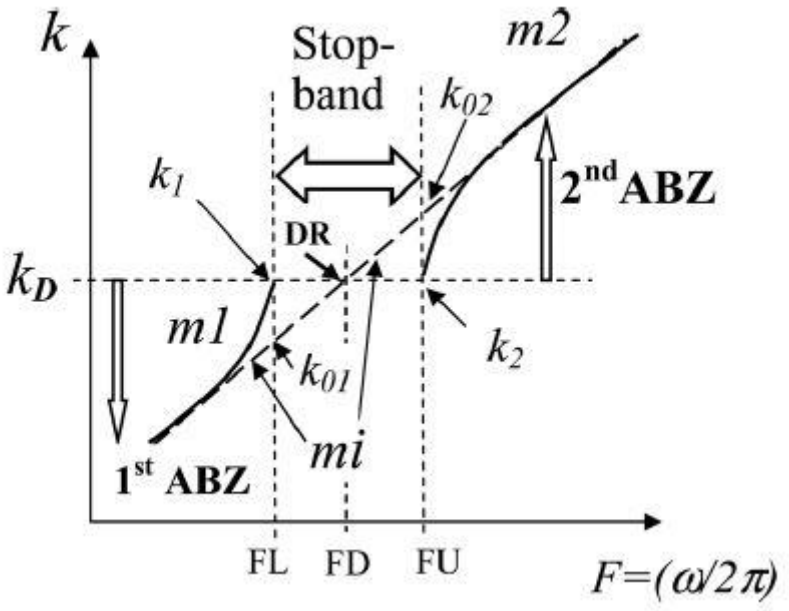

Figure 1-5. Dispersion curve using finite element modeling of the zero antisymmetric mode in ferroelectric phononic superlattice. FPS is fabricated in ZX-cut 0.5-mm-thick LN with domain length d=0.45mm and 44 domain pairs [54]. The initial single mode mi shown by a dashed line split into two modes, m1 and m2, as shown by the solid lines, in the first and second ABZ, respectively. The first ABZ is at F < FL, and the second ABZ is at F > FU; within the stopband, FL < F < FU, acoustic modes cannot propagate.

Finite element calculations presented in Figures 1-6(a) and 1-6(b) show the dispersion curves for longitudinal and transversal acoustic displacements, A_X and A_Z, respectively. The longitudinal displacement branch has a limiting frequencies F_{1X} =3.28±0.01MHz and F_{2X}= 3.67±0.01MHz. The transverse displacement branch has a limiting frequencies F_{1Z} =3.26±0.01MHz and F_{2Z}= 3.66±0.01MHz.

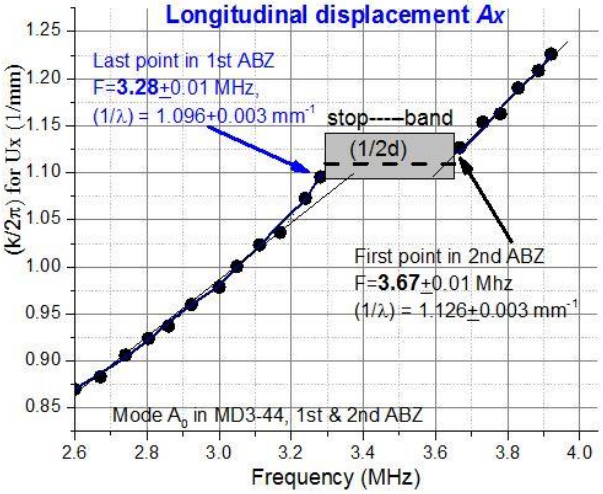

Figure 1-6 (a)

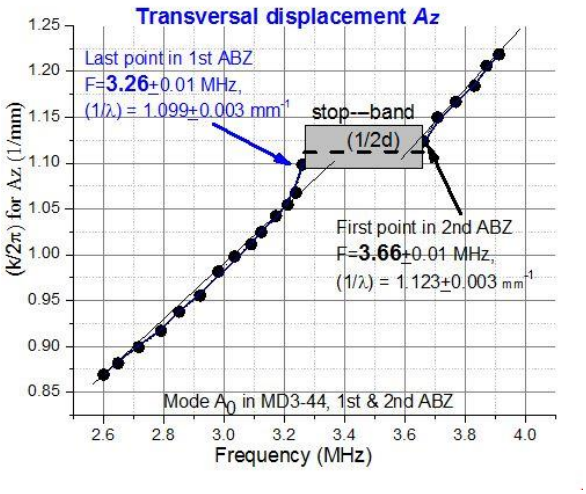

Figure 1-6 (b)

Figure 1-6. FEM-computations of the dispersion curve for (a) the longitudinal displacement A_X, and for (b) the transverse displacement A_Z, in MD3B-NC superlattice [54] .

CHAPTER II MATERIALS, SAMPLES AND EXPERIMENTAL METHODS.

This chapter is dedicated to the experimental techniques along with the samples provided by the laboratory to investigate the measurements of the acousto-electric impedance later in this dissertation. Main samples materials, quartz and lithium niobate, are explained in details. Two experimental methods are discussed to perform these investigations.

2.1 Materials

This section introduces the materials used for this research. Mainly a single quartz crystal and lithium niobate are included. General properties of the materials such as the crystallographic structure and electrical properties are presented in details to provide the reader with basic information needed later in this dissertation.

2.1.1 Single crystal Quartz

A piece of a crystal, like every other elastic body, has a series of resonant vibrational frequencies. The vibrating crystals are widely used in electronic devices as a frequency provider due to their unique properties. The most common example is the quartz crystal watches or clocks for time keeping, in which the flow of time is measured by counting crystal vibration cycles. Vibrating crystals also provide frequency basics for telecommunication devices in which frequency selections and operations are needed. Most of the commercial crystal resonators are made of quartz. Quartz is a crystal of silicon dioxide.

In crystallography, quartz belongs to class 32 of trigonal crystal structure [55]. There is a large amount of natural quartz, but it also can be artificially synthesized to very high quality. In addition to piezoelectricity, quartz has a very low damping factor. It has low solubility and is comparably hard but not brittle. It also can be cut into different shapes [56]. All of the above make quartz crystal one of the best materials for resonators.

Indeed, resonant frequencies and wave velocities are essential properties of an elastic body. Most crystals are highly anisotropic, and as a consequence, they often exhibit a piezoelectric effect. For a piezoelectric resonator, the operating mode or wave can be directly excited electrically, such that the resonator can be integrated into a circuit. A specific cut of a crystal plate refers to the crystallographic orientation of the plate when it is fabricated out of a bulk crystal. Quartz plates of different cuts have different mechanical properties along the coordinates normal and parallel to the plate surfaces. Examples of rotated Y-cuts include BT-cut (θ=-45˚), Y-cut (θ=0˚), and AT-cut [57, 58]. Crystal resonators are common acoustic wave devices. In fact, vibration modes or waves in a crystal can be divided into two types. The first type is bulk acoustic waves (BAW), which can propagate all over the crystal. The second type is surface

acoustic waves (SAW), which can only propagate along the crystal boundary. The particle displacements vanish quickly inside the crystal. Both bulk and surface waves are widely used in acousto-electric solid-state devices. For example, quartz is the most typical material for BAW devices.

A driving voltage is applied to the crystal for exciting the vibration in piezoelectric plates. As with all solid structures, a quartz crystal resonator can show different kinds of bulk acoustic wave modes at the resonance frequencies. Note that the crystal can also vibrate at overtones of every fundamental mode and that the existing modes can sum up to create complicated resonances modes. Hence, it is preferable to have the possibility to select only one specific mode and suppress the unneeded ones so that the resonator is oscillating at only one fundamental mode. This selection demands the crystal slab to have proper shape and be cut-out at a particular crystallographic orientation. The Y-cut quartz crystal, which is used in this dissertation, has a fundamental frequency at 10 MHz. Such a quartz plate oscillates under the thickness shear modes. Figure 2-1 shows the fundamental thickness shear mode of a plate. The arrows show the direction of particle displacement. The fundamental mode has only one node along the thickness and is antisymmetric with respect to $x_2=0$. The second thickness shear mode has two nodes and is symmetric with respect to $x_2=0$ plane, and so on.

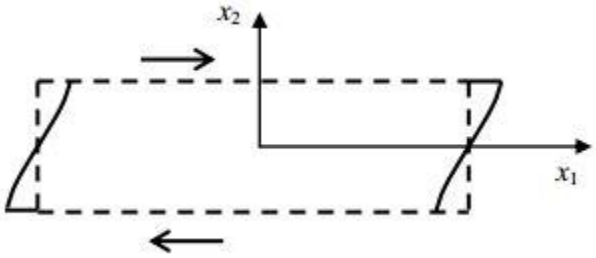

Figure 2-1 Fundamental thickness shear mode of a vibrating plate.

When a pure thickness-shear vibration is excited in a crystal plate, displacements of particles are parallel to the surfaces of the plate. Particle velocities only change along the plate thickness and do not have in-plane variations. A common quartz plate for resonator applications has a thickness of a few tenths of a millimeter, a diameter of a few millimeters, and a fundamental thickness shear frequency of the order of a few to tens of MHz. The thickness shear modes of a quartz plate are usually employed for the high frequency resonators. When a voltage is applied, the corresponding electrical field is parallel to the resonator plate thickness. Hence, the thickness shear mode, which appears due to piezoelectric properties and the crystalline orientation, consists of shear deformation of the crystal in the X-direction. The resulting vibration has a wave vector perpendicular to the surfaces [59, 60], as shown in Figure 2-3 in section 2.2.1.

2.1.2 Lithium niobate and periodically poled lithium niobate.

Lithium niobate (LN) has been intensively studied and applied in technology [61-63] since it was synthesized in 1965 by Fedulov in the USSR and by Ballman in the USA. On the other hand, despite that extensive research, new properties have been revealed year by year. At room temperature, LN has relatively large magnitude of remnant polarizations: 78±3 μC/cm^2 [64, 65]. Large magnitude of polarization generates large surface polarization charge.

LN Crystal Structure: All the unit cell parameters were established in 1966 by Abrahams *et al.*. The parameters of LN unit cells in a hexagonal basis are as follows: $c_H = 13.8631 \pm 0.0004$Å and $a_H = 5.14829 \pm 0.00002$Å. In a rhombohedral basis, the parameters are: $a_R = 5.4944$Å, and $\alpha = 55^o 52`$. Figure 2-2 shows the crystallographic structure of LN. Ideally, the stacking sequences along the c-axis are three types of octahedral, which are LiO_6, NbO_6 (TaO_6) and $\square O_6$, where the □ represents a vacancy. The Li^+ and Nb^+ ions are located along the polar *c*-axis and sit between the oxygen layer planes. Li^+ and Nb^+ ions can only be disturbed from the centrosymmetric position along the c-axis. Therefore, the resulting spontaneous polarization directed along the *c*-axis, and only antiparallel (180°) domains can be created in LN crystals.

The ferroelectric phase transition in LN crystal is connected with the displacement of the lithium and niobium ions. In the ferroelectric phase, the cations are shifted from the centers of the octahedral. The layered oxygen planes are at a distance of 2.310Å form each other. The niobium ion is 0.897Å from the nearest oxygen plane while the lithium ion is 0.714 Å. The oxygen octahedra are deformed, and the cations are not located at the centered of oxygen

octahedra. The Li^+ ion is further from the center than the Nb^+ ion because of the difference in bond strengths, i.e. the Li-O bond is weaker than the Nb-O bond [66, 67]. When the crystal is heated above Curie temperature T_c, the Li^+ ions are supposed to move towards the nearest oxygen plane, and Nb^+ ions move toward the center of the oxygen octahedral. The movement of cations reduces the net polarization, and the LN crystal transitions from the ferroelectric phase to the paraelectric phase.

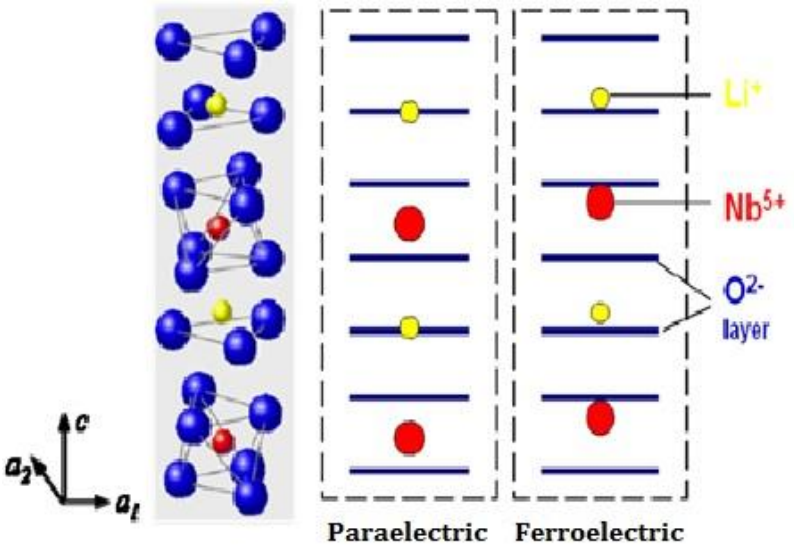

Figure 2-2. Crystallographic structure and relative positions of ions in lithium niobate. The stacking sequence of the unit cell is LiO_6 and NbO_6 (TaO_6). The Li^+ and Nb^+ ions are located along the polar *c*-axis and sit between the oxygen layer planes.

LN electrical Permittivity : The connection between the electric flux density and electric field is represented by $D = \varepsilon E$, where ε is a second-rank permittivity tensor. In the ε tensor of LN, the crystal has the only non-zero diagonal elements. In the places perpendicular to the c-axis, the permittivity components have the same magnitude due to the symmetry about the *c*-axis. Therefore, the permittivity tensor can be characterized by a 3×3 matrix:

$$\varepsilon_{ij} = \begin{bmatrix} \varepsilon_{11} & 0 & 0 \\ 0 & \varepsilon_{11} & 0 \\ 0 & 0 & \varepsilon_{33} \end{bmatrix}$$

Measured values of $\varepsilon_{11}/\varepsilon_0 \cong 28.1$ and $\varepsilon_{33}/\varepsilon_0 \cong 84.1$ [68] are used in our later research work of acousto-electric impedance calculations of the PPLN thin plate.

LN piezoelectric effect :The LN crystal is also a piezoelectric solid. The induced polarization and surface charge occur under applied mechanical stress. The connection between induced polarization and applied stress is denoted by $P = T \cdot d$, such that P is the induced polarization, d is a third-rank piezoelectric tensor, and T is the applied stress. The tensor d_{ijk} contains only 18 independent components and can be written as a 3×6 matrix. The jk subscripts reduce to a single subscript, as explained in Table 1, for simplifying the tensor representation. Thus the piezoelectric tensor can be written as [68]:

$$d_{ijk} = \begin{bmatrix} 0 & 0 & 0 & 0 & d_{15} & -2d_{22} \\ d_{22} & d_{22} & 0 & d_{15} & 0 & 0 \\ d_{31} & d_{31} & d_{33} & 0 & 0 & 0 \end{bmatrix}$$

Periodically poled lithium niobate (PPLN): Periodically poled lithium niobate is an artificially engineered material in which domain inversion is usually attained through electrical poling techniques [67]. PPLN is widely used in the field of nonlinear optics, which includes quasiphase-matched second harmonic generation [67] and optical parametric oscillation [68]. Domain inversion merged with low loss optical waveguides has been exploited in integrated devices. In acoustics, PPLN enables the possibility of induced electromechanical coupling in new configurations [69], such as acoustic superlattices. It is significantly different from more common integrated transducers [70] or bulk wave resonators [71] in a uniform piezoelectric medium.

In an acoustic superlattice structure, acoustic waves can be excited using uniform electrodes, instead of periodic electrodes, similar to the one used in the integrated transducers. Domain inversion certainly allows switching the sign, from positive to negative, of all odd rank tensors, specifically of the piezoelectric tensor (e_{mij}), from one domain to the following, while keeping all even rank tensors, such as permittivity (ε_{im}) or elastic constant (c_{ijkl}), remain unchanged. Consequently, the application of a uniform external electric field to the periodic structure will put the domain walls into a periodic strain, which will effectively result in elastic wave generation [69].

2.2 Samples under testing.

This section presents the samples under testing in this research. A total of four resistors, capacitors, and inductors are provided as calibration samples for the impedance and phase measurements that take place later in this dissertation. Two main samples are used and presented in separate subsections. Firstly, a single quartz sample with laboratory name (4YQ-9M7). Secondly, a periodically poled lithium Niobate wafer that has been fabricated in the laboratory [30]. Two samples with the following laboratory names (MD3B) and (MD3B-NC) are presented in details.

2.2.1 Y-cut quartz

Y-cut quartz crystal resonators are engaged in this dissertation. A pair of circular electrodes is placed on the main surfaces of the disk so that the resulting electrical field is parallel to the resonator plate thickness. The sample (4YQ-9M7) is shown in Figure 2-3. It consists of a circular quartz plate and two metallic electrodes made of gold [56].

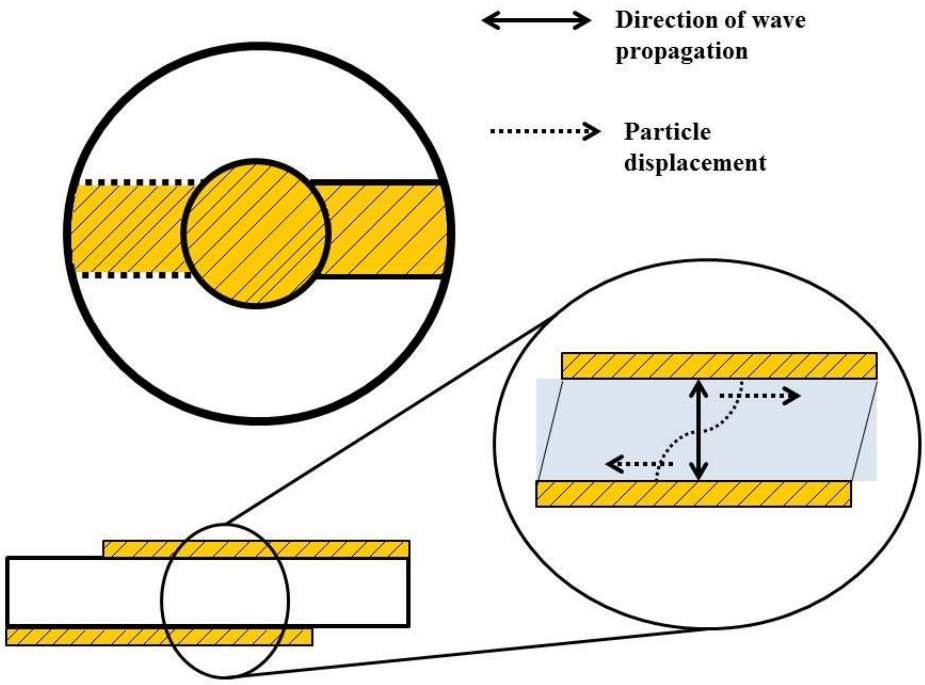

Figure 2-3. shows the structure of a quartz crystal resonator.

2.2.2 Periodically poled lithium niobate (PPLN)

The geometric model of the ferroelectric phononic superlattice is shown in figure 2-4. The Z-cut crystalline plate of 3m-symmetry consists of piezoelectric domains with opposite polarization along the X-axis. The PPLN sample consists of 44 domain pairs. Domains of A type, denoted as A in Figure 2-4, are polarized upward and have a positive piezoelectric constant. The domains of B type, denoted as B in figure 2-4, are inversely polarized and have a negative piezoelectric constant. The length of all domains is 0.45mm. Therefore, the periodicity *L* of the structure is A+B, and it is of 0.9mm length. This alternating-sign piezoelectric constant $e^{\pm}(x)$

reflects the fact that the same mechanical strain generates opposite electric fields in the A and B domains. The total length of the PPLN sample is the periodicity multiplied by the number of domains, which gives 39.5mm along the X-axis. In our case the PPLN width is 29.5 mm along the Y-axis. The thickness of the PPLN is 0.5mm along the Z-axis. The single crystal wafer is produced by MTI Corporation (Richmond, CA). The PPLN sample was fabricated in our laboratory.

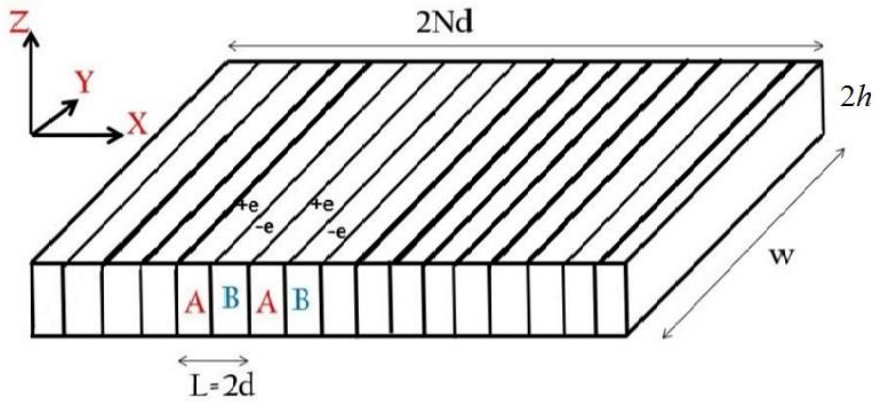

Figure 2-4. PPLN structure consisting of opposite polarized domains A and B. Sample length is $2Nd$, width is w and thickness is $2h$.

Buffer zones shown in Figures 2-5 and 2-6 are next to the PPLN structure. The purpose of these zones is to protect the PPLN structure from damage or crystal breaking. The buffer zones are unpoled Z-cut LiNbO3 crystal. This brings the final dimensions of the sample to the following: total length is 50mm, total width is 40mm, and the plate thickness is 0.5mm.

In the next step, the metal electrodes are deposited into the sample MD3B**,** normal to the X-axis as shown in Figure2-5. The second sample, MD3B-44, was also fabricated in the laboratory. Crystal structure of ZX-cut PPLN plate and buffer zone was used. The electrodes in this sample were placed on the top of the crystal plate, covering a small surface area of the buffer zone. The sample MD3-44-NC is shown in Figure 2-6. In this sample, the electrodes are covering more surface area of the crystal in comparison with MD3B-44, and they are closer to the PPLN zone. The experimental measurements are taken from the samples installed in a metal-grounded housing for minimizing possible influence of the air field on the experimental data. In addition to that shield, a conductor at ground potential, is surrounding the sample to reduce the electrostatic interference. Table 2 provides the reader with a detailed summary of the samples used in this research.

Sample number	Laboratory name	Material	Sample characteristics
1	4QY-9M7	Y-cut Quartz single crystal	Fundamental resonance at 9.77MHz
2	MD3B	PPLN	Figure 2-7 (Edge contacts)
3	MD3B-NC	PPLN	Figure 2-8 (Surface contacts)
4	R1, R2, R3, R4	Resistors	100-250 KOhms

Table 2. Samples under investigations throughout the research.

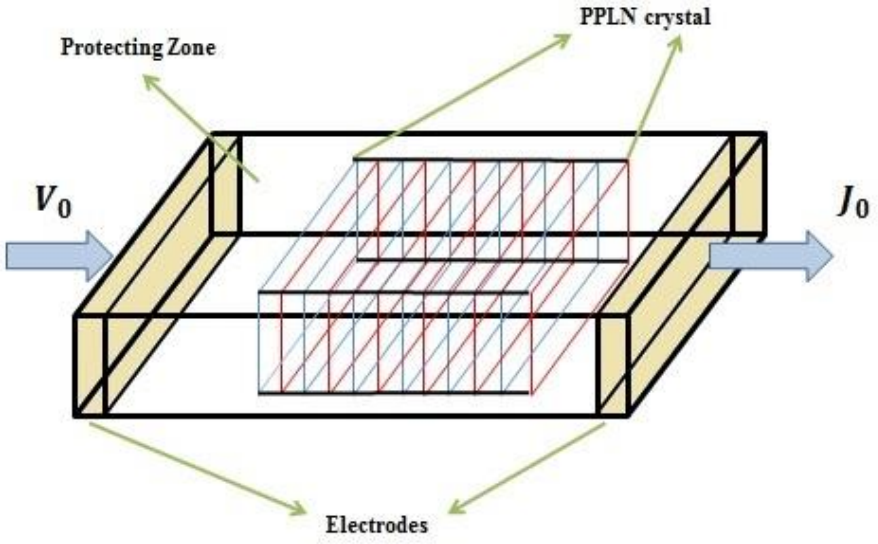

Figure 2-5. The MD3B sample structure, which consists of PPLN zone and buffering zone. N=44 domain pairs, the sample total length is 50mm, the total width is 40mm and the thickness is 0.5mm. Electrodes are connected to the sample at the edges of the plate.

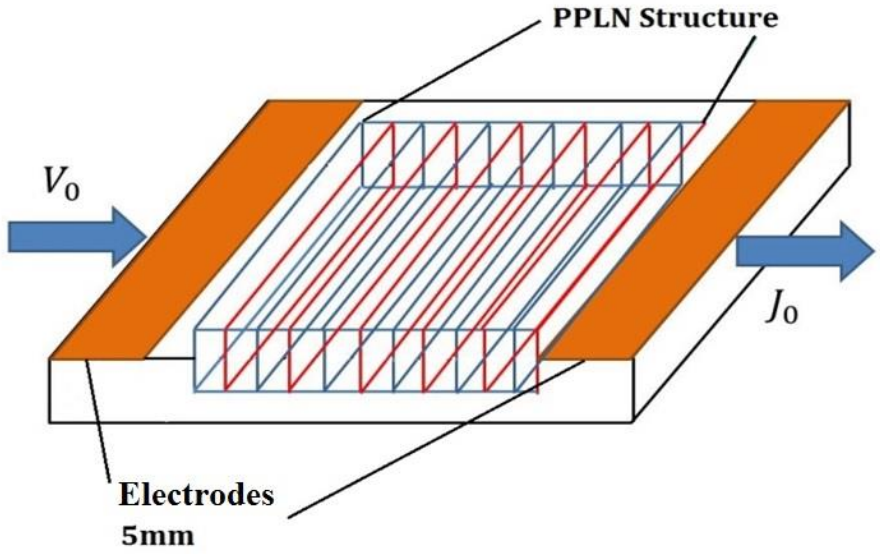

Figure 2-6. The MD3B-NC sample structure, which consists of a PPLN zone anda buffering zone. *N*=44 domain pairs, the sample total length along the X-axis is 50mm, the total width along the Y-axis is 40mm and the thickness is 0.5mm. Electrodes of length 5mm were connected to the sample at the surface.

2.3 Experimental methods for impedance and its phase measurements of FPS

2.3.1 Vector voltmeter with Function Generator (VVM & FG)

The measurements aparatus is presented in Figure 2-7. Alternating voltages (and currents) are often characterized as complex numbers consisting of a magnitude and a phase, with the phase being measured relative to some desired reference. Many instruments exist that can display the voltage amplitude and phase of a signal across a wide range of frequencies. One of those instruments is known as a Vector Voltmeter (VVM). The phase and amplitude as a function of frequency can be obtained in principle by taking the Fourier transformation of the signal and reading the amplitude and phase across the continuum of frequencies. The VVM is able to measure the real and imaginary parts of the voltage signal. To determine the real part of the voltage vector at a given frequency *f,* the signal is first down-converted by mixing with a local oscillator signal $\mathrm{Cos}(2\pi \mathrm{ft})$. This mixing of the signal recenters the frequency component of interest at 0 Hz. The resultant signal is low-pass filtered, digitally sampled, and averaged. The digital sampling and averaging allows the amplitude of the newly created 0-Hz component to be evaluated. The imaginary part is obtained in a similar way by mixing the signal with $\mathrm{Sin}(2\pi \mathrm{ft})$, low-pass filtering, digitally sampling, and again averaging the samples.

The Vector voltmeter for example, can measure complex or vector parameters such as impedance or admittance, amplifier gain and phase shift, complex insertion loss or gain, complex reflection coefficient, two-port network parameters, and filter transfer functions. Consequently, simultaneous measurements of voltage and phase have not always been easy to make. Most

systems which are able to measure phase angles require several control adjustments for each measurement, and many of them are limited in frequency range, sensitivity, and dynamic range.

The VVM, on the other hand, operates over the frequency range of 1MHz to 1GHz. It has high sensitivity and wide dynamic range. The phase resolution is 0.1^0 at any phase angle and all frequencies. The VVM operates with the simplicity of a voltmeter. The operator merely selects appropriate meter ranges, installs two probes to the points of interest and reads voltage and phase on two meter windows.

The VVM has nine voltage ranges with sensitivities of 100 microV to 1V rms. Its dynamic range is 95 dB, which means that it can measure gains or losses of up to 95 dB. As a phase meter, the VVM will measure phase angles between $+180^0$ and -180^0. The phase resolution is 0.1^0. Phase readings are independent of the voltage levels in the two channels. The reference signal for the phase measurement is channel A. The Vector voltmeter provides the ratio of the channel-A voltage to that of channel-B. In this case, we have the ratio (*VA/VB*). In the impedance measurements, the amplitude (*VA*/*VB*) ratio is used. A VVM typically provides a direct measure of the phase angle.

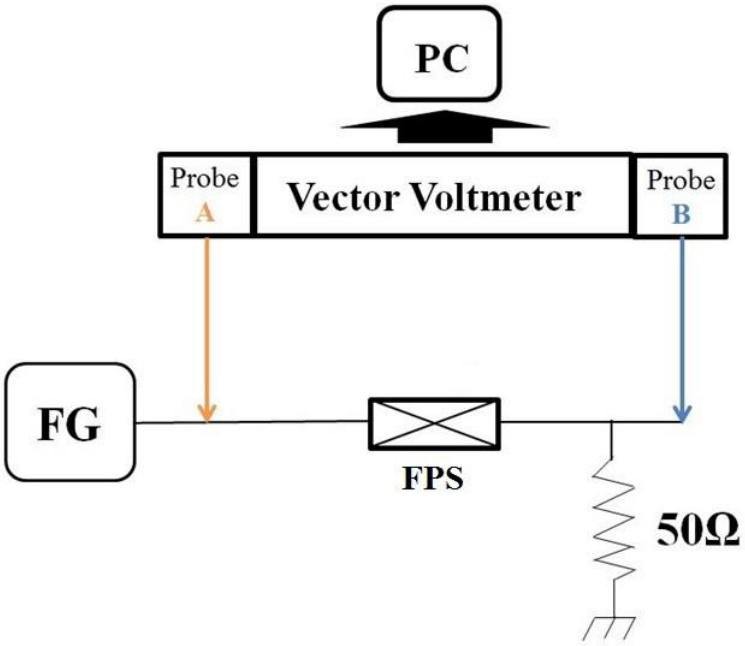

Figure 2-7. The experimental setup for measuring acousto-electric impedance by vector voltmeter and a function generator (FG) with an applied voltage of 1.0 Volts.

2.3.2 Digital Oscilloscope with Function Generator (OSC. & FG)

The method is depicted in Figure 2-8. The Digital oscilloscope (TDS2014B) provides a simple means for measuring the phase difference between two sinusoidal signals. The input signal is applied to Channel one of the TDS and the output to Channel two. The phase difference is the time delay between the two waveforms measured as a fraction of the period. The result is

expressed as a fraction of 360° or of 2π radians. That is, if the time delay is 1/4 of the period, then the phase difference is 1/4 of 360°= 90°. If the waveforms are not sinusoidal but are periodic, the same procedure can still be applied. The phase difference is just expressed as a fraction of the period or as a fractional part of 360°. Care must be taken with direct oscilloscope methods if noise is present. In particular, the noise can cause triggering difficulties that would make it difficult to accurately determine the period and/or the time delay between two different waveforms.

The setup in Figure 2-8 is used to measure V_1, V_2, and the angle, Φ, between them – the phase of V_2 relative to V_1. Using an oscilloscope the peak-peak amplitude of V_1 and V_2 can be measured. The ratio of V_1 to V_2 is used in the impedance measurements. The phase angle, Φ, (between the voltages, not the angle of the impedance) can be determined by triggering the scope on V_1 and measuring the time difference between the zero crossings. The time difference can be related to the phase angle shift using the following equality (2.1):

$$\Phi = (\text{time difference in seconds}) \times 360 \times (\text{frequency in Hz.}) \quad (2.1)$$

In order to measure an impedance *Z*, one should know the complex amplitude *V* of the voltage across the impedance for a given complex amplitude of the current *I* through the impedance. However one is only able to measure voltages by the oscilloscope. This problem can be avoided since it is possible to measure two voltages concurrently relative to a common zero (ground). The unknown impedance (crystal) is placed in series with a known auxiliary resistor R (50-Ohms), as shown in Figure 2-8.

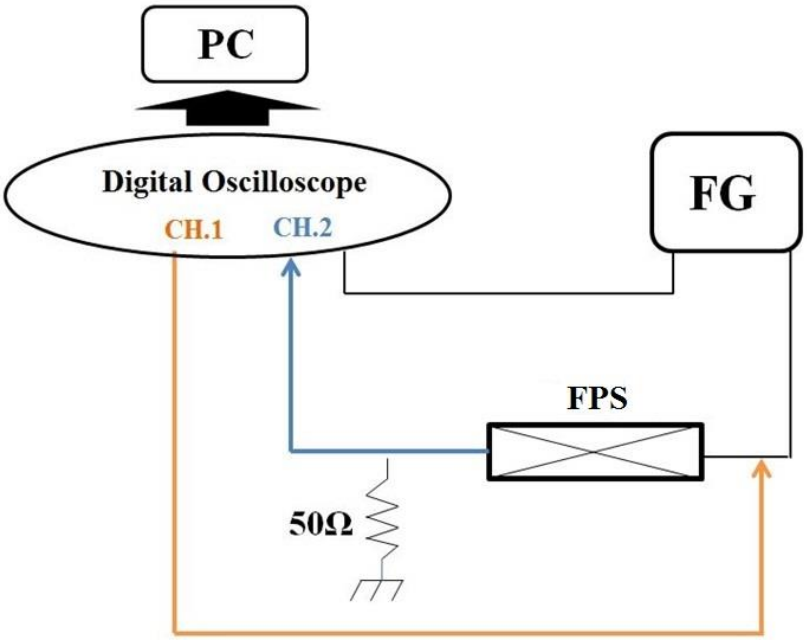

Figure 2.8. The experimental setup of measuring acousto-electric Impedance by using a Digital Oscilloscope (TDS2014B) and a function generator (GFG3015) with applied voltage of 9.0 Volts.

2.4 Impedance and Phase measurements of Quartz crystal

The impedance of quartz crystal (4QY-9M7) is measured in frequency range (9.76-9.79MHz). According to the plate thickness provided by the manufactural company, the fundamental resonance is expected to be close to 9.7MHz. The experiment was done in the lab at room temperature. The disadvantage of the Y-cut is its temperature sensitivity of $100\mathrm{Hz/MHz}\,\mathrm{C}^{0}$ five times the temperature sensitivity of the X-cut.

The methodology explained in the previous section is applied to the quartz plate. The applied voltage in the first method, when the Vector voltmeter and a FG are used, is about 1V. The applied voltage in the second method, when the Digital oscilloscope and a FG are used, is about 9V. We are interested in the frequency range 9.769.79MHz, in which 28 experimental points are measured. The resonance frequency does exist in this frequency range. The measurements taken from quartz were initial measurements in this dissertation. The acoustic impedance and the impedance phase are measured. The theoretical curve calculated for the Quartz resonator is included in this chapter for comparison.

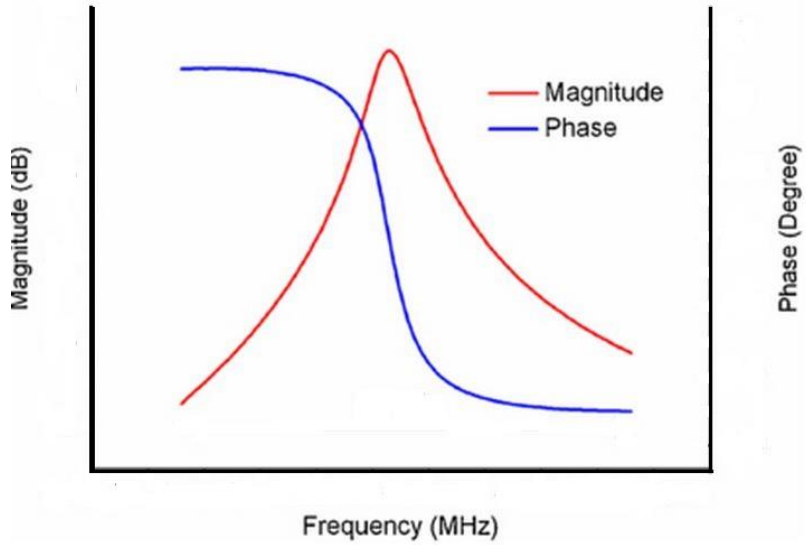

Figure 2-9. General theoretical calculations of the impedance and its phase for quartz plate.

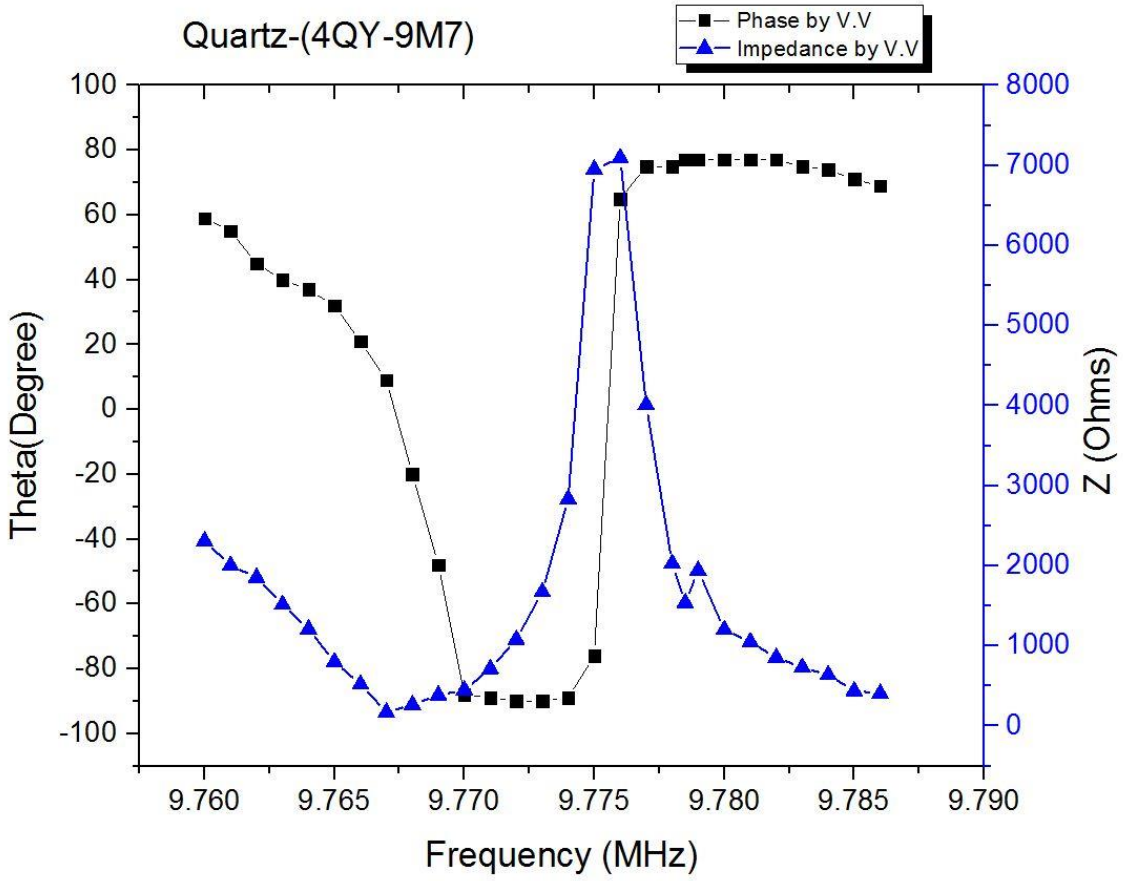

Figure 2-10. Impedance (Z) and phase angle (θ) vs. frequency of the quartz sample (4QY-9M7). Triangles represent Z measurements and squares represent phase measurements. The VVM & FG are used in this experiment. The resonance frequency is about 9.767MHz and the anti-resonance is about 9.776MHz.

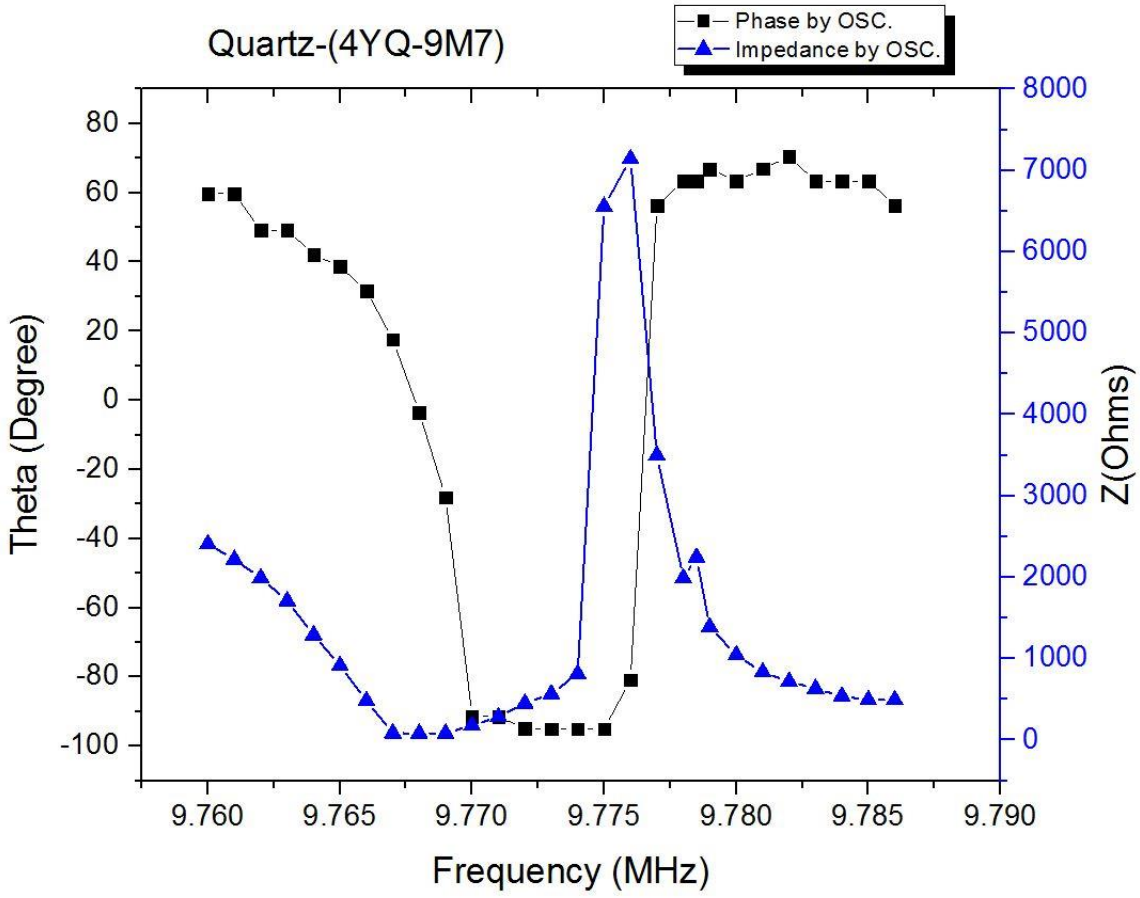

Figure 2-11. Impedance (Z) and phase angle (θ) vs. frequency of the quartz sample (4QY-9M7). Triangles represent Z measurements and squares represent phase measurements. The OSC. & FG method is used in this experiment. The resonance frequency is about 9.768MHz and the anti-resonance is about 9.777MHz.

The results for *Z(f)* and Theta are shown in one Figure. The impedance and phase experimental results are shown in Figure 2-10 using the VVM & FG method. Also Figure 2-11 shows the impedance and phase experimental results using OSC. & FG. The impedance has the resonance frequency at f=9.767MHz, and the antiresonance frequency around f=9.776MHz. At those two frequencies, the phase crosses the zero scale with negative and positive slopes, respectively. The measurements from quartz sample show that our experimental methods and setups work correctly.

CHAPTER III THEORY OF ACOUSTO-ELECTRIC IMPEDANCE IN FPS

Determining the acousto-electric impedance is an important step in understanding the physics of FPS, including practical usage in applications. Therefore this chapter is dedicated to the theoretical calculation of the acoustic vibrations in multidomain ferroelectric structures. These structures are fabricated in thin plates and resonators made of 3m-symmetry materials such as lithium niobate. The numerical evaluation of the acousto-electric impedance of FPS based on $LiNbO_3$ sample is provided.

3.1 Theoretical calculations of acousto-electric impedance of FPS

Piezoelectric media are anisotropic. For any direction of propagation there are three possible acoustic waves with mutually perpendicular vibrations but with different velocities. The periodically poled ferroelectric wafer is a two-dimensional phononic superlattice. The transformations between the electrical and mechanical energies are required in the applications. The ferroelectric phononic superlattice has a number of important solid-state applications. However, the acousto-electric impedance, which is a fundamental physics property of FPS under considerations, has not yet been considered in the literature for two-dimensional ferroelectric structures.

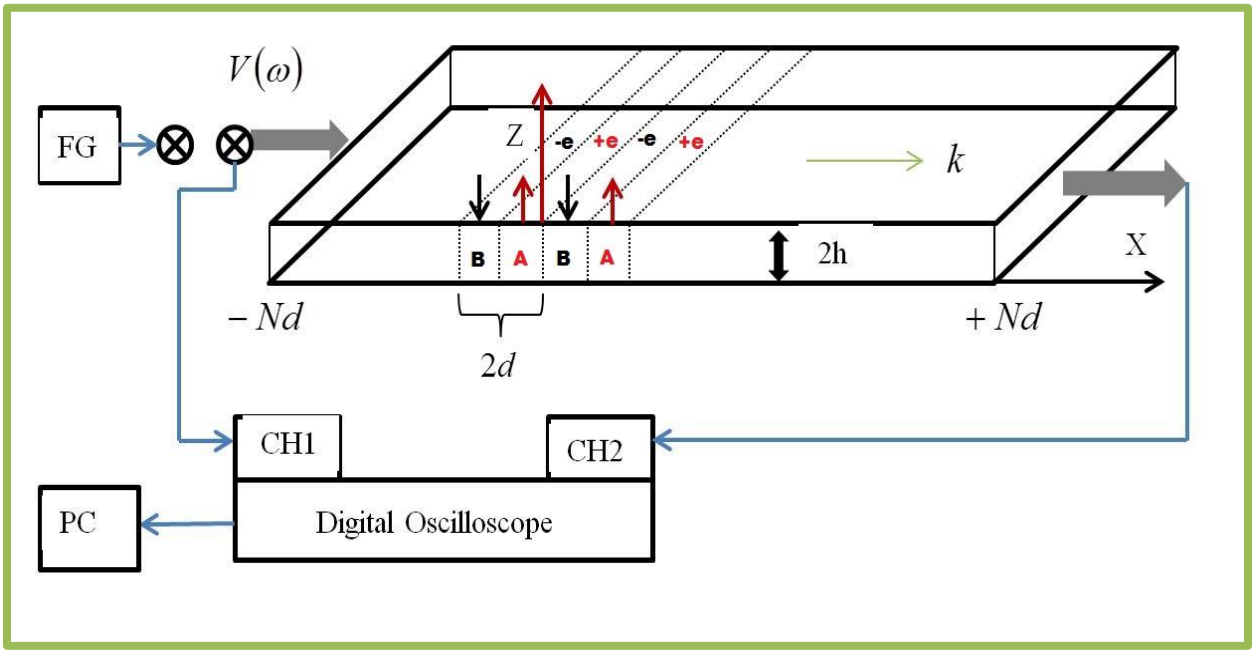

Figure 3-1. Ferroelectric Phononic superlattice consisting of inversely poled domains in the ZX-cut $LiNbO_3$ plate. The periodically poled domains are designated as (A) and (B). Input voltage is applied by a Function Generator (FG) at $x = -Nd$, and the output current is detected at $x = +Nd$ of the sample. Sample thickness is h, domain length is d, and the total length of the sample is $2Nd$.

The geometry of ferroelectric phononic superlattice (FPS) is shown in Figure 3-1. The FPS consists of a collection of inversely poled domains. This collection consists of *N* A-type domains and *N* B-type domains. The total number of inversely poled domains, each of length *d*, is 2*Nd* along X-axis. The inverse polarization is shown by the oppositely oriented arrows ($\uparrow$ and $\downarrow$). Mathematically, this configuration is represented by opposite signs of piezoelectric coefficients in the adjacent domains, $+e$ for A-type domains and $-e$ for B-type domains. This reflects the fact that the same type of mechanical strain generates opposite piezoelectric fields in A and B domains. In this crystalline wave guide, Lamb waves can be excited with longitudinal acoustic displacement A_x, transverse acoustic displacement A_z, and shear waves with acoustic displacement A_y. For purely longitudinal ultrasonic waves, the direction of propagation is along the x-axis with displacement A_x. Therefore Newton's equation can be written in this form

$$\rho \frac{\partial^2 A_i}{\partial t^2} = \frac{\partial T_{ij}}{\partial x_j}. \tag{3.1}$$

In a piezoelectric medium the stress is a function of geometric strain and of the electric field. In the configuration of Figure 3-1, the applied voltage produces an electric field, as well as a mechanical deformation, because of the piezoelectric effect. If the applied voltage signal is small enough, the piezoelectric effect is almost linear. Using this consideration, the basic piezoelectric equations can be established from Gibbs free energy. By neglecting the effect of the temperature and the magnetic field, we can write the equations that describe the piezoelectric effect. Applying an electric field to the plate causes a mechanical stress in the material as described by Equation (3.2). In the reverse piezoelectric effect described by Equation (3.3), the mechanical strain in the material causes an electric displacement. The voltage $V(\omega)$ is applied

along the X-axis. This produces an electric field $E_m(\omega)$ inside the FPS, which in turn generates PAW with acoustic displacement $A_k(\omega)$ and mechanical strain $S_{kl} = (\partial A_k / \partial x_l)$. Therefore, the electric field E_m and the elastic strain S_{kl} are independent variables. Let *D* be the amplitude of the electric field induction produced in the piezoelectric plate by a harmonic electric voltage with circular frequency $\omega = 2\pi \cdot f$. There are four known pairs of equations embedding elastic and piezoelectric tensors [32]. The correct choice of the equations for the case under consideration would be

$$T_{ij} = c^{E}_{ijkl} S_{kl} - e^{\pm}_{mij}(x) E_m \ , \tag{3.2}$$

$$D_i = e^{\pm}_{ikl}(x) S_{kl} + \varepsilon^{S}_{im} E_m \qquad i, j, k, l, m = 1,2,3 \ , \tag{3.3}$$

such that T_{ij} is the mechanical stress tensor, D_i is the electric displacement, c_{ijkl} are the elastic modules tensor components at a constant electric field, $\varepsilon^{S}_{im} = \varepsilon_0 \varepsilon$ is the dielectric constant at constant elastic strain, and $e_{kli}{}^{\pm}(x)$ is the piezoelectric coefficients tensor. For an isotropic piezoelectric material of class 3m-symmetry polarized in z-direction, the material tensors are known from the literature [22]. This piezoelectric vibrator is very thin, with a thickness of a fraction of a millimeter. Therefore the deformation of a piezoelectric material in the direction of the thickness (Z-axis) is very small compared to the other directions and can be neglected.

Moreover, for a one dimensional problem only the deformation of the plate along the length is considered, so spatial derivatives in the Y and Z-directions vanish..Substituting Equation (3.1) into Newton's equation of motion yields the general wave Equation below

$$\rho \frac{\partial^2 A_i}{\partial t^2} = \frac{\partial T_{ij}}{\partial x_j} = \frac{\partial}{\partial x_j}\left(c^E_{ijkl} \frac{\partial A_k}{\partial x_l} - e^{\pm}_{mij}(x) E_m \right), \tag{3.4}$$

where ρ is the crystal density and A_i is the acoustic displacement component. The crystallographic configuration shows more simplifications that can be considered here. For example, the applied electric field along X-axis and the polarized piezoelectric crystal along the same axis would give one term out of the total sum $\sum_{mij}\left(e^{\pm}_{mij}(x) \cdot E_m\right)$. The FPS thickness is smaller than its width and length. In addition, the acoustic wavelength is longer than the plate thickness. Thus in further calculations, the superscripts will be omitted in all tensor components and acousto-electric fields components. Hence, for any acoustic plate mode, one can introduce the effective elastic constant *c*, effective piezoelectric constant *e*, and corresponding electromechanical coupling coefficient *K*, as explained before. Each mode is characterized by its own dispersion curve, phase velocity and group velocities [72]. Then the equation of motion (3.4) can be written in the form

$$\rho \frac{\partial^2 A}{\partial t^2} = \frac{\partial}{\partial x_j}\left(c \ \frac{\partial A}{\partial x} - e^{\pm}(x) E \ \right). \tag{3.5}$$

Along the FPS plate, the piezoelectric constant changes its sign in the neighboring domains as $e^{\pm} = (-1)^N e$. Domain A has a positive piezoelectric constant and domain B has a negative one. Figure 3-2 shows the direction of the spontaneous polarization $\vec{P}_S$ and the sign of the effective piezoelectric constant e.

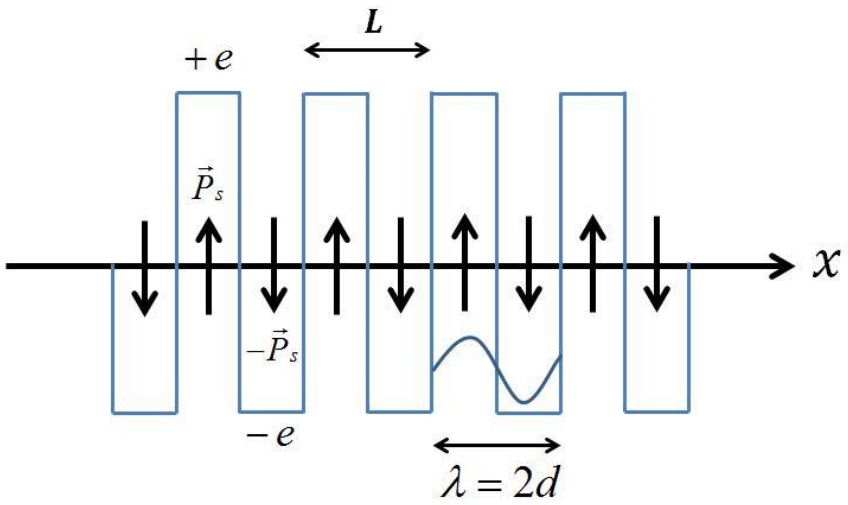

Figure 3-2. The direction of the spontaneous polarization $\vec{P}_s$ and the sign of the piezoelectric constant e of an FPS structure along the X-axis. Polarity of the ferroelectric domains is indicated by arrows. This crystallographic orientation corresponds to the direction of the *Z*-axis.

Consider the acoustic plate mode with longitudinal displacement $A = A_0 \exp^{i(\omega t - kx)}$ along the X-axis. The piezoelectric field is accompanying an acoustic wave with angular frequency ω. The mechanical boundary conditions are given by Equation (3.6) for the plate surfaces $x = \pm Nd$ and $z = \pm h$. The electrical boundary condition to be satisfied is given by Equation (3.7). The equality of the acoustic displacements and stresses at the interface between adjacent domains should also be taken into account.

The mechanical boundary conditions are $\left\{ \begin{matrix} T(x = \pm Nd) = 0 \\ T(z = \pm h) = 0 \end{matrix} \right\}$. (3.6)

The electrical boundary condition is $E(x = \pm Nd) = 0$. (3.7)

The electric field is assumed quasi-static, since the speed of electromagnetic wave is five orders of magnitude higher than the speed of acoustic waves in solids. Also there is no space charge within the medium, so div*D*=0, which is,

$$\frac{\partial D}{\partial x} = \frac{\partial}{\partial x}\left(e^{\pm}(x)\frac{\partial A}{\partial x} + \varepsilon E \right) = 0 \tag{3.8}$$

The acoustic waves propagate in the x-direction, so the longitudinal displacement is given by $A = A_X e^{i(\omega t - kx)}$, such that A_x is the displacement amplitude, ω is the angular frequency, k is the wave vector, and t is the time. Therefore, the acoustic displacement is $A = \frac{-1}{\rho \omega^2}\frac{\partial T}{\partial x}$. The derivative of the displacement vector with respect to position x (Strain) can be substituted in Equations (3.2) and (3.3), as shown in Equations (3.9) and (3.10) below:

$$T(x) = -i\,k\,c\,A - e^{\pm}(x)\,E\,, \tag{3.9}$$

$$D = e^{\pm}(x)\,\frac{T}{c} + \varepsilon E\left(1 + \frac{e^2}{c\varepsilon}\right). \tag{3.10}$$

The electromechanical coupling coefficient is defined as the numerical measure of conversion efficiency between electrical and acoustic energy in piezoelectric media and mathematically is given by:

$$K^2 = \frac{e^2}{c\varepsilon}. \tag{3.11}$$

The electric field E is assumed to be quasi-static, since the speed of the electromagnetic wave is five orders of magnitude higher than the speed of acoustic waves in solids. Then it can be written in term of the stress T, electric displacement D, and the electromechanical coupling coefficient K, as indicated by Equation (3.12) below:

$$E = \frac{D}{\varepsilon(1+K^2)} - \frac{e^{\pm}(x)}{c\varepsilon}\frac{T}{(1+K^2)}. \tag{3.12}$$

The direct way to find the acousto-electric impedance is to use Equation (3.5). Equation (3.12) and the derivative of Equation (3.1) with respect to x can be substituted into Equation (3.4), as shown in Equation (3.13). More manipulations are shown below, in order to give the corresponding differential Equation (3.16):

$$\frac{\partial A}{\partial x} = \frac{-1}{\rho\omega^2}\frac{\partial^2 T}{\partial x^2}, \tag{3.13}$$

$$T = \frac{-1}{\rho\omega^2}\frac{\partial^2 T}{\partial x^2} - e^{\pm}(x)\left[\frac{D}{\varepsilon(1+K^2)} - \frac{e^{\pm}(x)}{c\varepsilon}\frac{T}{(1+K^2)}\right], \tag{3.14}$$

$$T = \frac{-c}{\rho\omega^2}\frac{\partial^2 T}{\partial x^2} - \frac{e^{\pm}(x)D}{\varepsilon(1+K^2)} + \frac{K^2 T}{(1+K^2)}, \tag{3.15}$$

$$\frac{\partial^2 T}{\partial x^2} + k'^2 T + \frac{k'^2 e^{\pm}(x)}{\varepsilon} D = 0 \text{ , such that } k'^2 = \frac{k^2}{(1+K^2)}. \tag{3.16}$$

The procedure to solve this second order differential equation is presented below

$$T_1 = T + \frac{e^{\pm}(x)}{\varepsilon} D, \tag{3.17}$$

$$\frac{\partial^2 T_1}{\partial x^2} + \frac{k^2}{(1+K^2)} T_1 = 0, \tag{3.18}$$

$$T = B\sin\left(k'^2 x\right) + G\cos\left(k'^2 x\right) - \frac{e^{\pm}(x)}{\varepsilon} D, \tag{3.19}$$

such that B and G are constants to be determined by applying the mechanical boundary conditions of stress free surfaces of this periodically poled plate at $x = \pm Nd$. This is shown in Equations (3.16.a) and (3.16.b):

$$x = +Nd \Rightarrow E = 0 = B\sin\left(\frac{kNd}{\sqrt{1+K^2}}\right) + G\cos\left(\frac{kNd}{\sqrt{1+K^2}}\right) - \frac{e}{\varepsilon} D, \tag{3.20.a}$$

$$x = -Nd \Rightarrow E = 0 = -B\sin\left(\frac{kNd}{\sqrt{1+K^2}}\right) + G\cos\left(\frac{kNd}{\sqrt{1+K^2}}\right) + \frac{e}{\varepsilon} D. \tag{3.20.b}$$

The constant G is equal to zero, which follows from the addition of Equations (3.20.a) and (3.20.b). The parameter $B = \dfrac{eD}{\varepsilon \sin\left(\dfrac{kNd}{\sqrt{1+K^2}}\right)}$, which follows from subtracting Equations (3.20.b) from (3.20.a). Moreover, the internal boundary conditions that require equalities of the acoustic displacement and stresses at the interfaces between the adjacent inversely poled domains should be satisfied. The wave numbers at the boundaries of the resonator are k_{01} and k_{02}. The piezoelectric effect vanishes and the wave vector becomes $k_{01} \cong k_1 / \sqrt{1+K^2}$ in the first ABZ and $k_{02} \cong k_2 / \sqrt{1-K^2}$ in the second ABZ as shown in Figure 1-5. Both wave numbers are implemented in the stress equation.

The stress equation as a function of the electric displacement vector can take this form:

$$T = \frac{e}{\varepsilon}\left[\frac{\sin(kx)}{\sin\left(\dfrac{kNd}{\sqrt{1\pm K^2}}\right)} - \frac{e^{\pm}(x)}{e}\right] D(k, N, d, K), \tag{3.21}$$

where the plus sign with the electromechanical coupling factor is for the first acoustic Brillouin zone (ABZ) and the minus sign is for the second ABZ. The piezoelectric constant has a positive magnitude and changes its sign, so the ratio $\left(e^{\pm}(x)/e\right)$ does equal to $+1$ or -1 in the alternating domains throughout the vibrator. The electric field equation in *N*-pair-domain vibrator via electric inductance can be calculated by substituting the stress Equation (3.21) into Equation (3.12),

$$E = \frac{D}{\varepsilon\left(1+K^2\right)} - \frac{e^{\pm}(x)}{c\varepsilon\left(1+K^2\right)}\left[\frac{e}{\varepsilon}D\frac{\sin\left(kx\right)}{\sin\left(\frac{kNd}{\sqrt{1\pm K^2}}\right)} - \frac{e^{\pm}(x)}{e}\frac{e}{\varepsilon}D\right]. \tag{3.22}$$

Then applying the electric boundary conditions of metalized surfaces of this periodically poled plate at $x = \pm Nd$ is shown in Equation (3.23), in which the electric field is a function of electric displacement current:

$$E = \frac{D\left(K,N,k,d\right)}{\varepsilon}\left[1 - \frac{e^{\pm}}{e}\frac{\sin\left(kx\right)}{\sin\left(\frac{kNd}{\sqrt{1\pm K^2}}\right)}\right]. \tag{3.23}$$

The integration of the electric field $E\left(x,\omega\right)$, specified by Equation (3.23) over the superlattice length, is a sum of the particular integrals over each ferroelectric domain. This sum is equal to an applied rf-voltage, which allows for finding a dielectric displacement field $D(\omega)$ as a function of $V(\omega)$

$$V(\omega) = \int_{-Nd}^{+Nd} E.dx = \frac{D(k,N,d,K)}{\varepsilon}\int_{-Nd}^{+Nd} 1 - \frac{e^{\pm}(x)}{e}\frac{\sin\left(kx\right)}{\sin\left(\frac{kNd}{\sqrt{1\pm K^2}}\right)}dx\,. \tag{3.24}$$

The electrical inductance amplitude D_0 strongly depends on the sign switching term in Equation (3.24). The sum over all domains is a result of the integration from the domain number –N at $x = -Nd$ to the domain number N at $x = +Nd$. In reference [71], the acoustic amplitude

was calculated, and a similar equation to Equation (3.24) integral was discussed. The result is also applicable to the present problem. The integration is shown in the following Equation

$$\int_{-Nd}^{+Nd} \frac{e^{\pm}(x)}{e} \sin(kx) dx = \frac{4}{k} \sin\left(\frac{kd}{2}\right) \sum_{m=1}^{m=N} (-1)^m \sin\frac{(2m-1)kd}{2}, \tag{3.25}$$

where $K^2 = e^2/\varepsilon c$ is squared piezoelectric coupling coefficient and $k = \omega/V$ is the wave number of acoustic wave that travels with velocity $(c/\rho)^{1/2}$. The electric displacement (D) as a function of the characteristics of ultrasonic wave is shown below

$$D(\omega, k, N, d) = \frac{V(\omega)\varepsilon}{2Nd} \left[1 - \frac{\sin\left(\frac{kd}{2}\right) \cdot \sum_{m=1}^{m=N} (-1)^m \sin\frac{(2m-1)kd}{2}}{\left(\frac{kNd}{2}\right) \cdot \sin\left(\frac{kNd}{\sqrt{1 \pm K^2}}\right)} \right]^{-1}. \tag{3.26}$$

The rf-current $I(\omega, k, N, K)$ flowing through the dielectric periodically poled superlattice is equal to $\dot{D}(\omega, k, N, K)$, as shown in Equation (3.27). The first term is a capacitive current through FPS capacitance $C_0 = (\varepsilon A/2Nd)$ in which $A = hw$ is the area of the capacitor. The second term represents a contribution of the multidomain superlattice itself due to diffraction; it can be named phononic diffraction term:

$$I(\omega) = hw \frac{\partial D}{\partial t} = \frac{i \cdot h \cdot w \cdot \varepsilon \cdot \omega \cdot V(\omega)}{2N \cdot d} \left[1 - \frac{\sin\left(\frac{kd}{2}\right) \cdot \sum_{m=1}^{m=N} (-1)^m \sin\frac{(2m-1)kd}{2}}{\left(\frac{kNd}{2}\right) \cdot \sin\left(\frac{kNd}{\sqrt{1 \pm K^2}}\right)} \right]^{-1}. \tag{3.27}$$

An important acousto-electric characteristic of FPS is its rf- impedance $Z(\omega)$. The impedance shows the efficiency of acousto-electric transduction in bulk and two-dimensional acoustic superlattice:

$$Z(\omega,k,N,d)=\frac{-2i\cdot N\cdot d}{h\cdot w\cdot \varepsilon\cdot \omega}\left[1-\frac{\sin\left(\frac{kd}{2}\right)\cdot\sum_{m=1}^{m=N}(-1)^m\sin\frac{(2m-1)kd}{2}}{\left(\frac{kNd}{2}\right)\cdot\sin\left(\frac{kNd}{\sqrt{1\pm K^2}}\right)}\right]. \tag{3.28}$$

Acousto-electric impedance $Z(\omega)$ is a function of wave number k, electromechanical coupling coefficient K, number of domain pairs N, electromechanical quality factor Q, and domain length d. Within the frequency domain, $Z(\omega)$ is minimum when the wave number is close to the boundary of the first ABZ, which corresponds to wave length approximately equal to twice the domain length. The term $\sin\left(\frac{kNd}{\sqrt{1\pm K^2}}\right)$ in Equations (3.21) (3.28) is a result of applying the boundary conditions on the metalized edges of the resonator, in which the piezoelectric effect vanishes

In a real crystal, acoustic wave attenuation is taken into account by a complex wave number $k=(k'-ik'')$ and corresponding quality factor $Q=(k'/2k'')$, in which the real part $\mathrm{Re}\,k=(\omega/V)$ depends on the phase velocity V of the acoustic wave, and the imaginary part $\mathrm{Im}k=(\mathrm{Re}\,k/2Q)$ depends on the quality factor Q.

The fact that the stopband is at the boundary of the ABZ leads to splitting in the second term of the Equation (3.28), which must be computed for two parts of A0 mode in the first and

second ABZ, respectively. The final equation of the acousto-electric impedance in the first ABZ and the second ABZ is given in term of the phononic diffraction terms $P_{1,2}$:

$$Z(f,N,K,d,Q)=i\,Z_o\left[1-\left(P_1(k_1,\, f\le F_1)\right)-\left(P_2(k_2,\, f\ge F_2)\right)\right], \tag{3.29}$$

Such that $$P_{1,2}=\frac{\sin\left(k_{1,2}d/2\right)}{\frac{k_{1,2}Nd}{2}\sin\left(k_{1,2}Nd/\sqrt{1\pm K^2}\right)}\sum_{m=1}^{m=N}(-1)^m\sin\left((2m-1)k_{1,2}d/2\right).$$

(3.30)

One can discuss a limiting case such as, when the number of domains is large $N\to\infty$. The length of the FPS is very large that makes the diffraction terms $P_{1,2}$ approach zero, and the impedance is going to be an impedance of a capacitor C_0, then $C_0\to 0$ and $Z(f)$ tends to be large. The velocities of acoustic waves in the first and second ABZ can be calculated as $V_1=2d\cdot F_1=2.934 Km/s$ and $V_2=2d\cdot F_2=3.303 Km/s$ respectively. Physically, the reasons behind the stopband occurrence are as follows:

1) The propagating mode in a piezoelectric plate has mechanical displacement, which is coupled to the piezoelectric field.
2) The expansion and the contraction of the crystal at half-wave length distances caused by the propagation of acoustics waves in alternating regions with positive and negative piezoelectric constant.
3) Resonance occurs if the wave length of the mode is equal to the period of ferroelectric domains. The propagating mode becomes trapped in the periodic domain structure, where its amplitude goes to zero due to out of phase diffraction.

This particularity of multidomain vibrators along with their frequency characteristics may be interesting for MEMS and rf-filter design, especially for super-high- frequencies of gigahertz range. We note that at the gigahertz range frequencies, the ferroelectric domains must be at the nanoscale. The results designated above also remain valid for any low dispersion acoustic wave in the multidomain ferroelectric plate; this includes shear waves as well as high frequency limits when a wavelength is much shorter than plate thickness. The phase speed of another acoustic mode is different. Nevertheless, these results also remain useable for cases other than for the crystallographic orientation of the crystal shown in Figure (3.1). A difference between ZX-cut and another cut will be rotating Z, X, crystallographic axes with respect to laboratory Z, X axes. Consequently changing acoustic and piezoelectric modules in the Equations (3.12)-(3.28) will not change the physical results.

3.2 Computer modeling of the acousto-electric impedance of the MD3B sample

This section is devoted to the computer modeling of the acousto-electric impedance as a function of frequency according to Equation (3.28). MD3B and MD3B-NC samples are used in the calculations. The possible variations of the FPS parameters are also studied computationally. Within the frequency domain, Z(f) is minimum when the wave frequency is in the near boundary(NB) region of the first ABZ, which corresponds to wave number $k = 2\pi/\lambda$, and $\lambda = 2d$.

The theoretical plot of the acousto-electric impedance of MD3B sample is shown in Figure 3-3(a) and 3-3(b) for first and second ABZ respectively. This sample consists of 44 domain pairs and 0.45mm-long domains. The MD3B sample configuration is shown in Figure 2-7. The electromechanical coupling coefficient K is 0.11 and the mechanical quality factor is 110,

both values are provided by the MTI Corporation (Richmond, CA). The zero asymmetrical mode A_0 is propagating along the FPS plate. This mode cannot propagate through the stopband frequency range, because of the diffraction by the interdomain walls. The computations in the following Figures are in arbitrary unit. In the first ABZ, the acousto-electric impedance minimum is in the NB region, in which F_1=3.28 MHz. Similarly, in the second ABZ the acousto-electric impedance minimum is in the NB region, in which F_2=3.65 MHz. The zero antisymmetric mode is propagating along the FPS plate.

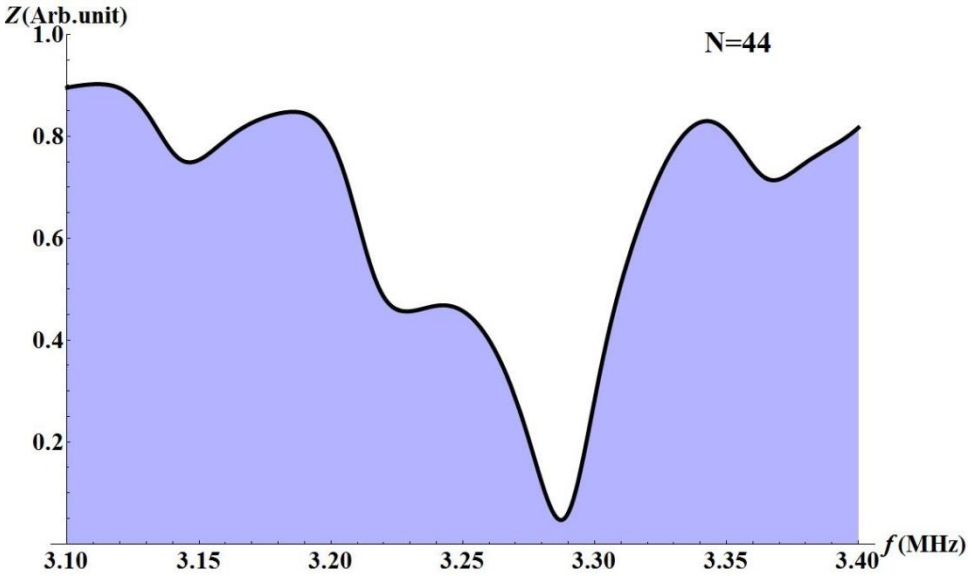

Figure 3-3 (a)

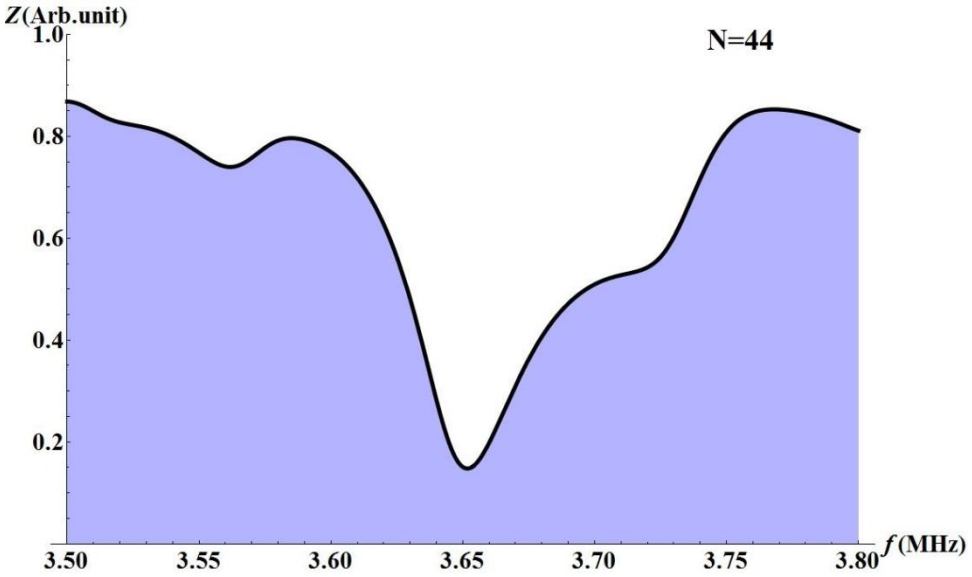

Figure 3-3 (b)

Figure 3-3. The acousto-electric impedance of FPS (Z/Z_0) vs. frequency in (a) the first ABZ and (b) the second ABZ is computed for MD3B sample, which consists of 44-domain pairs and the domain length is 0.45mm. The reference Z_0 is 20-KOhm.

3.3 The influence of domains number on the acousto-electric impedance of FPS

The number of domains has a strong influence on the acousto-electric impedance, which has been investigated numerically for four different structures with 44, 41, 35, and 28 domain pairs. Equation (3.28) and (3.30) are used along with the parameters that are taken from ZX-LN-MD3B sample to estimate the acousto-electric impedance as a function of number of domains. Those parameters include domain length of 0.45mm, sample thickness of 0.5mm, sample width of 30mm, and electromechanical coupling coefficient of K=0.11. The periodic pattern causes reflections and diffractions of waves. Therefore, the larger number of domain pairs, the longer vibrator, which would increase the internal loss. Figures 3-4(a), 3-5(a), and 3-6(a) show the effect of changing the number of domains on the acousto-electric impedance in the first ABZ. While Figures 3-4(b), 3-5(b), and 3-6(b) show the effect in the second ABZ. Mathematica software is used to compute the acousto-electric impedance as a function of number of domains $Z(N)$. The parameters used in this code are as follow: The mechanical quality factor in the first ABZ (Q_1) is 97, the mechanical quality factor in the second ABZ (Q_2) is 108, the phase velocity of A_0 mode in the first ABZ (V_1) is 2.943Km/s, the phase velocity of A_0 mode in the second ABZ (V_2) is 3.303Km/s, the electromechanical coupling coefficient (K) is 0.11, the dielectric constant of $LiNbO_3$ (ε) is 7.52×10^{-7} F/m.

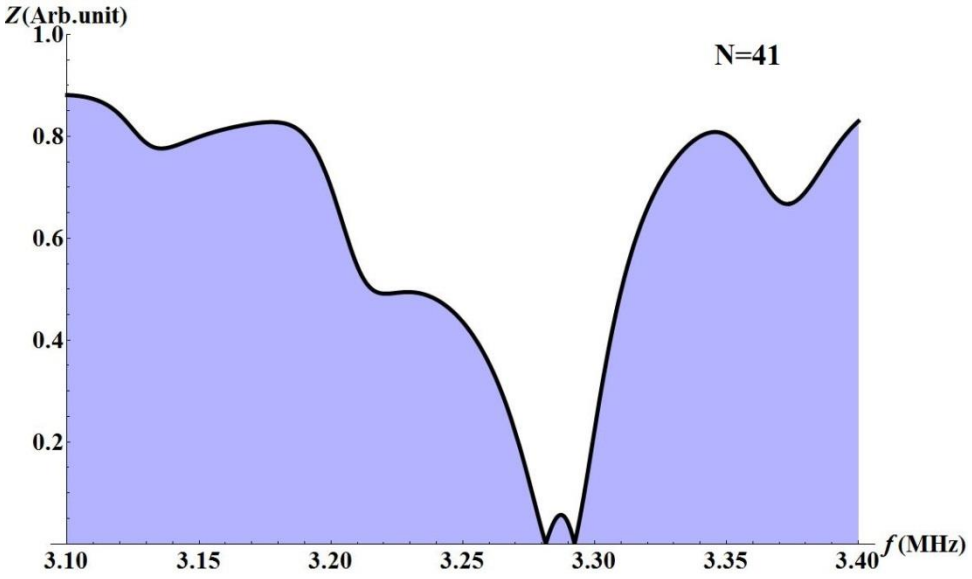

Figure 3-4 (a)

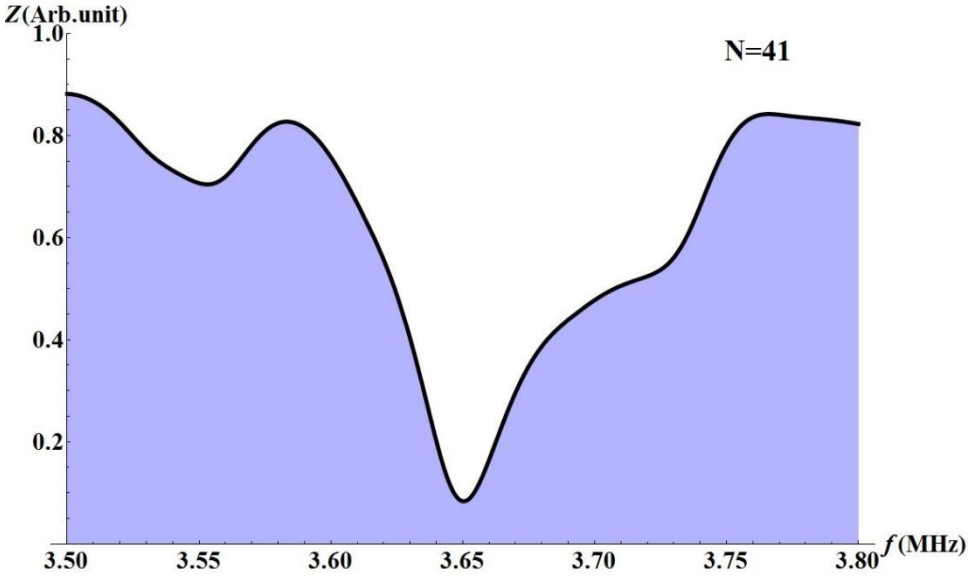

Figure 3-4 (b)

Figure 3-4. The acousto-electric Impedance of FPS vs. frequency in the first (a) and second (b) ABZ, computed for a PPLN sample with N=41, d=0.45mm and K=0.11

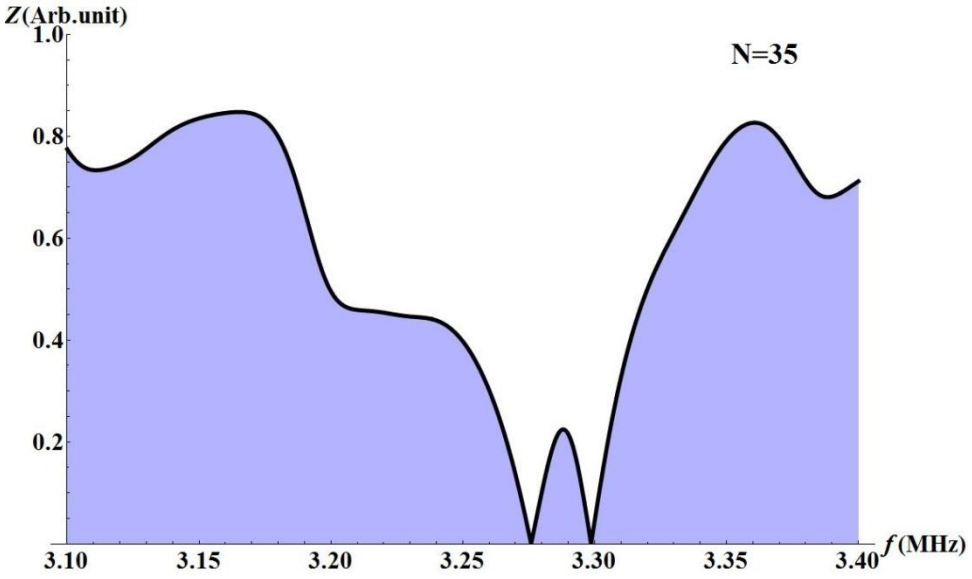

Figure 3-5 (a)

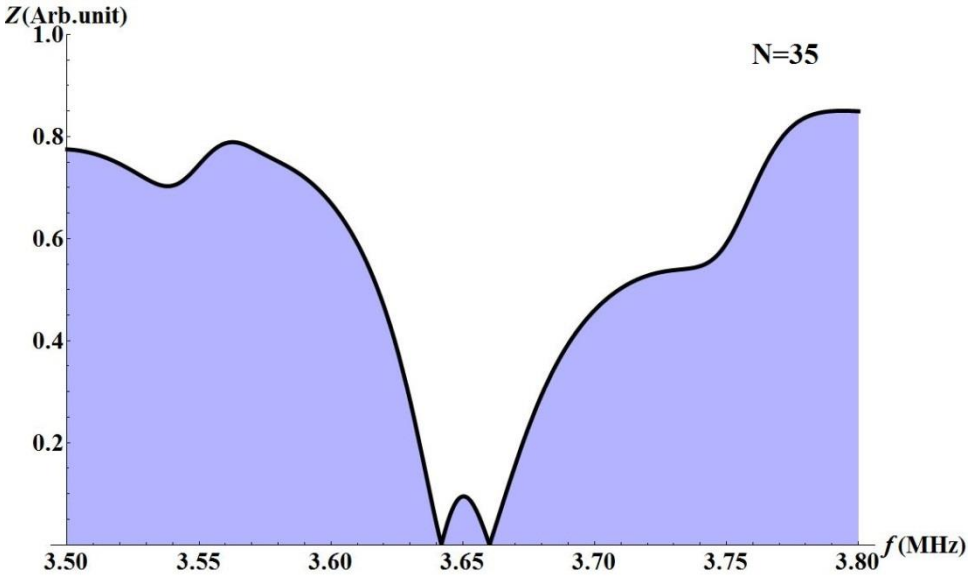

Figure 3-5 (b)

Figure 3-5. The acousto-electric Impedance of FPS vs. frequency in the first (a) and second (b) ABZ, computed for a PPLN sample with N=35, d=0.45mm and K=0.11

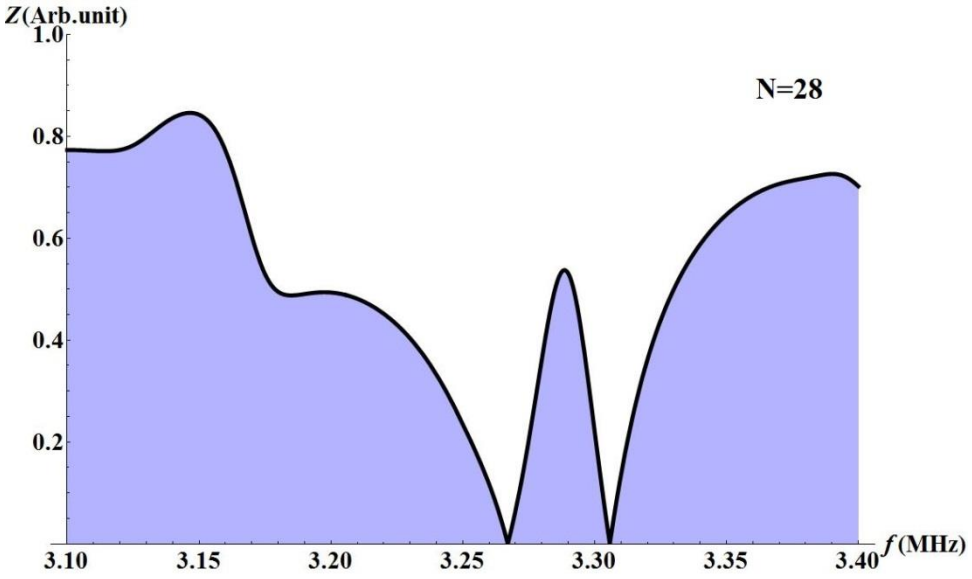

Figure 3-6 (a)

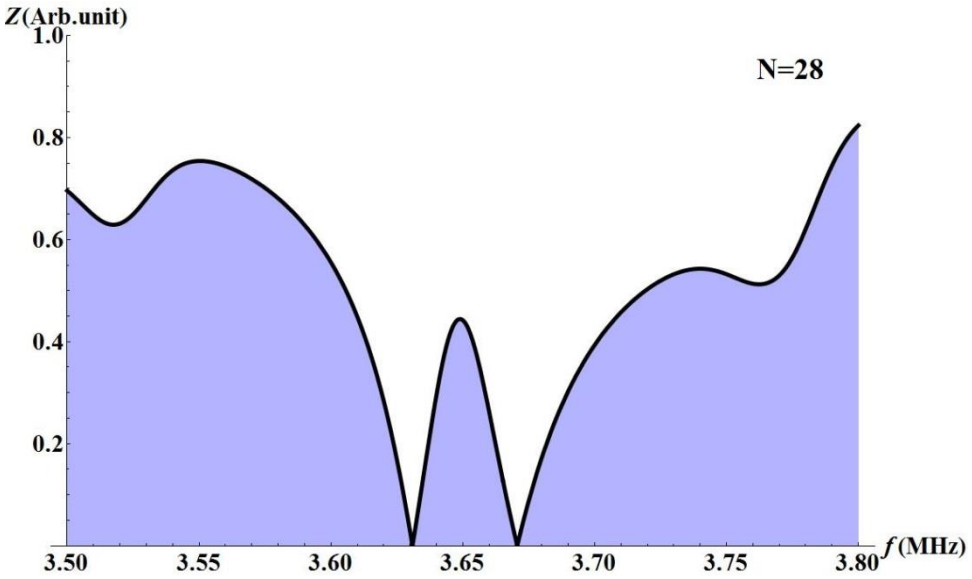

Figure 3-6 (b)

Figure 3-6. The acousto-electric Impedance of FPS vs. frequency in the first (a) and second (b) ABZ, computed for a PPLN sample with N=28, d=0.45mm and K=0.11

The main conclusions out of the computations presented in Figures 3.4-3.6 are the following. The acousto-electric impedance can be controlled by changing number of domains in FPS. One also can predict a phase shift of Z in FPS, due to a change sign of $Z(f,N)$ at certain frequencies and N.

CHAPTER IV EXPERIMENTAL INVESTIGATIONS OF ACOUSTO-ELECTRIC IMPEDANCE *Z(f)* OF FPS.

This chapter narrates the experimental investigations of the acousto-electric impedance and phase shift of FPS. Starting with *Z(f)* measurements taken from MD3B-NC sample, which leads us to improve and extend our investigations. The MD3B-NC sample is used mainly in this chapter to investigate the existence of displacement-components decoupling in complicated regions called transition zones within the near stopband frequencies. Furthermore, impedance phase shift measurements are included as an independent prove of the existence of acoustic displacement decoupling near stopband edges.

3.1 The frequency characteristics of Z(f) from MD3B sample

The acousto-electric impedance measured with the MD3B sample is shown in Figure 4-1 to Figure 4-4 below. The sample structure is explained in details in section (2.2.2). It mainly consists of a PPLN zone, buffer zone and metal electrodes connected at the edges normal to the X-axis. The experimental setup explained in section (2.3.1) is used to take measurements of $Z(f)$ using the vector voltmeter and a function generator (VVM & FG). The applied voltage by FG is about 1.7V. The measurements are taken at room temperature.

The impedance as a function of frequency is shown in Figures 4-1 and 4-2 in the first and second ABZ, respectively. The theoretical calculations-curve of $Z(f)$, by Equations (3.28-3.30), is added to the experimental measurements for comparison. The second method used to investigate the impedance of FPS is explained in section (2.3.2), in which the digital oscilloscope and a function generator (OSC. & FG) are used. The applied voltage from FG is 9.0V. The experimental measurements of the impedance as a function of frequency are shown in Figures 4-3 and 4-4 for this method. Likewise the theoretical calculations of $Z(f)$ is added to the experimental measurements.

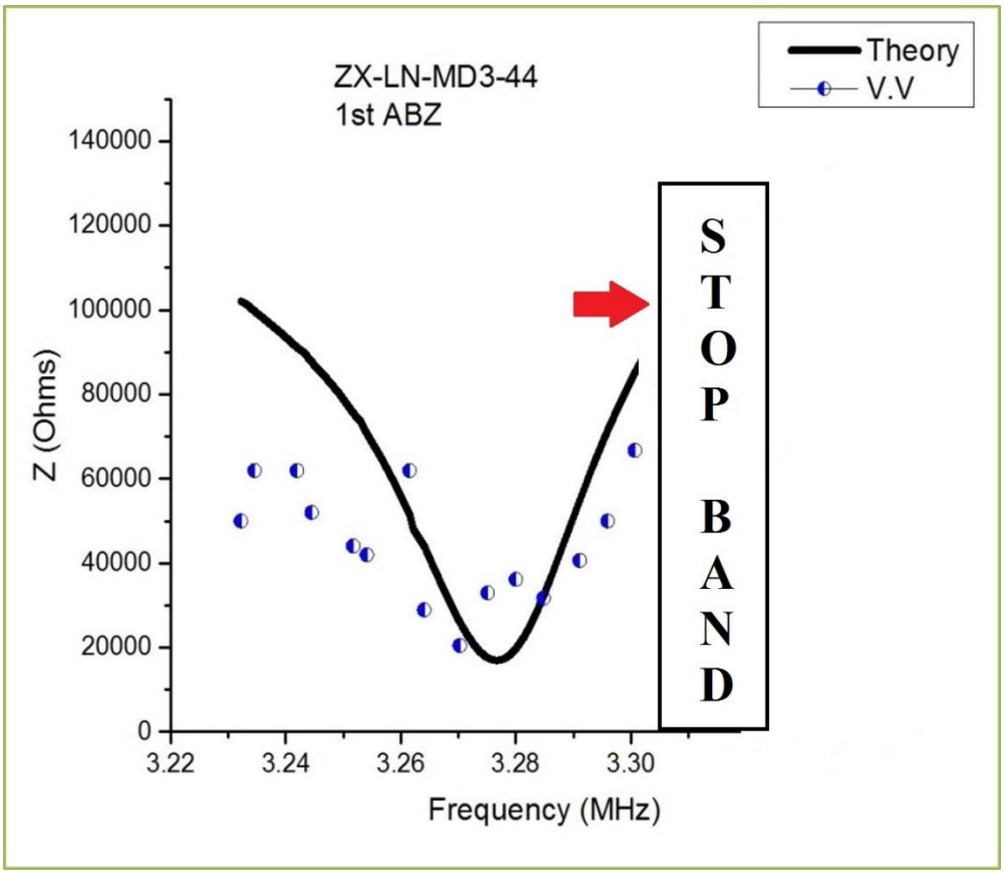

Figure 4-1. The acousto-electric impedance vs. frequency in the first ABZ. The solid line shows the theoretical calculations by Equation (3-28) and points represent measurements taken by VVM & FG from the MD3B sample, which consists of 44 domain pairs of 0.45mm domain- length.

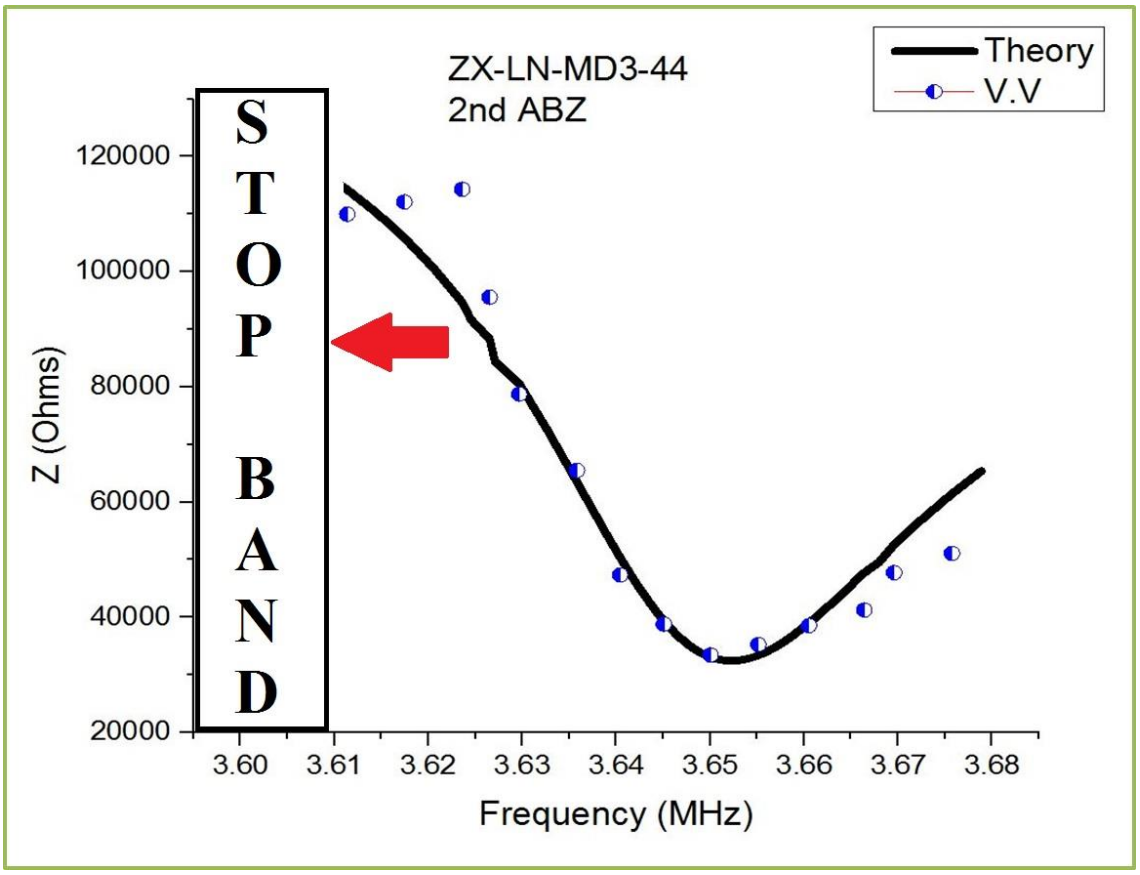

Figure 4-2. The acousto-electric Impedance vs. frequency in the second ABZ. The solid line shows the theoretical plot by Equation (3.28) and points represent measurements taken by VVM & FG from the MD3B sample, which consists of 44 domain pairs of 0.45mm domain-length.

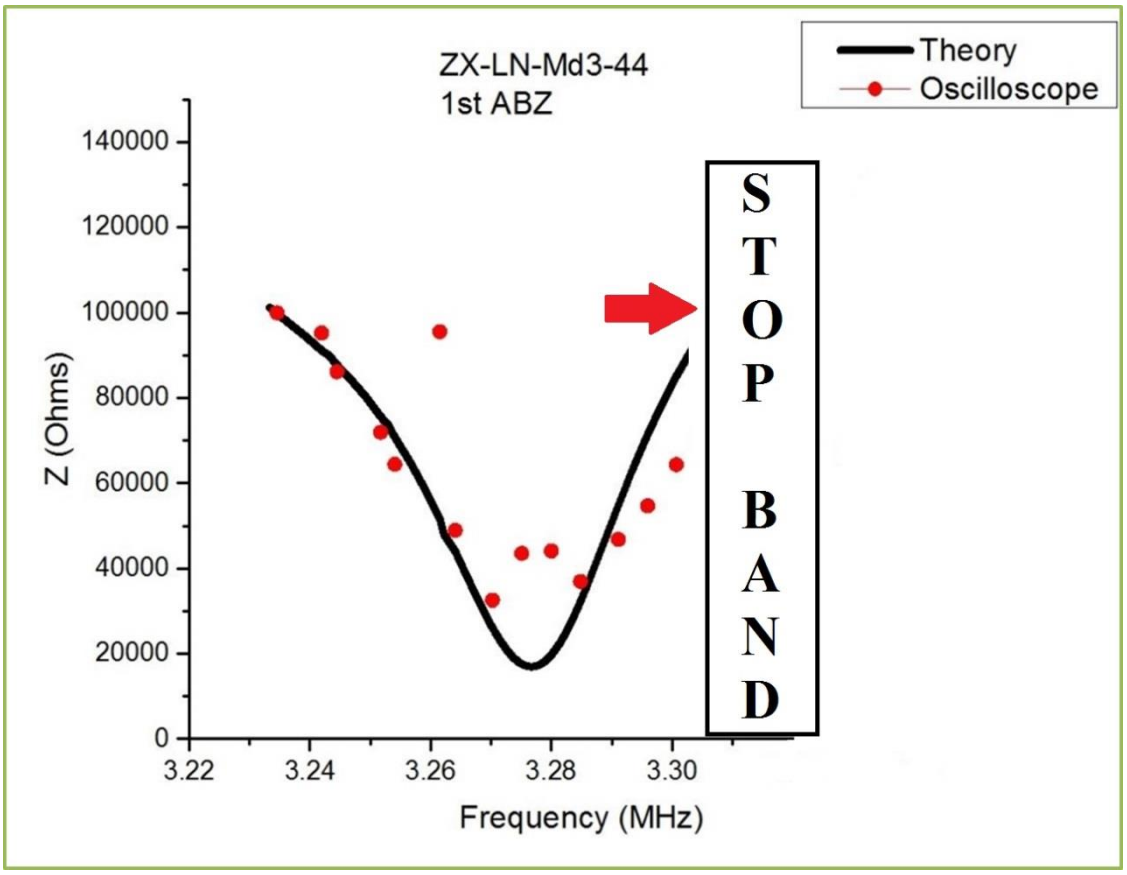

Figure 4-3. The acousto-electric Impedance vs. frequency in the first ABZ. The solid line shows the theoretical calculations by Equation (3.28) and points represent measurements taken by OSC. & FG from the MD3B sample, which consists of 44 domain pairs of 0.45mm domain-length.

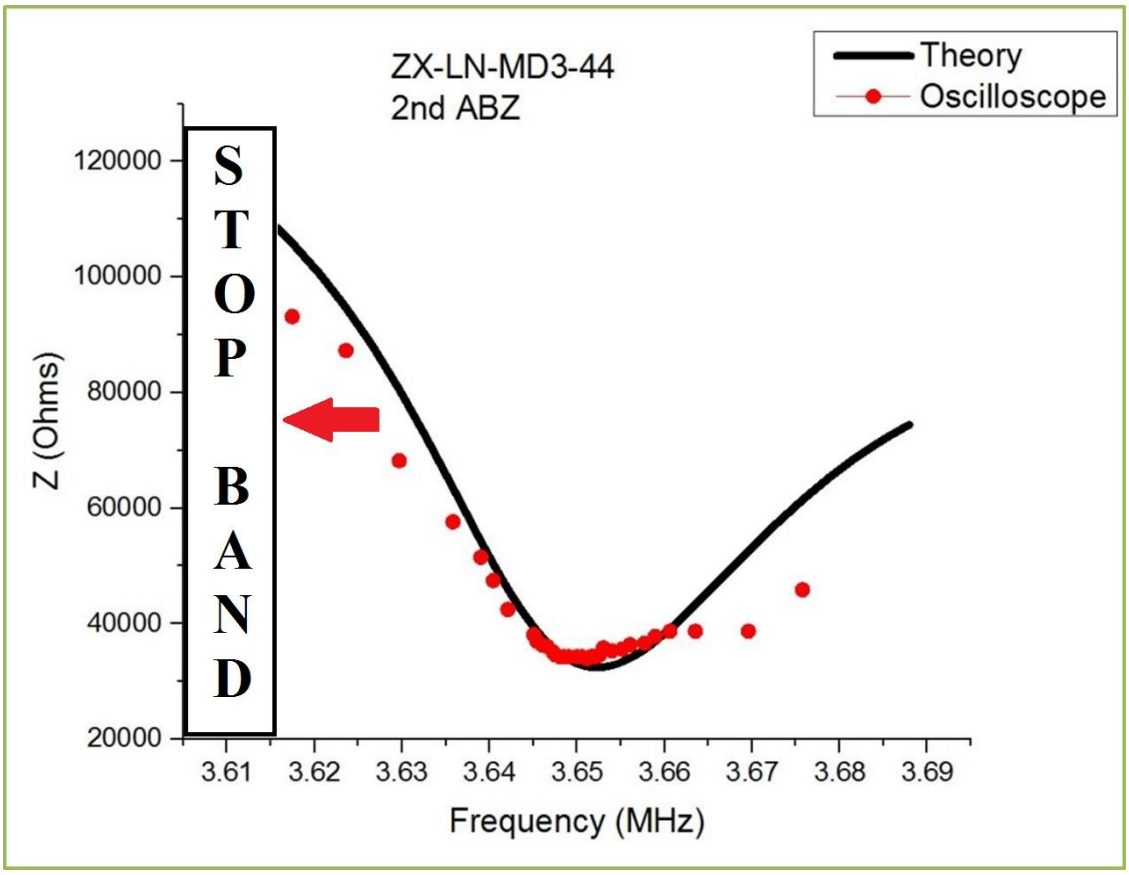

Figure 4-4. The acousto-electric Impedance vs. frequency in the second ABZ. The solid line shows the theoretical calculations by Equation (3.28) and points represent measurements taken by OSC. & FG from the MD3B sample, which consists of 44 domain pairs of 0.45mm domain-length.

One can make the following conclusions out of the results presented above in the Figures 4-1 to4-4.

1. The FPS structure reveals the stopband effect. The width of this band is 380 KHz for the MD3B sample, which is in a good agreement with the definition of the stopband through the dispersion curve of PAW in this FPS (details are in section 1.10).
2. The Figures show that the impedance has minima at frequencies close to the stopband boundaries, that is $F_1 = (3.27 \pm 0.02)$ MHz for m1 mode and $F_2 = (3.65 \pm 0.02)$ MHz for m2 mode; where m1 is the acoustic mode in the first ABZ at $F<F_1$, and m2 is the same acoustic mode but in the second ABZ at $F>F_2$.
3. Figures 4-1 through 4-4 reveals certain discrepancy between experiment and computations. In particular, there are two minima in Figures 4-1 and 4-3 instead of one minimum, and there are two points too far from the theoretical curves in Figures 4-1, 4-2, 4-3, and 4-4. This situation implies the existence of more than one diffraction term in Equation (3.28), and consequently more than one displacement component in an acoustic mode. The PAW modes have mainly more than one displacement component. In particular, the zero antisymmetric mode A_0 has a longitudinal displacement A_X and transverse displacement A_Z. However, the two components A_X and A_Z are usually coupled, and as such piezoelectric interaction may be represented through certain effective displacement A, as in section (3.2). However, the discrepancy between theory and experiment in Figure 4-1 through 4-4 put under a strong question the coupling of

A_X and A_Z components of displacement right near the boundary of the stopband. In the next section (4.2) more details are provided.

4. The experimental and theoretical amplitudes of Z at minimum do not coincide in Figures 4-1 and 4-3. This will be explained in details in section 4.3.

4.2 Decoupling components of acoustic mode displacement near the stopband

The MD3B-NC sample consists of 44 domain pairs, of 0.9mm domain length, and metal contacts that are different from those in the sample MD3B. The sample configuration is shown in Figure 2-6. The change in contact position on the sample is made to get rid of possible influence of protective non-polarized zones on the data taken from FPS. When the electric field is applied to the input electrode, lamb waves are excited to propagate through the FPS. When the wavelength is about twice the domain length, the A_0 mode is split into two parts, m1 and m2, propagating in two different frequency bands. The transition zones are narrow frequency range that bound the stopband in the first and second ABZ as shown in Figures 4-5 and 4-6. As it follows from Figure 1-6, the first transition zone that exists in the first ABZ has a frequency range of about 70-KHz, and extends to the lower limiting edge of the acoustic stopband F1in Figure 4-5, or F_L in Figure 1-5. Similarly the second transition zone exists in the second ABZ and has a frequency range of about 50-KHz. This zone starts from the upper limiting edge of the stopband, F_U in Figure 1-5, or F_2 in Figure 4-6. The mode m1 has two displacement components, A_X and AZ, which decoupled in the transition zone with different velocities, as shown in Figure 4-5. Furthermore, the mode m2 has two components in the transition zone with different velocities in the second ABZ, as shown in Figure 4-6. The so called X-component corresponds to

the acoustic displacement along the X-axis. This displacement component has a propagation velocity of 2.993Km/s in the first ABZ and 3.260Km/s in the second ABZ. The X-component of PAW can propagate at frequencies below F_{1X}=3.28±0.01MHz and at frequencies above F_{2X}=3.67±0.01MHz. The Z-component corresponds to the acoustic displacement along the Z-axis. This displacement-component has a propagation velocity of 2.966Km/s in the first ABZ and 3.259Km/s in the second ABZ. The Z-component of PAW can propagate at frequencies below F_{1Z}=3.26±0.01MHz in the first ABZ and above F_{2Z}=3.66±0.01MHz in the second ABZ.

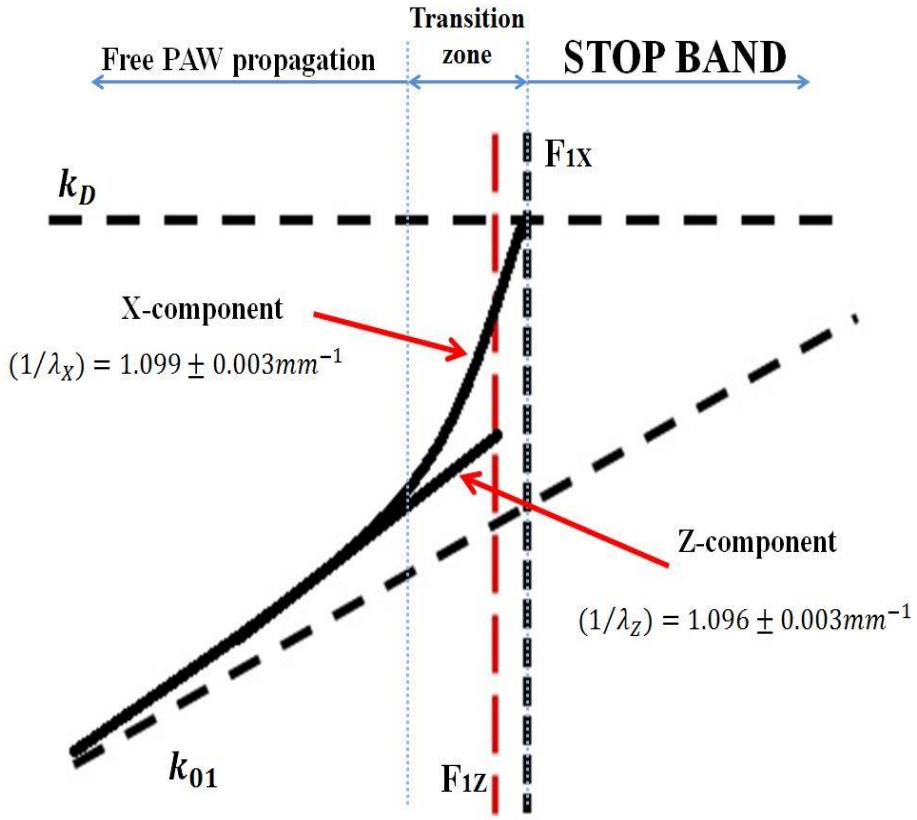

Figure 4-5. Dispersion curve of A_0 mode near lower frequency edge of the stopband, as it follows from the data of Figure 1-6. The mode displacements are decoupled into two components in the first transition zone near stopband. Displacement field of the A_0 mode decoupled into two components including X-component displacement Ax and Z-component displacement Az. The transition zone of 70 KHz wide is very narrow about 2% of F_1=3.27±0.01MHz. Plate acoustic waves with longitudinal displacement (X-component) can propagate at frequencies below F_{1X}. Similarly plate acoustic waves with transverse displacement (Z-component) can propagate at frequencies below F_{1Z}. The k_{01} is a wave vector in the first ABZ of the propagating mode in a wafer without inversely poled domains.

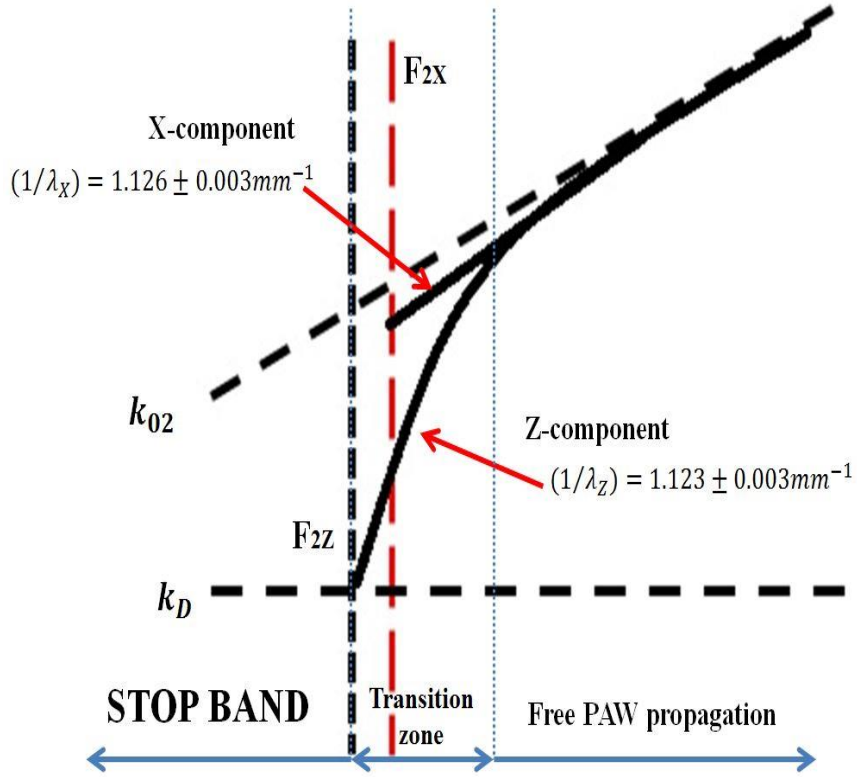

Figure 4-6. Dispersion curve of A_0 mode near frequency edge of the stopband, as it follow from the data of Figure 1-6. Two mode-components exist in the second transition zone of the second ABZ. A_0 mode decoupled into two components, X-component and Z-component, through the transition zone. Plate acoustic waves with longitudinal displacement (X-component) can propagate at frequencies above F_{2X}. Similarly acoustic wave with transverse displacement (Z-component) can propagate at frequencies above F_{2Z}. The k_{02} is a wave vector in the second ABZ of the propagating mode in a wafer without inversely poled domains.

The Equations (3.29) and (3.30) must be modified for the decoupled displacements. The existence of mode-components is taken into account mathematically by splitting each term of Equation (3.30) into two sub terms. One can apply that by taking into consideration the numerical values of F_{1X}, F_{1Z}, F_{2X}, and F_{2Z} of Figures 4-4 and 4-6. The existence of two minima in each zone reflects the fact that the decoupled displacements of A_0 mode in the transition zones have two different velocities. The modified Equations for *Z(f)* under the decoupled A_X and A_Z displacements are as follow for first ABZ:

$$Z_1 = \frac{Z_X(f < F_{1X}) \cdot Z_Z(f < F_{1Z})}{Z_X(f < F_{1X}) + Z_Z(f < F_{1Z})}, \tag{4.1}$$

And for the second ABZ

$$Z_2 = \frac{Z_X(f > F_{2X}) \cdot Z_Z(f > F_{2Z})}{Z_X(f > F_{2X}) + Z_Z(f > F_{2Z})}, \tag{4.2}$$

where each of Z_X and Z_Z is calculated by the Equations of the type of (3.28)-(3.30), but with corresponding frequencies and other parameters.

The computer modeling by Equations (4.1) and (4.2) of the acousto-electric impedance under decoupled A_X and A_Z displacement in the MD3B-NC sample is shown in Figures 4-7(a) and 4-7(b) for the first and second ABZ, respectively. In the numerical modeling of the acousto-electric impedance of FPS, the following parameters are used in the first ABZ: The mechanical quality factor of X-component (Q_{1X}) is 125, the mechanical quality factor of Z-component (Q_{1Z}) is 115, the phase velocity of X-component (V_{1X}) is 2.94Km/s, the phase velocity of Z-component (V_{1Z}) is 2.97Km/s, the electromechanical coupling coefficient of X-component (K_{1X}) is 0.149, and the electromechanical coupling coefficient of Z-component (K_{1Z}) is 0.17. One can use the

following parameters to numerically model the impedance in the second ABZ: The mechanical quality factor of X- component (Q_{2X}) is 102, the mechanical quality factor of Z- component (Q_{2Z}) is 83, the phase velocity of X- component (V_{2X}) is 3.313Km/s, the phase velocity of Z-component (V_{2Z}) is 3.294Km/s, and the electromechanical coupling coefficient of both components are near 0.3.

The difference in quality factor between X- and Z- displacements may be explained by somewhat stronger piezoelectric coupling coefficient K for the Z-component which leads to a stronger attenuation of the Z-displacement. Computations show that actually, the results agree with experiment if $K_{2X} > K_{2Z}$ by some percent near average K_2=0.3. That is why in the calculations we may use K_2=0.3 for both components, because the frequency range of the second transition zone is a way very narrow. If $F>F_{2X}$, then both components A_X and A_Z are coupled and K is the same.

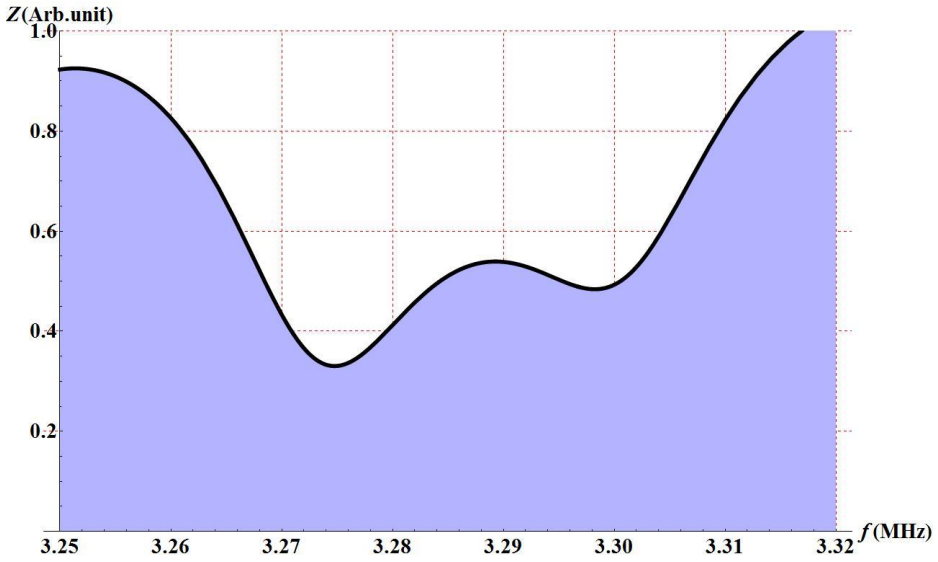

Figure 4-7 (a)

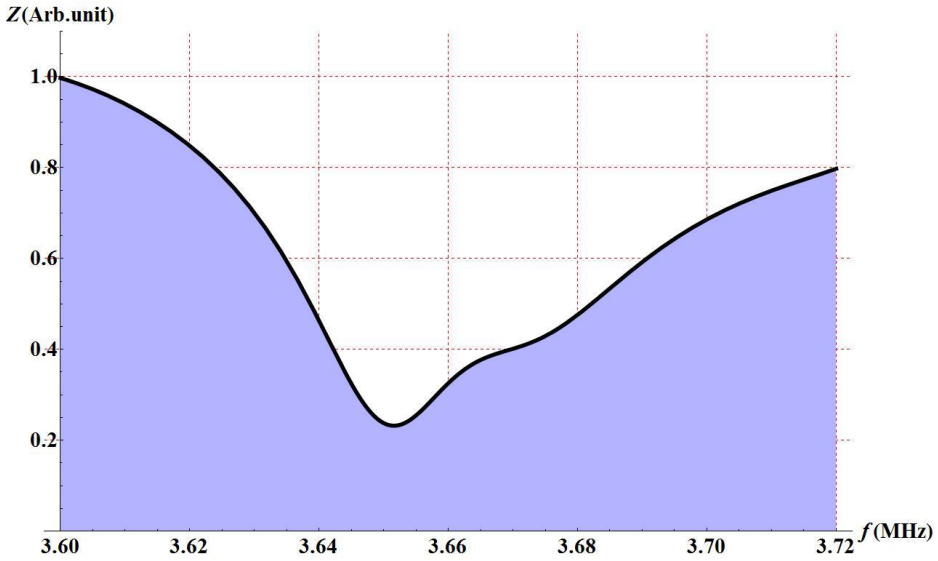

Figure 4-7 (b)

Figure 4-7. Theoretical plot of the acousto-electric impedance of FPS (Z/Z_0) vs. frequency in (a) the first ABZ and (b) the second ABZ for MD3B-NC sample. The two minima in both Figures are due to two displacement components in the corresponding transition zones. The normalization factor Z_0 in the first ABZ is 45-KOhms and in the second ABZ is 62-KOhms.

4.3 Computations of the variance of important FPS-parameters

In piezoelectric materials, there is a strong coupling between electrical and mechanical fields. Consequently, mechanical, electrical and piezoelectric components of energy losses should be included in the characterization. The acousto-electric impedance is sensitive to the change of the main parameters, such as the electromechanical coupling coefficient K, the mechanical quality factor Q, and the phase velocity of the acoustic wave. The minimum value of the impedance does exist within the transition zone, which is about 5070KHz in the frequency range. This section, computationally, discusses the effect of varying the parameters of FPS. Because the transition zone is a small frequency region, and one would like to study the influence within that zone, the change in the parameters is about 1% of the typical values of those parameters. In the following calculations, the parameters are taken for the MD3B-NC sample. The Figures below show the computed acousto-electric impedance in arbitrary unit. The normalization impedance Z_0 is 45-KOhm in the first ABZ and 62-KOhm in the second ABZ.

4.3.1 The variation of the electromechanical coupling coefficient (K)

The electro mechanical coupling coefficient is a numerical measure of conversion efficiency between electrical and acoustic energy in piezoelectric media and is mathematically given by $K^2 = \frac{e^2}{c\varepsilon}$. For the MD3B-NC sample, the value of the electromechanical coupling coefficient is less than 0.31 for all components in the first and second ABZ. Figures (4-8-a) and (8-9-a) numerically show the effect of changing K through increasing it by 1% of K_0 in the first and second ABZ, respectively. Figures (4-8-b) and (4-9-b) numerically show the effect of changing K through reducing it by 1% in the first and second ABZ, respectively.

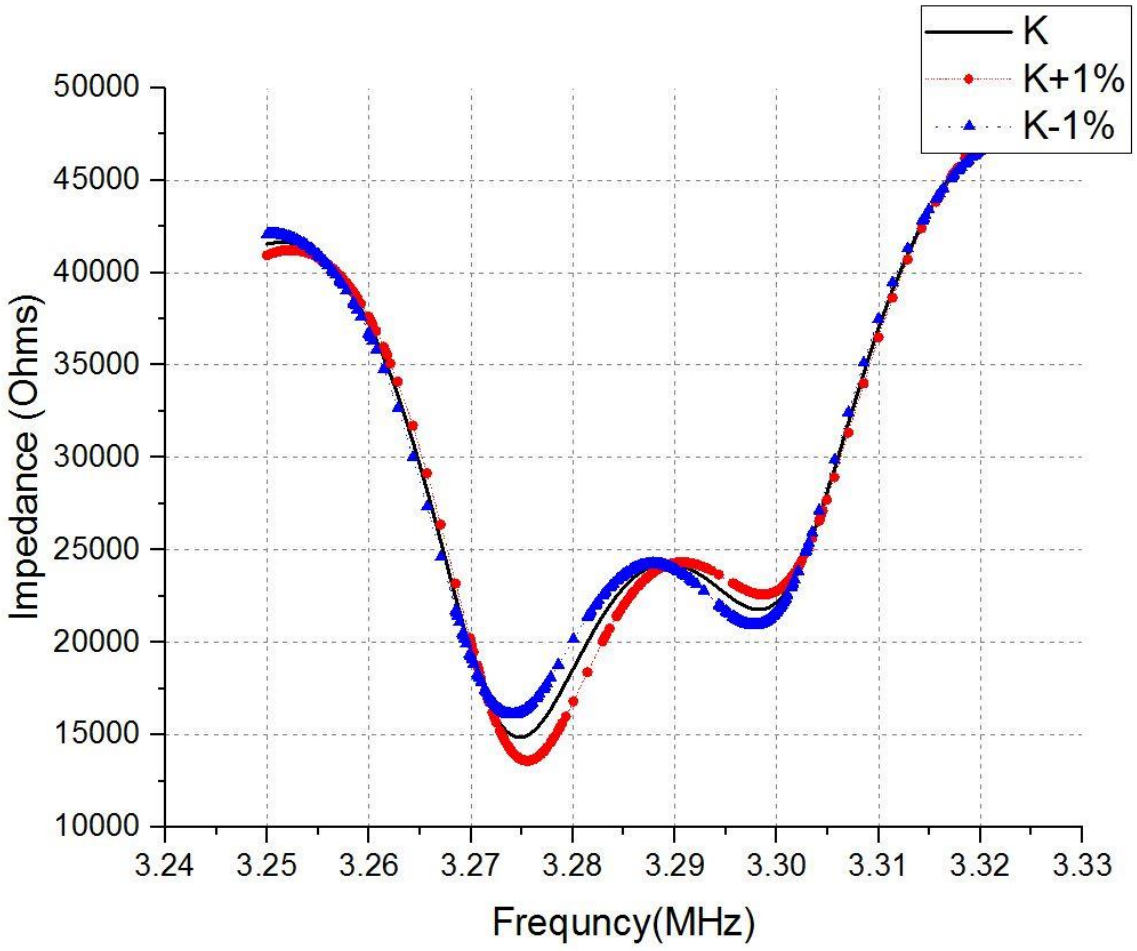

Figure 4-8. The variation of the electro mechanical coupling coefficient by ±1% in the first ABZ is computed for MD3B-NC sample.

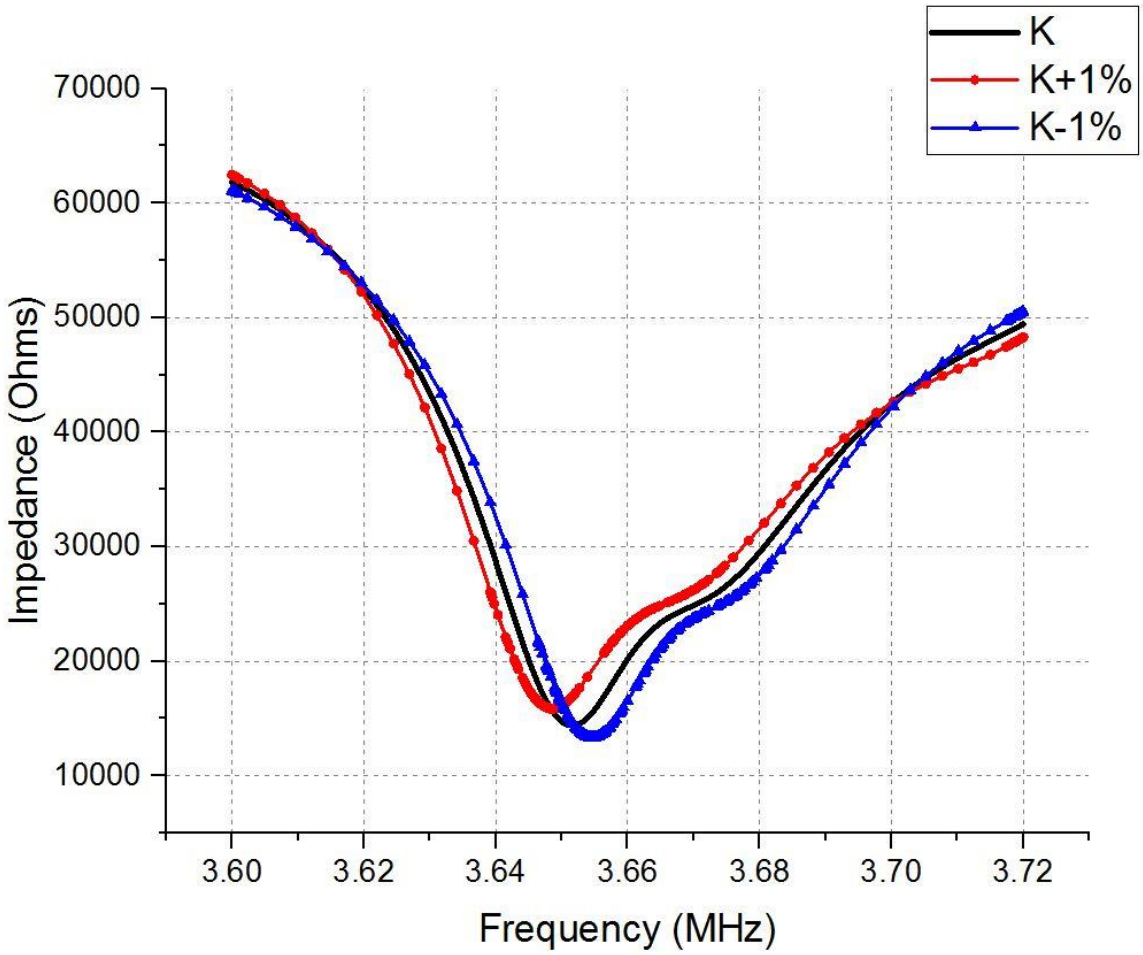

Figure 4-9.The variation of the electro mechanical coupling coefficient by ±1% in the second ABZ is computed for MD3B-NC sample.

The electromechanical coupling coefficient K is included in the $\sin\left(\frac{kNd}{\sqrt{1\pm K^2}}\right)$ term of the Equation (3-28). In the first ABZ, the following analysis can be made according to the calculations: increasing K by 1% mainly affects the Z- component in which the magnitude of *Z(f)*-minimum is reduced with opposite effect on the X- component. In the second ABZ, the effect is vice versa from the analysis of the first zone due to the negative sign in the square root $\sqrt{1\pm K^2}$. Therefore, increasing K by 1% increases the magnitude of *Z(f)*-minimum for both branches. In addition to that, there is a negligibly small frequency shift of about 20 KHz.

4.3.2 The variation of the mechanical quality factor (Q)

The quality factor (Q) compares the time constant for decay of a resonating system's amplitude to its resonance period. It is generally defined as the ratio of the stored energy to the energy dissipated per cycle. For the MD3B-NC sample, the typical value of the mechanical quality factor is Q_0=105 on average. Figures (4-10-a) and (4-11-a) numerically show the effect of changing Q via increasing it by 1% of Q_0 in the first and second ABZ respectively. Figures (4-10-b) and (4-11-b) numerically show the effect of changing Q via reducing it by 1% in the first and second ABZ, respectively.

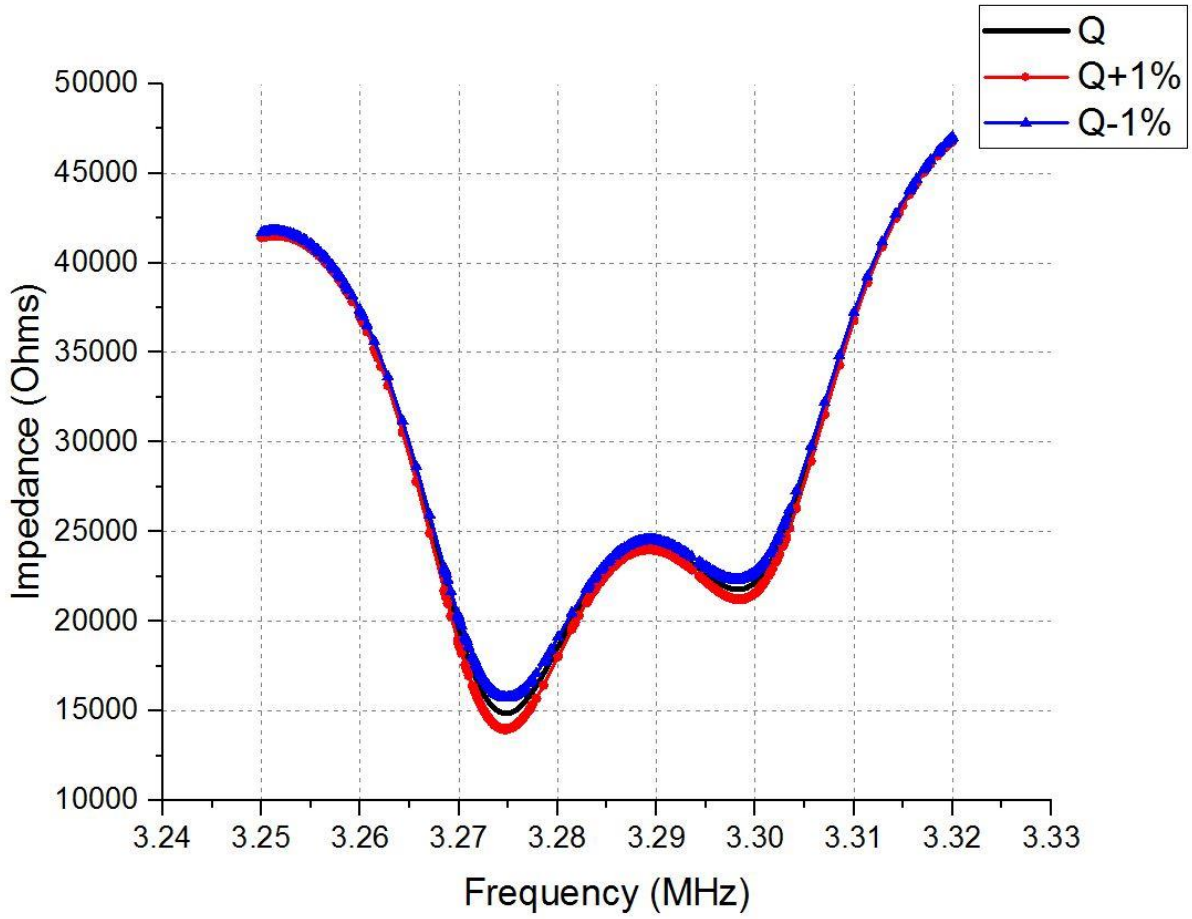

Figure 4-10. The variation of the mechanical quality factor by ±1% in the first ABZ is computed for MD3B-NC sample.

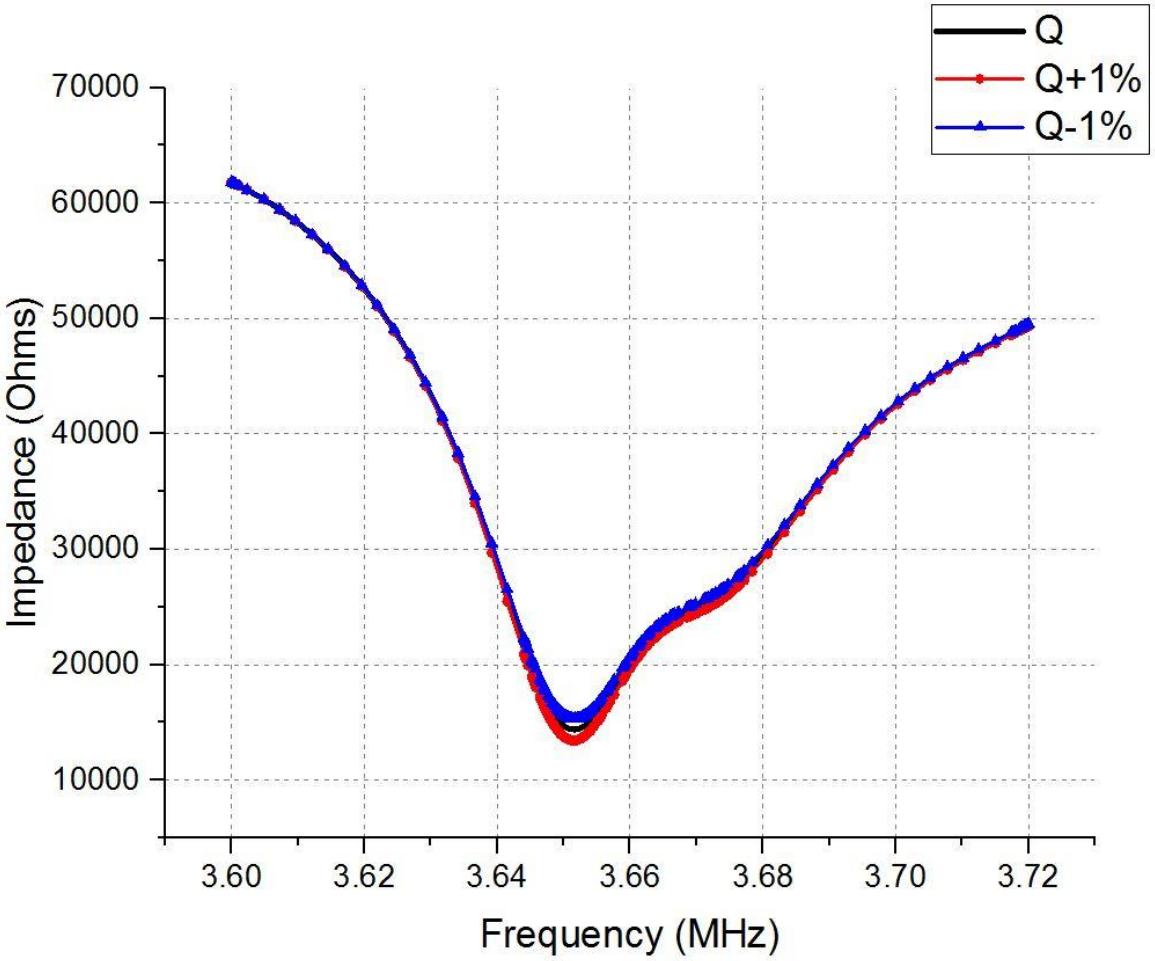

Figure 4-11 (b)

Figure 4-11. The variation of the mechanical quality factor by ±1% in the second ABZ is computed for MD3B-NC sample.

Changing Q is responsible for changing magnitude of the impedance in the transition zones. There is no change or shift in the frequency. Mainly, increasing Q by 1% reduces the magnitude of Z in both zones, and decreasing Q by 1% increases the magnitude of Z.

4.3.3 The variation of the phase velocity (V)

The ultrasound speeds in the frequency range under consideration, 3-4MHz, are calculated as $V_1=2d.F_1$ for m1 mode, and $V_2=2dF_2$ for m2 mode. Thereafter the phase velocities of the X- component are calculated in the transition zone as follow: $V_{1X}=2dF_{1X}$ in the first ABZ and $V_{2X}=2dF_{2X}$ in the second ABZ. Similarly the phase velocities of Z- component is $V_{1Z}=2dF_{1Z}$ in the first ABZ and $V_{2Z}=2dF_{2Z}$ in the second ABZ. The frequency temperature coefficient for Z minimum is dependent on the phase velocity of the acoustic mode of FPS structure. As mentioned in chapter 1, the phase velocity is a function of the elastic constant of the materials and as such a function of temperature. In $LiNbO_3$ the temperature coefficient for a plate resonator is $T \cdot s = 1.66 \times 10^{-4} / C^0$. Thus, if the velocity dependence on temperature is added to the code, then it is used in sensors applications. Numerically, this section studies the influence of varying the phase velocities by $\pm$1% which will vary the temperature coefficient. This change is taken into account by the Equation (3.28), in which $\pm 1\%$ of the typical values of V_{1X}, V_{2X}, V_{1Z}, and V_{2Z} is applied.

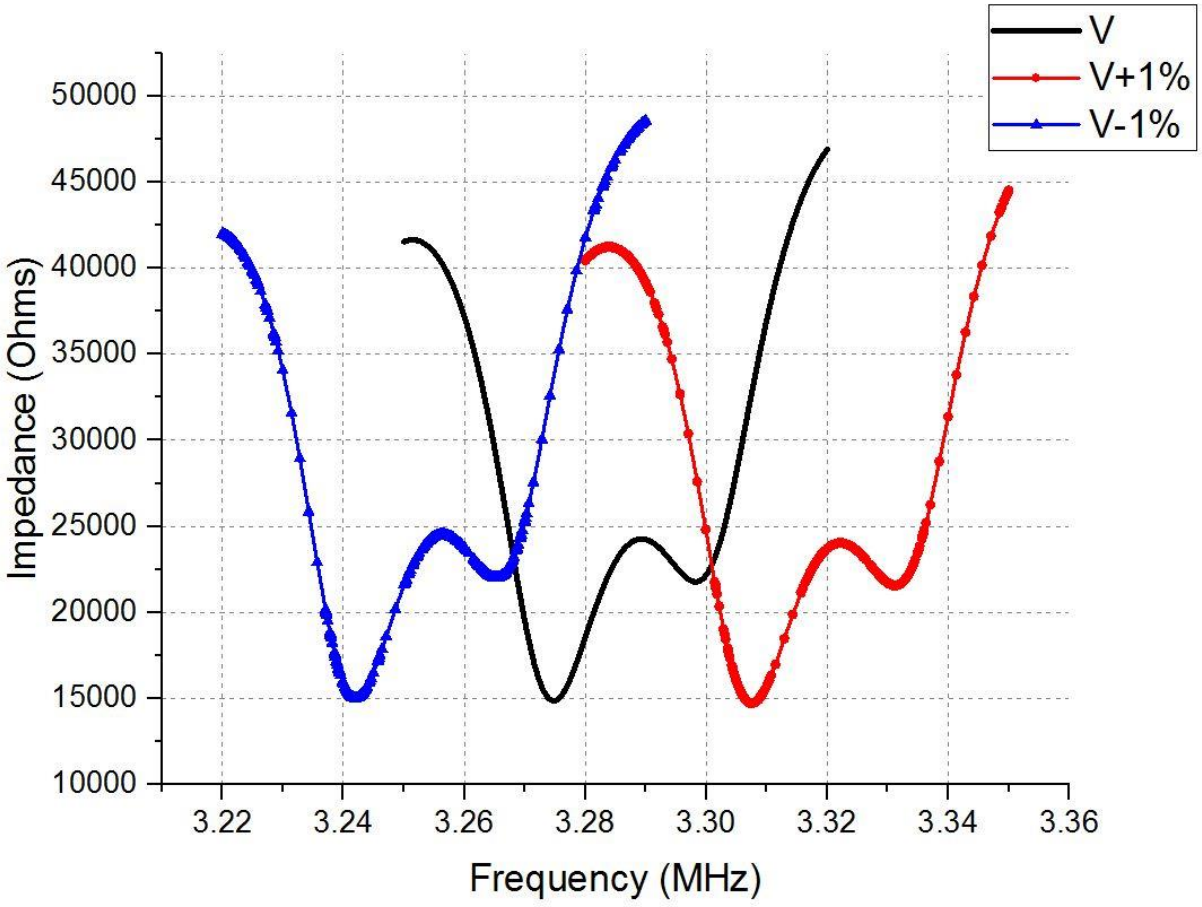

Figure 4-12. The variation of the phase velocity by ±1% in the first ABZ is computed for MD3B-NC sample.

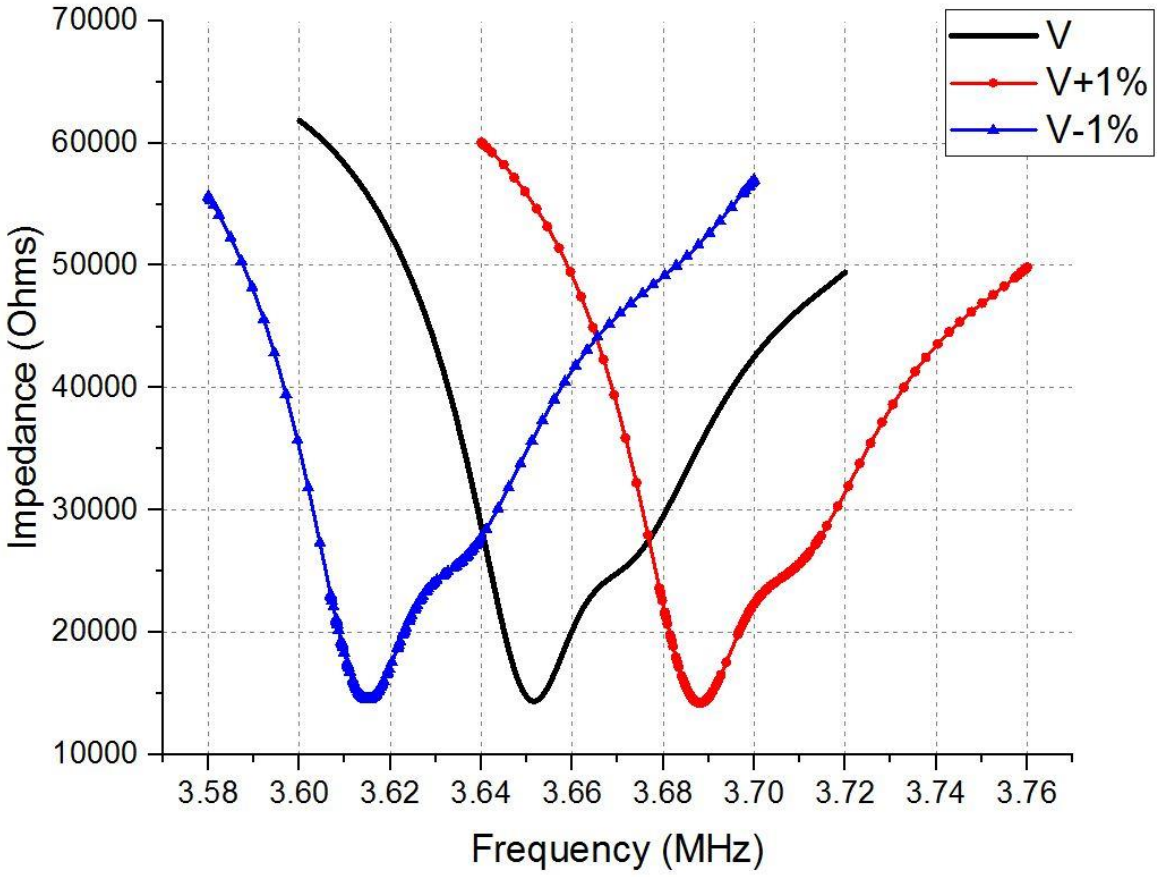

Figure 4-13. The variation of the phase velocity by ±1% in the second ABZ is computed for MD3B-NC sample.

Figures (4.12) and (4.13) show the influence of 1% changing of phase velocity on the acousto-electric impedance. One can conclude that the magnitude of the impedance is not particularly affected. The main influence is the frequency shift in the impedance minima. This shift is approximately 3.5% of the frequency range under consideration.

According to Figures 4-7 through 4-13, one can make the following conclusions:

1- The variation of 1% of the mechanical quality factor affected the magnitude of the impedance only.
2- The electromechanical coupling coefficient variations produces more complicated effects than changes in V or Q, because changing K by 1% leads to changing the magnitude of Z and produces a frequency shift of minima in *Z(f).*
3- In all over, this computing analysis prove that the developed Mathematica- Codes work stable, that is correctly and coincide with the theoretical expectations.
4- It is important to note that if the changes in K, Q, and V are bigger than a few percents, than the computed model *Z(f)* is totally disagree with experiment data. The reason of this section is to show that computer model is very sensitive to all practical characteristics of FPS. Consequently, we may consider FPS parameters as trustable for computation coinciding with experiment.
5- Changing the phase velocity by 1% created a frequency shift of the impedance minima in the first and second ABZ. Correspondingly, temperature coefficients will be changed. If the velocity dependence on temperature or Gamma radiation is applied to the code, then it is used for sensors applications. This shift in frequency is about 30 KHz in both zones.

4.4 The experimental investigations of acousto-electric impedance of MD3B-NC sample

The acousto-electric impedance as a function of frequency from FPS is calculated by the Equation (4.1), (4.2) along with Equations (3.28)-(3.30) for strongly coupled A_X and A_Z displacements. It also numerically modeled in the first and second ABZ. The MD3B-NC sample is used to measure Z in the frequency range under consideration. The sample structure is explained in detail in section 2.2.2. This sample possesses the displacement components effect in the first and second ABZ as shown in Figures 4-5 and 4-6, experimental data prove it as presented in Figures 4-14 through 4-17. The theoretical calculations of *Z(f)* are made in this section using the same experimental frequency range for the sake of comparison. The non-linear fit is used with the experimental data to report the frequency values corresponding to the minima in *Z(f)* of X- and Z- displacement components. The electrical characterization of the fabricated sample-MD3B-NC is performed with two experimental methods. The experimental methods are explained in section 2.3. The experiments were done at room temperature. The experimental results of investigating *Z(f)* using the VVM along with a FG and the digital oscilloscope along with a FG are both presented in Figures 4-15 and 4-17 for the first and second ABZ, respectively.

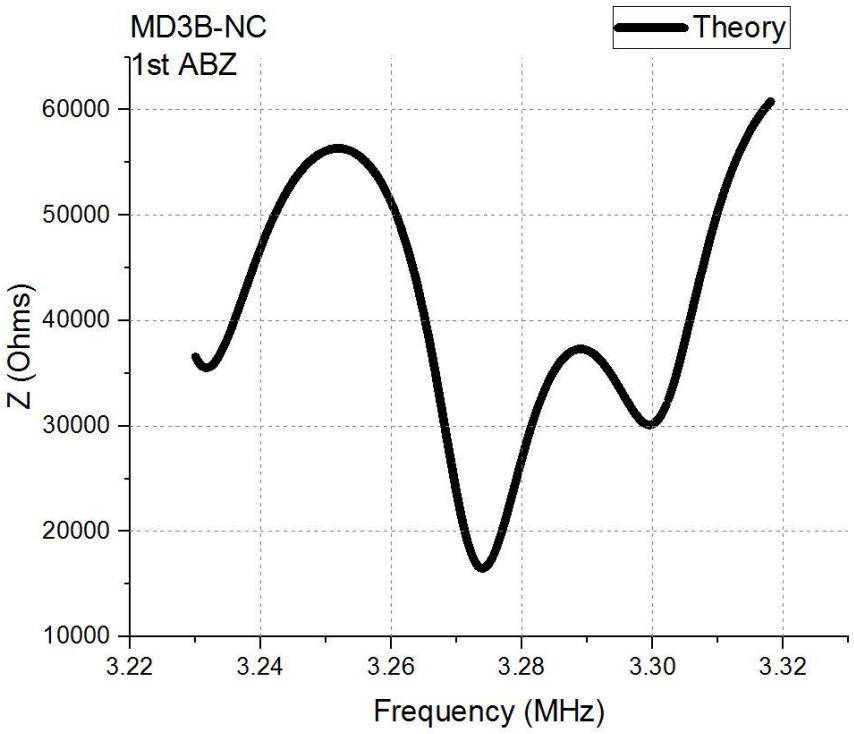

Figure 4-14. The acousto-electric impedance vs. frequency in the first transition zone is calculated for the MD3B-NC sample. Equations (4.1and 4.2) and the limiting frequencies are used in this calculation. The two components of the acoustic mode are shown by two peaks.

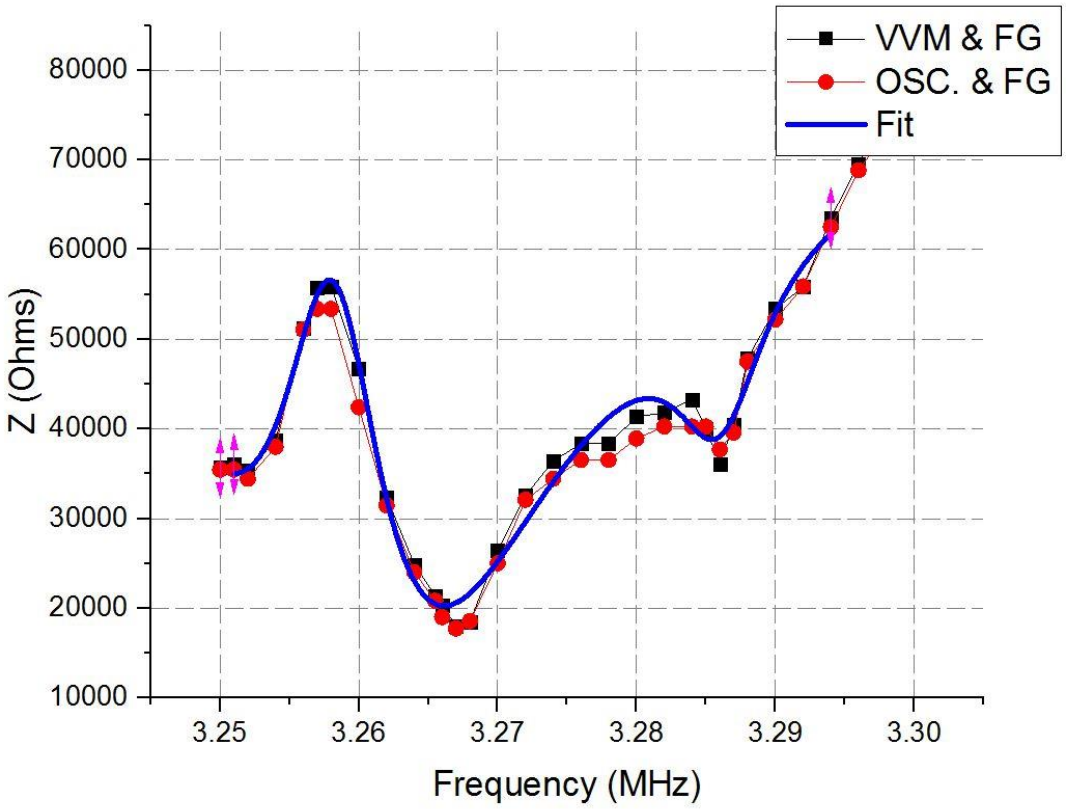

Figure 4-15. The acousto-electric impedance vs. frequency in the first transition zone is measured by two methods. The Z- component is observed at frequency 3.26±0.01MHz, and the X- component is observed at 3.28±0.01MHz as shown by the non-linear fit of the experimental data.

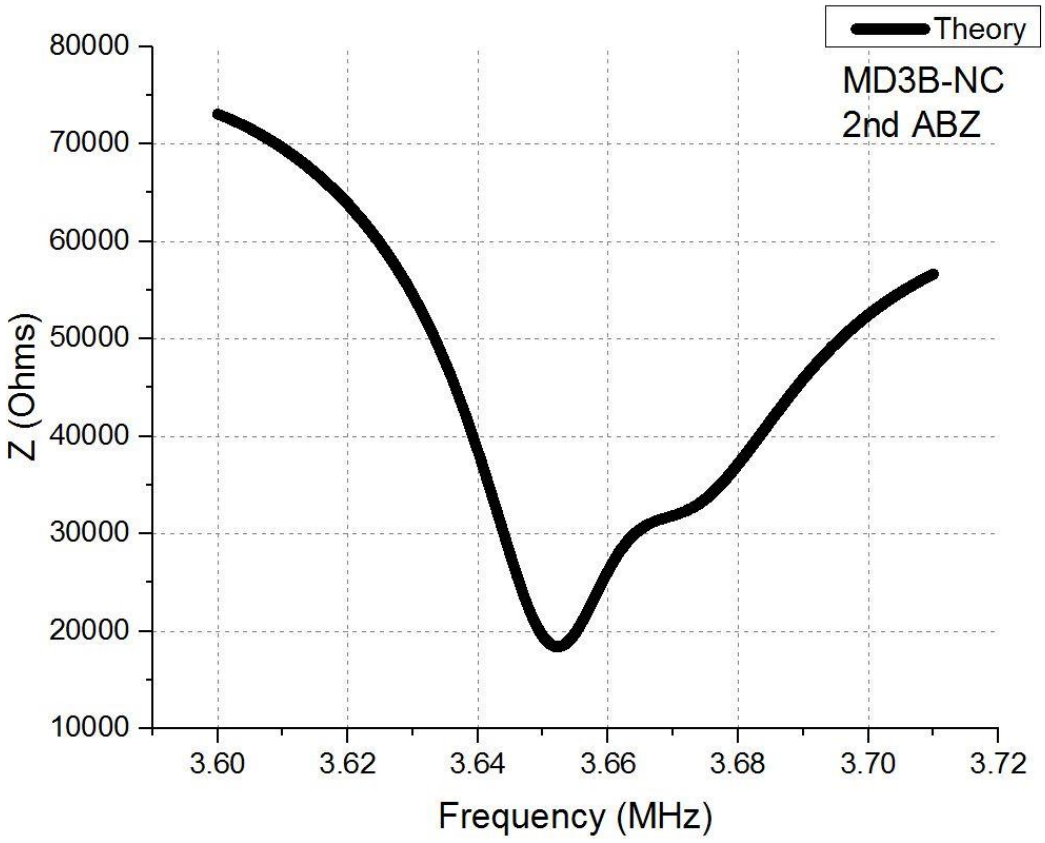

Figure 4-16. The acousto-electric impedance vs. frequency in the second transition zone is calculated for the MD3B-NC sample. Equations (4.1 and 4.2) and the limiting frequencies are used in this calculation. The Z- component is shown by the first peak and the X- component is shown by a peak shoulder.

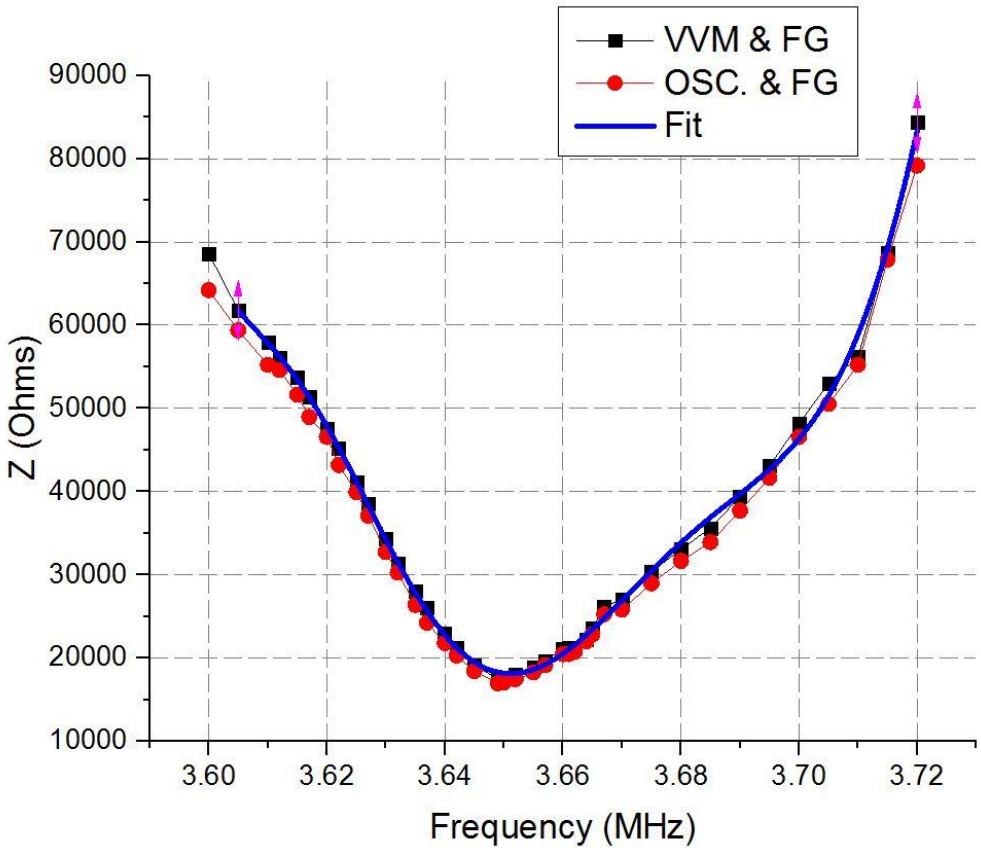

Figure 4-17. The acousto-electric impedance vs. frequency in the second transition zone is measured by two methods. The Z- component is observed at frequency 3.65±0.01MHz, and the X- component is observed at 3.67±0.01MHz as shown by the non-linear fit of the experimental data.

The acousto-electric impedance as a function of frequency is presented in Figures 4-14 through 4-17. Non-linear fit is used to fit the experimental data, which provides us with information about the limiting frequencies. Both experimental methods show two peaks corresponding to the X- and Z- displacement components. The VVM & FG method gives the following limiting frequencies: F_{1Z}=3.267MHz, F_{1X}=3.286 MHz in the first ABZ and F_{2Z}=3.650MHz, F_{2X}=3.670MHz in the second ABZ. Similarly, using the OSC & FG method, the following limiting frequencies of X- and Z- component: F_{1X}=3.286 MHz, F_{1Z}= 3.267 MHz in the first ABZ, and F_{2X}=3.668 MHz, F_{2Z}=3.650 MHz in the second ABZ. However, these values are slightly different from the following theoretical limiting frequencies: F_{1X}=3.297 MHz, F_{1Z}=3.276 MHz in the first ABZ, F_{2X}=3.673 MHz, F_{2Z}= 3.652 MHz in the second ABZ. The uncertainty of the measurements taken by the oscilloscope and the VVM are less than the size of the experimental points

4.5 The phase shift due to FPS

Impedance $Z(\omega) = Z' + iZ''$ is a vector quantity and maybe plotted in the plane with either rectangular or polar coordinates. The two rectangular coordinate values are clearly the real and imaginary parts of the impedance, as shown by Equations (4.3) and (4.4), respectively.

$$\mathrm{Re}(Z) = Z' = |Z|\mathrm{Cos}\theta, \tag{4.3}$$

$$\mathrm{Im}(Z) = Z'' = |Z|\mathrm{Sin}\theta, \tag{4.4}$$

with the phase angle θ and the modulus $|Z|$, given by Equations (4.5) and (4.6), respectively.

$$\theta = \tan^{-1}\left(\frac{Z''}{Z'}\right), \tag{4.5}$$

$$|Z| = \sqrt{(Z')^2 + (Z'')^2}. \tag{4.6}$$

In polar form, Z may now be written as $Z(\omega) = |Z|e^{i\theta}$, which may be converted to rectangular form through the use of the Euler relation $\exp^{i\theta} = Cos(\theta) + iSin(\theta)$. Impedance is by definition a complex quantity and is only real when $\theta = 0$ and thus $Z(\omega) = Z'(\omega)$, that is, for purely resistive behavior. In this case, the impedance is completely frequency-independent.

The phase shift of FPS can be measured by applying AC voltage using a FG to one electrode of the sample and simultaneously measuring the current response from the other electrode. The current response will be of a different phase than the applied voltage and will lag or lead the applied voltage signal depending on whether a measured quantity is capacitive or inductive, respectively. The current response of a pure capacitor will lag the applied voltage in phase by 90^0 while a pure inductor will lead the applied voltage in phase by 90^0.

The phase shift of FPS is numerically modeled using Mathematica software. This software is able to provide the user with the imaginary and real parts of complex expressions.

This is applied to Equations 4.1-4.6 along with Equation 3.28 to model the phase shift of FPS in the first and second ABZ. The computations are as shown in Figures 4-18 and 4-20, for first and second ABZ, respectively. Figures 4-19 and 4-21 present the impedance phase shift of FPS measured using VVM & FG and OSC. & FG methods in the first and second ABZ, respectively.

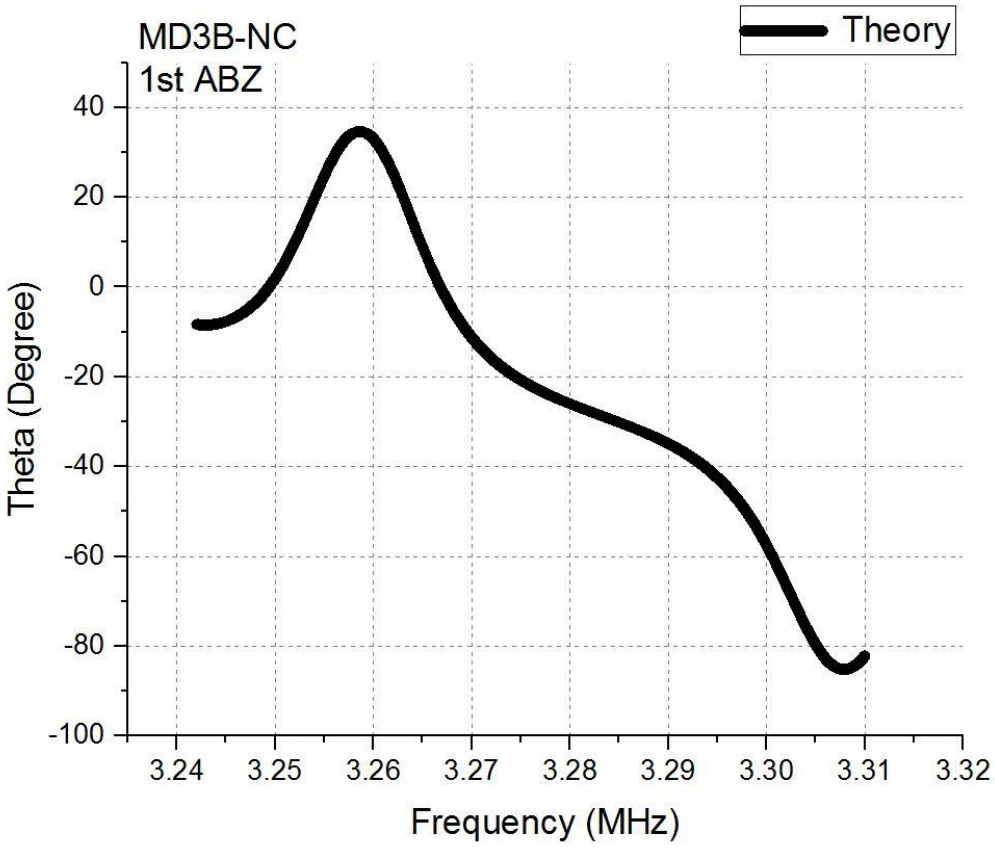

Figure 4-18. The phase-shift of FPS (Degree) vs. frequency (MHz) in the first transition zone is calculated for MD3B-NC sample. Equations (3.28, 4.1- 4.4) along with the sample parameters are used in this modeling. The theoretical phase shift is about 120^0 in the first ABZ.

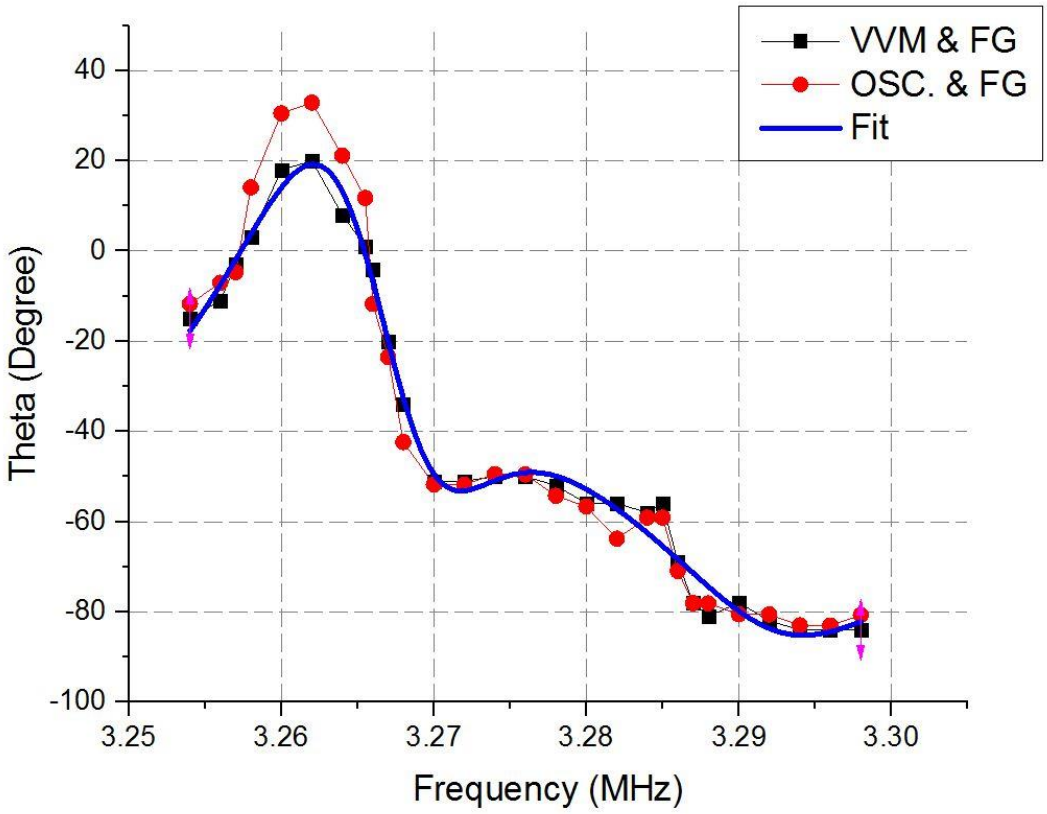

Figure 4-19. The impedance phase shift (Degree) vs. frequency (MHz) in the first transition zone is measured for MD3B-NC sample. The 'VVM & FG' and 'OSC. & FG' methods are used in this measurement. The phase shift is about 105^0.

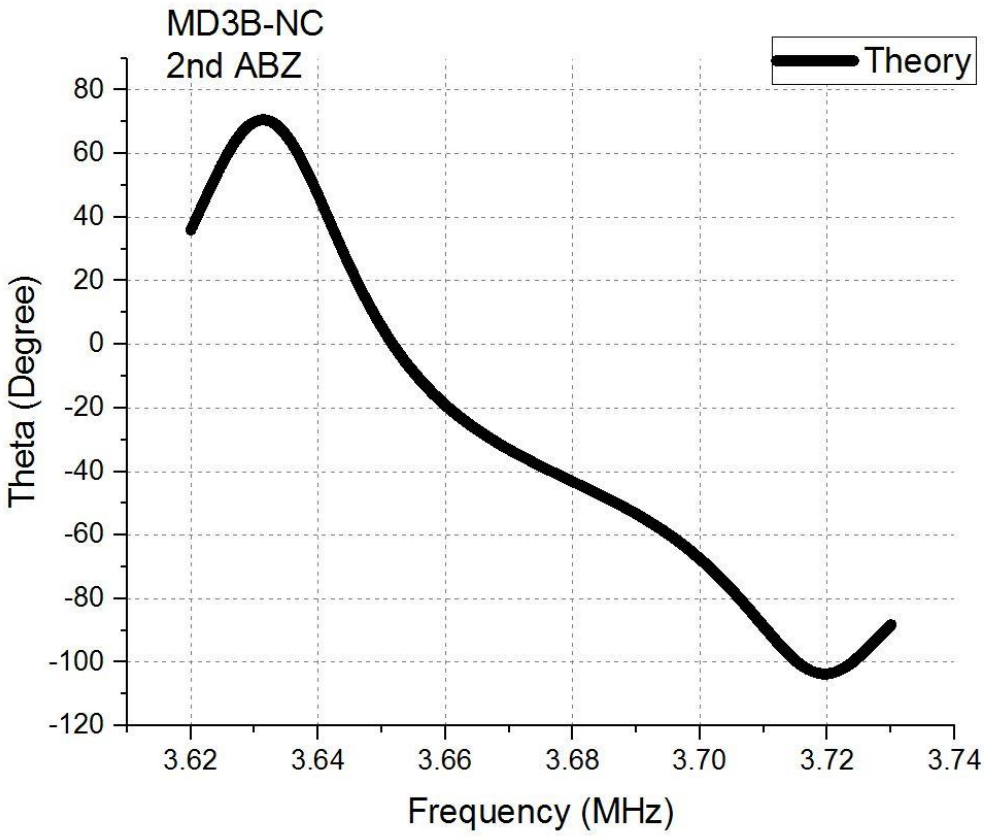

Figure 4-20. The impedance phase-shift vs. frequency in the second transition zone is calculated for MD3B-NC sample. Equations (3.28, 4.1- 4.4) and sample parameters are used in this modeling. The theoretical phase shift is about 175^0 in the first ABZ.

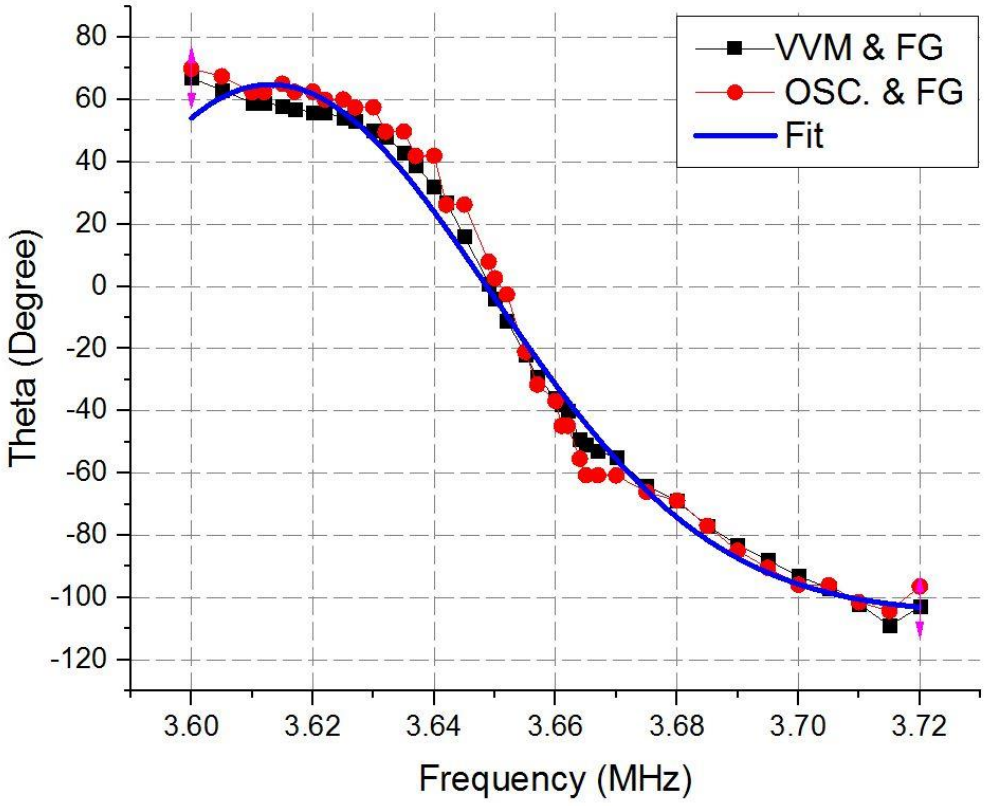

Figure 4-21. The impedance phase-shift (Degree) vs. frequency (MHz) in the second transition zone is measured for MD3B-NC sample. The 'VVM & FG' and 'OSC. & FG' methods are used in this measurement. The phase shift is about 170^0.

The phase shift of FPS is considered theoretically and verified experimentally. Theoretically, the total phase shift of FPS is about 120^0 and 175^0 in the first and second ABZ, respectively. The method of using VVM & FG shows close measurements to the proposed theory, the total phase shift is 105^0 and 170^0 in the first and second ABZ, respectively. The second method OSC. & FG reveals the total phase shift of about 118^0 and 178^0 in the first and second ABZ, respectively. There is a small difference in the frequency range between theory and experiments. The same parameters used in the impedance modeling are used for the phase modeling.

The experimental measurements of phase shift reveal the existence of two acoustical components of the A_0 mode in the transition zones. In the first ABZ, the existence Z-component is shown by a peak in the phase diagram in which the curve cross the zero scale with positive slope and then with negative slope. This is shown in Figure 4-22 by two green vertical lines to the left. That phase shift peak corresponds to minimum in the acousto-electric impedance, which is proportional to maximum acoustical amplitude. Consequently, the existence of X-component is shown by local peak in the phase-shift diagram, in which the slope is slightly changing from positive to negative at frequency close to 3.286MHz. This peak corresponds to a local minimum in the acousto-electric impedance, as shown in Figure 4-22. In the second ABZ the phase-shift experimental curve crosses the zero with negative slope at one point, as shown in Figure 4-23 by a solid green line to the left. At that frequency the impedance has a minimum. Moreover, there is a small change in the phase-slope sign close to the frequency 3.68MHz. This small change of sign is signified by that small shoulder in the impedance measurements of FPS, as presented in Figure 4-23.

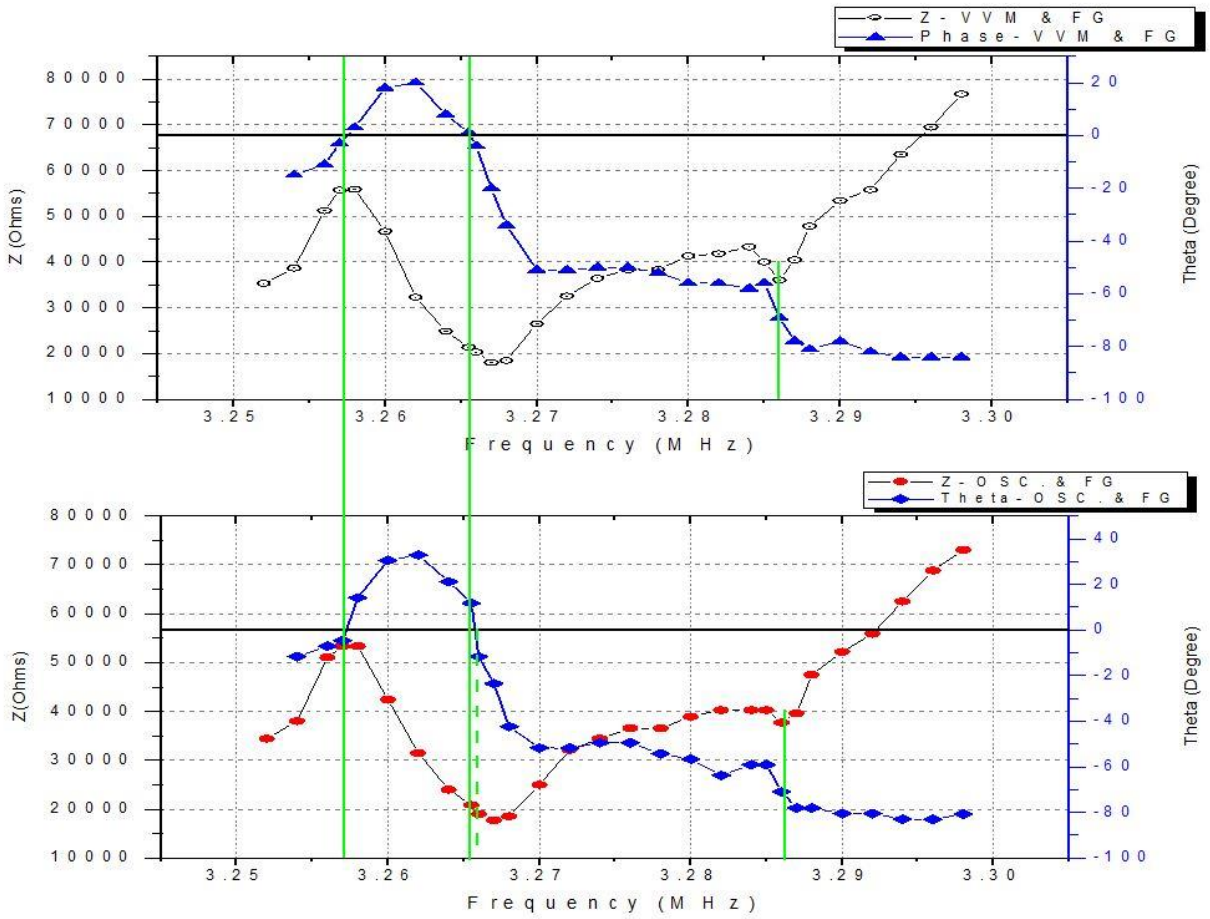

Figure 4-22. The acousto-electric impedance (Z) and the impedance phase-shift (Theta) vs. frequency for the MD3B-NC sample. The measurements are taken in the first transition zone. The impedance obtained with VVM & FG and the OSC. & FG methods are indicates on the left vertical axes. The phase obtained by the VVM & FG and the OSC. & FG methods are indicates on the right vertical axes. The green lines represent the extreme values of Z corresponding to a sign changing slope of the phase-shift curve. The dashed green line denotes the small difference between the VVM & FG and OSC. & FG methods.

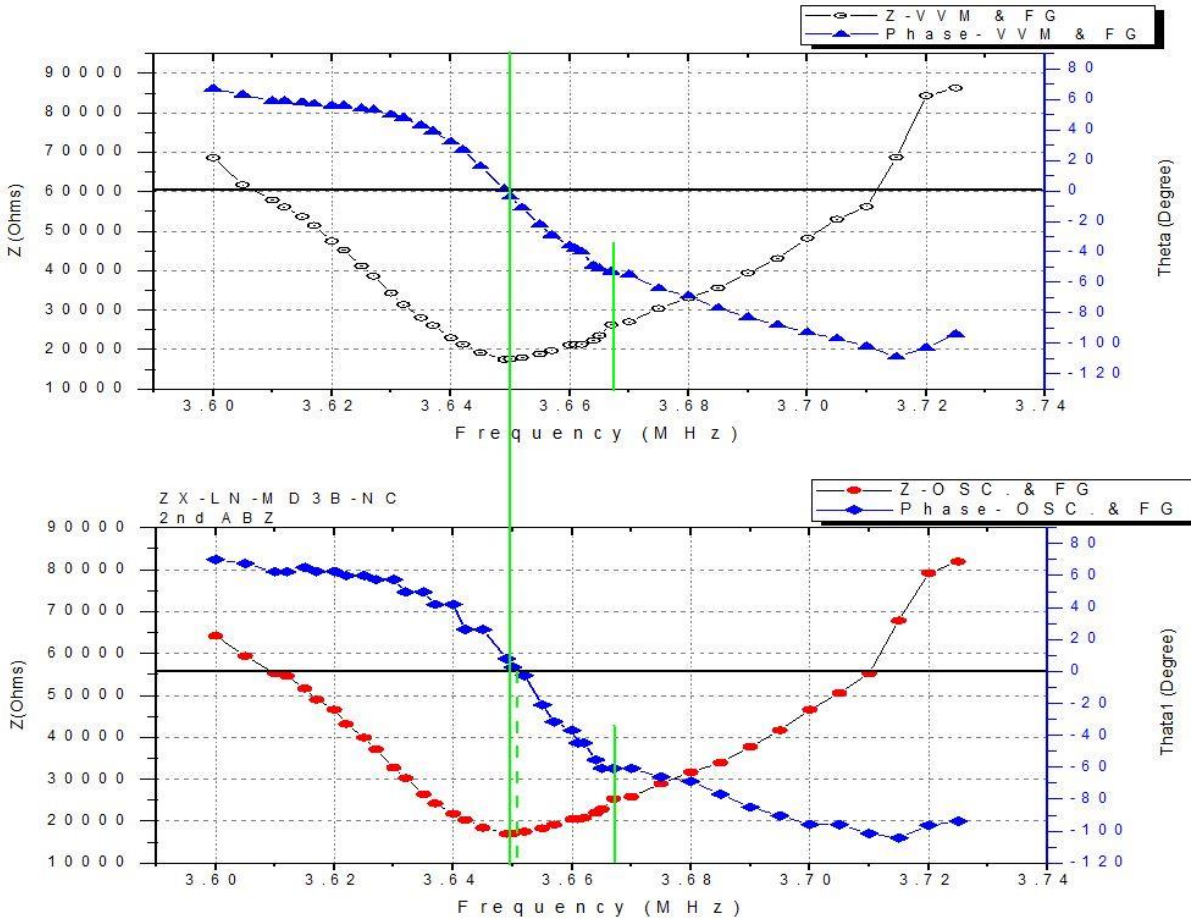

Figure 4-23. The acousto-electric impedance (Z) and the phase-shift (Theta) vs. frequency for the MD3B-NC sample. The measurements are taken in the second transition zone. The impedance obtained with VVM & FG and the OSC. & FG methods are indicates on the left vertical axes. The phase-shift obtained by the VVM & FG and the OSC. & FG methods are indicates on the right vertical axes. The green lines represent the extreme values of Z corresponding to a sign changing slope of phase-shift curve. The dashed green line represents the small difference between the VVM & FG and the OSC. & FG methods.

CHAPTER V CONCLUSIONS

Results including, theoretical, computations, and experimental investigations presented allow to make the following conclusions:

1. The analytical Equation of the acousto-electric impedance $Z(f)$ of ferroelectric phononic superlattice (FPS) is obtained. The impedance $Z(f)$ is a function of frequency f, and FPS characteristics such as number of domain pairs N, domain length d, electromechanical coupling coefficient K, mechanical quality factor, and phase velocity V of plate acoustic waves (PAW) in a crystal.
2. An important physical property of the acousto-electric impedance is its phase shift between applied AC-voltage and AC-current flowing through the ferroelectric phononic superlattice. The phase shift of the acousto-electric impedance is obtained analytically.
3. Computer modeling of the acousto-electric impedance of the ferroelectric phononic superlattice reveals the effect of acoustic stopband. Within the stopband frequencies $Z(f)$ is much higher than at each side frequency. The phase shift is strongly changing near the boundary of the stopband.
4. The number of domains influences the acousto-electric impedance. Theory given by Equation (3.28) and calculations showed in Figures (3-4, 3-5, and 3-6), in which the number of domains are changed from 44 to 28 domain pairs, illustrate that Z can be as small as close to zero. It means that Z can be effectively controlled by N.

5. The comparison with experimental data and computational variation of the parameters of ferroelectric phononic superlattice under study, such as the mechanical quality factor Q, the electromechanical coupling coefficient K and the acoustic phase velocity V, proved the validity of the Mathematica codes that is used to model the acousto-electric impedance and its phase shift of FPS.
6. The frequency limits of the acoustic stopband maybe determined experimentally by measuring the minima in $Z(f)$ dependency. The experimental data taken from FPS based on the periodically poled crystal of lithium niobate prove this consideration. Furthermore, it is proved by computer simulations with the analytical equations obtained in this work.
7. Measurements of the $Z(f)$ dependency reveal the existence of two minima in the $Z(f)$ function. In particular, there are two minima in Figures 4-1 and 4-3. However, the computations by a single acoustic mode with coupled displacements gives only one minimum. This situation implies the possibility of more than one component of an acoustic displacement field contributing into $Z(f)$. In other words, a total acoustic displacement of plate wave may be decoupled into components. The effect of decoupled displacements near a stopband in a phononic crystal is theoretically shown for LiNbO3-superlattice in reference [73]. The two displacement components, those in plane of propagation and those normal to it become decoupled near the stopband.
8. The existence of displacement components in the transition zone is proved experimentally by the data from the MD3B-NC sample as shown in Figures (4-15 and 4-17). The first and second displacement components are reflected by the two minima in the $Z(f)$ for each acoustic Brillouin zone. This refers to the two orthogonal displacement components such as A_X and A_Z.

9. The phase shift of ferroelectric phononic superlattice FPS is experimentally measured with the MD3B-NC sample. Figures (4-21 and 4-19) show the phase plot changing its slope at the frequencies corresponding to the limiting frequencies of X- and Z-components. The frequencies are F_{X1}, F_{Z1}, F_{Z2}, and F_{X2}. This result shows the decoupling of the acoustic mode by Ax and Az displacements near the boundaries of the stopband in the frequency domain. In the wave-vector domain, the decoupling takes place near the boundary of the acoustic Brillouin zone.
10. Both measurements phase and the acousto-electric impedance prove the effect of the decoupling of the total acoustic displacement by two components. The phase diagram with changing slope-sign corresponds to the mode displacement, and that is supported by a minimum in the impedance diagram. This is shown in Figures 4-22 and 4-23 in the first and second ABZ, respectively.
11. The maximum efficiency of a transformation from electric in to acoustic energy and vice versa will be near the acousto-electric resonances at frequencies F_1 and F_2. The acoustic amplitude is inversely proportional to the acousto-electric impedance. Thus the minima's in Figures (4-1, 4-2, 4-3 and 4-4) reflects the maximum efficiency of acousto-electric transformation of energy.
12. The analytical equations can be used for developing new acousto-electric applications such as ultrasonic sensors, ultrasonic transducers and actuators usually found in MEMS. One can use the equations and Mathematica codes for any FPS, since experiments proved a validity of the equations and codes. For a particular FPS, it is necessary to substitute into the equations and codes the characteristics of the FPS, such as the number of

domains N, the electromechanical coupling coefficient K, the mechanical quality factor Q, the domain length d, and the plate acoustic phase velocity V.

BIBLIOGRAPHY

[1] I. A. Victorov, “RayIeigh and Lamb Waves” (Plenum, New York, 1967).

[2] S. W. Wenzel and R. M. White, "*A multisensory employing an ultrasonic Lamb-wave oscillator*” IEEE Trans. Electron. Devices, vol. 35, no. 6, pp. 735-743, (1988).

[3] B. J. Costello, B. A. Martin, and R. M. White, Proc. IEEE Ultrason. Symp, 977 (1989).

[4] H. Wohltjen, in Digest of Technical Papers, 4th International Conference on Solid-State Sensors and Actuators (IEE, Japan, 1987), pp. 471-477.

[5] D. Feng, N. B. Ming, J. F. Hong, Y. S. Yang, J. S. Zhu, Z. Yang, and Y. N. Wang, Appl. Phys. Lett. 37, 607 (1980).

[6] N. B. Ming, J. F. Hong, and D. Feng, J. Mater. Sci. 17, 1663 (1982).

[7] A. Feisst and P. Koidl, Appl. Phys. Lett. 47, 1125 (1985).

[8] V. V. Antipov *et al.*, Sov. Phys. Crystallogr. 30, 428 (1985).

[9] Y. Y. Zhu, N. B. Ming, J. Appl. Phys. 72,904 (1991).

[10] Y. Y. Zhu, S. N. Zhu, Y. Q. Qing, and N. B. Ming, ibid. 79,2221(1996).

[11] Y. Y. Zhu, N. B. Ming, J. Phys. D 29, 185 (1996).

[12] M. A. Breazeale, I. V. Ostrovskii, and M. S. McPherson, J. Appl. Phys. 96, 2990 (2004).

[13] Yanping Fan, Xiaojun Ji, Xianping Liu, Ping Cai,” *The nonlinear analysis of elastic wave of piezoelectric crystal plate with perturbation method*” Wave Motion, July 2014, vol.51, no.5, pp. 798-803.

[14] Caliendo, Cinzia, Castro, Fabio Lo,” *Quasi-Linear Polarized Modes in Y-Rotated Piezoelectric $GaPO_4$ Plates*”. *Crystals (2073-4352).* Sep2014, Vol. 4 Issue 3, p228-240.

[15] Cho, Yasuo*.” Nano-domains and related phenomena in congruent lithium tantalate single crystals studied by scanning nonlinear dielectric microscopy.” IEEE Transactions on Ultrasonics Ferroelectrics & Frequency Control* , Aug2014, Vol. 61 Issue 8, p1368-1378,

[16] Motohiro Ogino, Yuji Noguchi, Yuuki Kitanaka, Masaru Miyayama, Chikako Moriyoshi, Yoshihiro Kuroiwa.” *Polarization Rotation and Monoclinic Distortion in Ferroelectric $(Bi_{0.5}Na_{0.5})TiO_3$--$BaTiO_3$ Single Crystals under Electric Fields.*” *Crystals (2073-4352).* Sep2014, Vol. 4 Issue 3, p273-295.

[17] Dejin Huang, Jiashi Yang,” *On the propagation of long thickness-stretch waves in piezoelectric plates*” Ultrasonics, July 2014, vol.54, no.5, pp. 1277-80.

[18] Chengchao Jin, Feifei Wang, Chung Ming Leung, Qirong Yao, Yanxue Tang, Tao Wang, Wangzhou Shi," *Enhanced ferroelectric and piezoelectric response in Mn-doped $Bi_{0.5}Na_{0.5}TiO_3$-$BaTiO_3$ lead-free film by pulsed laser deposition*" Applied Surface Science, 15 Oct. 2013, vol.283, pp. 348-51

[19] Waegner, M. Schro¨der, M. Suchaneck, G. Sturm, H. Weimann, C. Eng, L.M. Gerlach, G.," *Enhanced Piezoelectric Response in Nano-patterned Lead Zirconate Titanate Thin Films*" Japanese Journal of Applied Physics, Nov. 2012, vol.51, no.11, pt.2, 11PG04

[20] M. J. Vellekoop, "*Acoustic wave sensors and their technology*," Ultrasonics, vol. 36, no. 1-5, pp. 7-14, (1998).

[21] D. S. Ballantine, R.M. White, S. J. Martin, A. J. Ricco, E. T. Zellers, G. C. Frye, and H. Wohltjen, Acoustic Wave Sensors. San Diego: Academic Press, ch.3, (1997).

[22] F. Teston, G. Feuillard, L. Tessier and M. Lethiecq, "*Mass sensitivity of acoustic plate mode in liquids*," IEEE Trans. Ultrason., Ferroelect., Freq. Contr., vol. 45, no. 5, pp, 1266 -1272, (1998).

[23] K. Mizutani and K. Toda, "*Analysis of Lamb wave propagation characteristics in rotated Y-cut X-propagation LiNbO3 plates*" Electron. Commun. Japan, vol.69, no.4, pt. 1, pp.47-55, (1986).

[24] E. L. Adler "*Electromechanical coupling to Lamb and Shear horizontal modes in piezoelectric plates*," IEEE Trans. Ultrason., Ferroelect., Freq. Countr., vol. 36, no. 2, pp. 223-231, (1989).

[25] S. G. Joshi and Y. Jin, "*Propagation of ultrasonic Lamb waves in piezoelectric plates*," J. Appl. Phys., vol. 70, no.8, pp. 4113-4120, (1991)

[26] M. A. Hawwa, "*Acoustic/elastic stop-band interaction in waveguides involving two periodicities*," J. Acoust. Soc. Am., 102, 137–142 (1997).

[27] R. C. Yin, S. Y. Yu, C. He, M. H. Lu, and Y. F. Chen, "*Bulk acoustic wave delay line in acoustic superlattice,*" Appl. Phys. Lett. 97, 092905 (2010).

[28] I. V. Ostrovskii, V. A. Klymko, and A. B. Nadtochiy, "*Plate wave stopbands in periodically poled lithium niobate,*" J. Acoust. Soc. Am. 125(4), EL129–EL133 (2009).

[29] S. Benchabane, A. Khelif, J.-Y. Rauch, L. Robert, and V. Laude, "*Evidence for complete surface wave band gap in piezoelectric phononic crystal*," Phys. Rev. E73, 065601 (2006)

[30] I. V. Ostrovskii, and L. Cremaldi, "*Split-mode ultrasonic transducer*," J. Acout. Soc. Am., Vol. 134, No. 2, Pt. 2, (2013)

[31] H.H. Huang, C.T. Sun, G.L. Huang, "*On the negative effective mass density in acoustic metamaterials*" Int J Eng Sci, 47 (2009), pp. 610‑617

[32] P.A. Deymier," *Acoustic metamaterials and phononic crystals*" Springer, New York (2013)

[33] B.A. Auld, "*Acoustic fields and waves in solids,*" John Wiley and Sons, Inc. (1973)

[34] A. I. Beltzer, "*Acoustic of solids*" Springer-Velag Berlin Heidelberg (1988)

[35] Daniel Royer "*Elastic waves in Solids II*" Springer-Verlag Berlin Heidelberg (2000)

[36] J. David N. Cheeke "*Fundamentals and Applications of ultrasonic waves*" CRC Press LLC (2002)

[37] M. E. Lines and A. M. Glass, Principles and Applications of Ferroelectrics and Related Materials (Clarendon, Oxford, 1977).

[38] J. A. Christman. 1999. Piezoelectric Measurements Using An Atomic Force Microscope. PhD thesis, North Carolina State University, Raleigh, NC.

[39] W. J. Merz, Phys. Rev., 95, 690 (1954).

[40] Y. Uesu, S. Kurimura and Y. Yamamoto, Appl. Phys. Lett., 66, 2165 (1995).

[41] S. Zhu and W. Cao, Phys. Rev. Lett., 79, 2558 (1997).

[42] V. M. Fridkin, Ferroelectric Semiconductors (Consultants Bureau, New York, 1980).

[43] I. V. Ostrovskii, A. B. Nadtochiy, V. A. Klymko, "*Velocity dispersion of plate acoustic waves in a multidomain phononic superlattice*," Phys. Rev. B 82, 014302 (2010).

[44] M. Sigalas and E. N. Economou. Band structure of elastic waves in two dimensional systems. Solid State Communications, 86(3):141–143, 1993.

[45] M. S. Kushwaha, P. Halevi, L. Dobrzynski, and B. Djafari-Rouhani. "*Acoustic band structure of periodic elastic composites.*" Physical Review Letters, 71(13):2022, 1993.

[46] Y. Pennec, B. Djafari-Rouhani, J. O. Vasseur, A. Khelif, and P. A. Deymier. "*Tunable filtering and demultiplexing in phononic crystals with hollow cylinders.*" Phys. Rev. E, 69:046608, 2004.

[47] V. Laude, L. Robert, W. Daniau, A. Khelif, and S. Ballandras. Surface acoustic wave trapping in a periodic array of mechanical resonators. Applied Physics Letters, 89(8):083515–3, 2006.

[48] T.-C. Wu, T.-T. Wu, and J.-C. Hsu. "*Waveguiding and frequency selection of lamb waves in a plate with a periodic stubbed surface*". Physical Review B, 79(10):104306, 2009.

[49] T.-T. Wu, W.-S. Wang, J.-H. Sun, J.-C. Hsu, and Y.-Y. Chen. "*Utilization of phononic-crystal reflective*

gratings in a layered surface acoustic wave device". Applied Physics Letters, 94(10):101913, 2009.

[50] X. Zhang, T. Jackson, E. Lafond, P. Deymier, and J. Vasseur. "*Evidence of surface acoustic wave band gaps in the phononic crystals created on thin plates.* "Applied Physics Letters, 88(4):041911–3, 2006.

[51] T.-T. Wu, Z.-G. Huang, and S. Lin. "*Surface and bulk acoustic waves in twodimensional phononic crystal consisting of materials with general anisotropy.*" Phys. Rev. B, 69:094301, 2004.

[52] S. Mohammadi, A. A. Eftekhar, A. Khelif, W. D. Hunt, and A. Adibi. "*Evidence of large high frequency complete phononic band gaps in silicon phononic crystal plates.*" Applied Physics Letters, 92(22):221905,2008.

[53] R. H. Olsson and I. El-Kady." *Microfabricated phononic crystal devices and applications.* "Measurement Science and Technology, 20(1):012002, 2009.

[54] O. Nusierat, L. Cremaldi, and I. Ostrovskii "*Acoustical Transduction in two-dimensional piezoelectric array*" 168th Meeting: Acoustical Society of America, Indianapolis, October 2014

[55] ANSI/IEEE Std 176-1987, IEEE Standard on Piezoelectricity.

[56] J. R. Vig, (2007, Jan.) Quartz crystal resonators and oscillators for frequency control and timing applications - a tutorial.

[57] J. S. Yang, "*The Mechanics of Piezoelectric Structures*. "Singapore: World Scientific, 2006.

[58] J. S. Yang," *An Introduction to the Theory of Piezoelectricity.* "New York: Springer, 2005.

[59] F. Shen and P. Lu, "*Influence of interchannel spacing on the dynamical properties of multichannel quartz crystal microbalance*," IEEE Trans. Ultrason. Ferroelectr. Freq. Control., vol. 51, pp. 249-253, 2004.

[60] E. P. EerNisse, "*Simultaneous thin-film stress and mass-change measurement using quartz resonators,*" J. Appl. Phys., vol. 43, pp. 1330-1337, 1972.

[61] E. J. Lim, M. M. Fejer, and R. L. Byer, Electron. Lett., 25, 174 (1989).

[62] R. L. Byer, J. Nonlin. Opt. Phys. Mater., 6, 549 (1997).

[63] J. G. Gualtieri, J. A. Kosinski, and A. Ballato, IEEE Trans. Ultrason. Ferroelectr. Freq. Control, 41, 53 (1994).

[64] Y. Q. Shi, C. Zhang, H. Zhang, J. aH. Bechtel, L. R. Dalton, B. H. Robinson, and W. H. Steier, Science, 288, 119 (2000).

[65] S. Ganesamoorthy, M. Nakamura, S. Takekawa, S. Kumaragurubaran, K. Terabe, and K. Kitamura, Mater. Sci. Eng. B, 120, 125 (2005).

[66] Sergei V. Kalinin and Dawn A. Bonnell, Phys. Rev. B, 63, 125411 (2001).

[67] O. F. Schirmer, O. Thiemann, and M. Wohlecke, J. Phys. Chem. Solids, 52, 185 (1991).

[68] A. Prokhorov and I. Kuzminov, Physics and Chemistry of Crystalline Lithium Niobate (Hilger, Bristol New York, 1990).

[69] M. Yamada, N. Nada, and K. Watanabe, Appl. Phys. Lett. 62, 435 (1993).

[70] L. E. Myers, R. C. Echardt, M. M. Fejer, and R. L. Byer, J. Opt. Soc. Am. B 12, 2102 (1995).

[71] Y. Q. Lu, Y. Zhu, Y. Chen, S. Zhu, N. Ming, and Y. Feng, Science 284, 1822 (1999).

[72] Victor Klymko, Andriy Nadtochy, and Igor Ostrovskii ”theoretical and experimental study of plate acoustic waves in ZX-cut lithum Niobate”, IEEE Transactions on Ultrasonics, Ferroelectrics, and frequency control, 55,2726-2731(2008)

[73] Younes Achaoui, Abdelkrim Khelif, Sarah Benchabane and Vincent Laude,”*Polarization state and level repulsion in two-dimensional phononic crystals and waveguides in the presence of material anisotropy*” *J. Phys. D: Appl. Phys.* 43 185401 (2010)

APPENDIX

Below are the MATHEMATICA codes of modeling the acousto-electric impedance and its phase shift in the first and second ABZ. The parameters are included.

```
ClearAll
Element[m,Reals]; Element[d,Reals]; Element[K,Reals]; Element[n,Reals];
Element[K1,Reals];Element[K2,Reals];Element[K3,Reals];Element[K4,Reals];
Element[c,Reals];Element[V0,Reals];Element[Q2,Reals];
Element[h,Reals];Element[f,Reals];Element[e,Reals];Element[FL1,Reals];Element[
FL2,Reals];Element[FU1,Reals];Element[FU1,Reals];Element[Q1,Reals];Element[Q3,Re
als];Element[Q4,Reals]

Q1= Quality factor of Z-component in the 1st ABZ
Q2= Quality factor of the X-component in the 1st ABZ
Q3= Quality factor of the Z-component in the 1st ABZ
Q4= Quality factor of X-component in the 1st ABZ
FL1= Lower frequency of Z-component near the Stopband(MHz)
FL2= Lower frequency of X-component near the Stopband(MHz)
FU1= upper frequency of Z-component near the stopband(MHz)
FU2= upper frequency of X-component near the stopband(MHz)
n= Domain number
h= Sample thickness (mm)
K1= Electromechanical coupling of Z- component in the 1st ABZ
K2= Electromechanical coupling of X- component in the 1st ABZ
K3= Electromechanical coupling of Z- component in the 2nd ABZ
K4= Electromechanical coupling of X- component in the 2nd ABZ
d= Domain length(mm)
c= elastic constant
w= Sample width(mm)
ε= Permittivity of the LiNbO3 (F/m)

V1=2*d*FL1; Phase velocity of Z- component in the 1st ABZ
V2=2*d*FL2; Phase velocity of X- component in the 1st ABZ
V3=2*d*FU1; Phase velocity of Z- component in the 2nd ABZ
V4=2*d*FU2; Phase velocity of X- component in the 2nd ABZ

k1=(2*π*f)/V1*(1-(™*1)/(2*Q1));    The wavenumber of the acoustic components
k2=(2*π*f)/V2*(1-(™*1)/(2*Q2));
k3=(2*π*f)/V3*(1-(™*1)/(2*Q3));
k4=(2*π*f)/V4*(1-(™*1)/(2*Q4));
ω=2*π*f;
```

F1:

$$= \frac{2 * i * n * d * 10^{-3}}{\epsilon * w * h * \omega}((1 - \text{Abs}[(\text{Sin}[\frac{k_1 * d}{2}] * \sum_{m=1}^{n} (-1)^m * \text{Sin}[\frac{k_1 * d}{2} * (2 * m - 1)]) \Big/ (\frac{k_1 * d * n}{2} * \text{Sin}[k_1 * d * \frac{n}{\sqrt{1 + \text{K1}^2}}])]) * (1 - \text{Abs}[(\text{Sin}[\frac{k_2 * d}{2}] * \sum_{m=1}^{n} (-1)^m * \text{Sin}[\frac{k_2 * d}{2} * (2 * m - 1)]) \Big/ (\frac{k_2 * d * n}{2} * \text{Sin}[k_2 * d * \frac{n}{\sqrt{1 + \text{K2}^2}}])]))/(2 - \text{Abs}[(\text{Sin}[\frac{k_1 * d}{2}] * \sum_{m=1}^{n} (-1)^m * \text{Sin}[\frac{k_1 * d}{2} * (2 * m - 1)]) \Big/ (\frac{k_1 * d * n}{2} * \text{Sin}[k_1 * d * \frac{n}{\sqrt{1 + \text{K1}^2}}])] - \text{Abs}[(\text{Sin}[\frac{k_2 * d}{2}] * \sum_{m=1}^{n} (-1)^m * \text{Sin}[\frac{k_2 * d}{2} * (2 * m - 1)]) \Big/ (\frac{k_2 * d * n}{2} * \text{Sin}[k_2 * d * \frac{n}{\sqrt{1 + \text{K2}^2}}])])(*1stABZ*)$$

$$\text{Impedanceinthe1stABZ}, Z = \frac{Z_x * Z_z}{Z_x + Z_z}$$

$$\text{F2:} = \frac{2 * i * n * d * 10^{-3}}{\epsilon * w * h * \omega}((1 - \text{Abs}[(\text{Sin}[\frac{k_3 * d}{2}] * \sum_{m=1}^{n} (-1)^m * \text{Sin}[\frac{k_3 * d}{2} * (2 * m - 1)]) \Big/ (\frac{k_3 * d * n}{2} * \text{Sin}[k_3 * d * \frac{n}{\sqrt{1 - \text{K3}^2}}])]) * (1 - \text{Abs}[(\text{Sin}[\frac{k_4 * d}{2}] * \sum_{m=1}^{n} (-1)^m * \text{Sin}[\frac{k_4 * d}{2} * (2 * m - 1)]) \Big/ (\frac{k_4 * d * n}{2} * \text{Sin}[k_4 * d * \frac{n}{\sqrt{1 - \text{K4}^2}}])]))/(2 - \text{Abs}[(\text{Sin}[\frac{k_3 * d}{2}] * \sum_{m=1}^{n} (-1)^m * \text{Sin}[\frac{k_3 * d}{2} * (2 * m - 1)]) \Big/ (\frac{k_3 * d * n}{2} * \text{Sin}[k_3 * d * \frac{n}{\sqrt{1 - \text{K3}^2}}])] - \text{Abs}[(\text{Sin}[\frac{k_4 * d}{2}] * \sum_{m=1}^{n} (-1)^m * \text{Sin}[\frac{k_4 * d}{2} * (2 * m - 1)]) \Big/ (\frac{k_4 * d * n}{2} * \text{Sin}[k_4 * d * \frac{n}{\sqrt{1 - \text{K4}^2}}])])$$

$$\text{Impedanceinthe2ndABZ}, Z = \frac{Z_x * Z_z}{Z_x + Z_z}$$

P1 = Plot[Abs[F1], {f, 3.25,3.32}, AxesLabel → {f[MHz], Z[Arb. unit]}, LabelStyle → Directive[Black, Bold, 30], PlotStyle → Directive[{Thickness[0.005], Black}], Filling → Axis, FillingStyle → Lighter[Blue,.7], GridLines → Automatic, GridLinesStyle → Directive[Red, Dashed]]

P2 = Plot[Abs[F2], {f, 3.6,3.72}, LabelStyle → Directive[Black, Bold, 30], PlotStyle → Directive[{Thickness[0.005], Black}], AxesLabel → {f[MHz], Z[Arb. unit]}, Filling → Axis, FillingStyle → Lighter[Blue,.7], GridLines → Automatic, GridLinesStyle → Directive[Red, Dashed]]

Phase Shift of FPS

First ABZ

```
β1=(2*π*f)/V1;
α1=(π*f)/(V1*Q1);
β2=(2*π*f)/V2;
α2=(π*f)/(V2*Q2);
Elements[{β1,α1},Reals];
k1=β1-™*α1;
Elements[{β2,α2},Reals];
k2=β2-™*α2;
```

F01:

$$= \frac{2 * n * d * i}{\epsilon * w * h * \omega}(1 - (\text{Sin}[\frac{\text{k1} * d}{2}] * \sum_{m=1}^{n} (-1)^m * \text{Sin}[\frac{\text{k1} * d}{2} * (2 * m - 1)]) \Big/ (\frac{\text{k1} * d * n}{2} * \text{Sin}[\text{k1} * d * \frac{n}{\sqrt{1 - \text{K2}^2}}]));$$

F02:

$$= \frac{2 * n * d * i}{\epsilon * w * h * \omega}(1 - (\text{Sin}[\frac{\text{k2} * d}{2}] * \sum_{m=1}^{n} (-1)^m * \text{Sin}[\frac{\text{k2} * d}{2} * (2 * m - 1)]) \Big/ (\frac{\text{k2} * d * n}{2} * \text{Sin}[\text{k2} * d * \frac{n}{\sqrt{1 - \text{K1}^2}}]))$$

$$\text{Z1:} = \sqrt{(\text{Re}[\text{F01}])^2 + (\text{Im}[\text{F01}])^2};$$

$$\text{Z2:} = \sqrt{(\text{Re}[\text{F02}])^2 + (\text{Im}[\text{F02}])^2}$$

$$\text{R1} \coloneqq \text{ArcTan}\left[\frac{\text{Im}[\text{F01}]}{\text{Re}[\text{F01}]}\right];$$

$$\text{R2} = \text{ArcTan}\left[\frac{\text{Im}[\text{F02}]}{\text{Re}[\text{F02}]}\right];$$

$$\text{RT:} = \text{ArcTan}\left[\frac{\left(\frac{\text{Im}[\text{F01}]}{\text{Re}[\text{F01}]}\right) + \left(\frac{\text{Im}[\text{F02}]}{\text{Re}[\text{F02}]}\right)}{1 - \left(\frac{\text{Im}[\text{F02}]}{\text{Re}[\text{F02}]}\right) * \left(\frac{\text{Im}[\text{F01}]}{\text{Re}[\text{F01}]}\right)}\right];$$

Plot[RT, {f, 3.22,3.31}]

Second ABZ

```
β3=(2*π*f)/V3;
α3=(π*f)/(V3*Q3);
β4=(2*π*f)/V4;
α4=(π*f)/(V4*Q4);
Elements[{β3,α3},Reals];
k3=β3-™*α3;
Elements[{β4,α4},Reals];
k4=β4-™*α4;
```

F03:

$$= \frac{2 * n * d * i}{\epsilon * w * h * \omega}(1 - (\mathrm{Sin}[\frac{k3 * d}{2}] * \sum_{m=1}^{n} (-1)^m * \mathrm{Sin}[\frac{k3 * d}{2} * (2 * m - 1)]) \Big/ (\frac{k3 * d * n}{2} * \mathrm{Sin}[k3 * d * \frac{n}{\sqrt{1 - K2^2}}]));$$

F04

$$:= \frac{2 * n * d * i}{\epsilon * w * h * \omega}\left(1 - \left(\mathrm{Sin}\left[\frac{k4 * d}{2}\right] * \sum_{m=1}^{n} (-1)^m * \mathrm{Sin}\left[\frac{k4 * d}{2} * (2 * m - 1)\right]\right) \Big/ \left(\frac{k4 * d * n}{2} * \mathrm{Sin}\left[k4 * d * \frac{n}{\sqrt{1 - K1^2}}\right]\right)\right)$$

$$Z3 := \sqrt{(\mathrm{Re}[F03])^2 + (\mathrm{Im}[F03])^2};$$

$$Z4 := \sqrt{(\mathrm{Re}[F04])^2 + (\mathrm{Im}[F04])^2}$$

$$R3 := \mathrm{ArcTan}\left[\frac{\mathrm{Im}[F03]}{\mathrm{Re}[F03]}\right];$$

$$R4 = \mathrm{ArcTan}\left[\frac{\mathrm{Im}[F04]}{\mathrm{Re}[F04]}\right];$$

$$RT := \mathrm{ArcTan}\left[\frac{\left(\frac{\mathrm{Im}[F03]}{\mathrm{Re}[F03]}\right) + \left(\frac{\mathrm{Im}[F04]}{\mathrm{Re}[F04]}\right)}{1 - \left(\frac{\mathrm{Im}[F03]}{\mathrm{Re}[F03]}\right) * \left(\frac{\mathrm{Im}[F04]}{\mathrm{Re}[F04]}\right)}\right];$$

$$\mathrm{Plot}[RT, \{f, 3.6, 3.71\}];$$

VITA

OLA H. NUSIERAT

Teaching Assistant
University of Mississippi Dept of Physics and Astronomy

EDUCATION

M.S., **Applied Mathematics**, University of Alabama at Birmingham (UAB), May 2010

M.S., Physics, Jordan University of Science and Technology (JUST), May 2007

B.S., **Applied Physics**, (JUST), Jan 2004

EXPERIENCE

University of Mississippi **Aug2011-Present**
Department of Physics and Astronomy
Graduate Teaching Assistant
Courses: Laboratory Physics I (spring 2012, summer 2012, fall 2012, fall 2014)
Supervised, instructed, and graded undergraduate students in physics laboratory class in connection with the lecture class.

University of Alabama at Birmingham (UAB) **Aug 2008 –May 2010**
Department of Mathematics
Graduate Teaching Assistant
Courses: College Algebra (Fall 2009)
Intermediate Algebra (Spring 2010)

Responsible for course plans and materials, monitoring progress/attendance, advising students, preparing quizzes, study sheets, and exams. Also I administrate, proctor, and graded exams, quizzes, homework assignments, and recording grades and submitting reports, and I assign final grades for my students.

All level of Junior High School (General Physics). **Jan 2004-Dec 2006**

AFFILIATIONS & ACTIVITIES

American Physical Society (APS), Student member, 2013-Present
Acoustical Society of America, Student Member, 2013-Present
Mississippi Academy of Science (MAS), Student member, 2014-Present
Member of the Organizing committee of Conference for Undergraduate Women in Physics at the University of Mississippi, Jan 2015
Society of Physics Students

HONORS, AWARDS, & FELLOWSHIPS

Dissertation Fellowship Award, spring 2015

Summer Research Assistantship Award, summer 2013

University of Mississippi Zdravko Stipcevic Honors Fellow, 2012-2014

Jordan University of Science and Technology, Undergraduate fellowship.

SKILLS

Languages: English and Arabic
Computer software: Matlab, Mathematica, Microsoft Office, Python, LATEX, and COMSOL.
COMSOL Structural Mechanics Workshop at the University of Mississippi, December 3rd 2014

PUBLICATIONS

Ola Nusierat[1], Lucien Cremaldi and Igor Ostrovskii**,"Acoustical transduction in two- dimensional piezoelectric array"** J. Acoust. Soc. Am. 136, 2252 (2014)

Ola Nusierat[1], Lucien Cremaldi and Igor Ostrovskii ," Acousto-electric admittance of two-dimensional ferroelectric metamaterial" J. Acoust. Soc. Am. (Jan. 2015) Accepted

PRESENTATIONS

O.Nusierat "Acousto-electric Impedance of Ferroelectric Phononic Superlattice" APS Conference for Undergraduate Women in Physics at the University of Mississippi, Jan 2015

O.Nusierat "Acousto-electric Impedance of Ferroelectric Phononic Superlattice" Colloquium in Physics Department of University of Mississippi, Nov 2014

O. Nusierat, L. Cremaldi, and I. Ostrovskii "Acoustical Transduction in two-dimensional piezoelectric array" 168th Meeting: Acoustical Society of America, Indianapolis, October 2014

O. Nusierat, L. Cremaldi, and I. Ostrovskii "Acousto-electric Impedance of Periodically Poled LiNbO3 wafer" 78th Annual meeting: Mississippi Academy of Science, March 2013